

**Detector characterization
and Λ_b measurements
with the upgrades
of the ALICE
Inner Tracking System**

Dimitra Andreou



**Detector characterization and Λ_b measurements with
the upgrades of the ALICE Inner Tracking System**

Dimitra Andreou

Copyright © 2021 Dimitra Andreou.

Cover design by Dimitra Andreou.

Cover photo by Nikolaos Tsoulos,

Statue of Pythagoras at Pythagorio, Samos, Greece.

Typeset by L^AT_EX.

Printed by ProefschriftMaken | ProefschriftMaken.nl.

ISBN: 978-94-6423-561-6

Detector characterization and Λ_b measurements with the upgrades of the ALICE Inner Tracking System

Detector karakterisering en Λ_b metingen met de upgrades van het ALICE Inner Tracking System

(met een samenvatting in het Nederlands)

Proefschrift

ter verkrijging van de graad van doctor aan de
Universiteit Utrecht
op gezag van de
rector magnificus prof.dr. H.R.B.M. Kummeling,
ingevolge het besluit van het college voor promoties
in het openbaar te verdedigen
op maandag 6 december 2021 des middags te 2.15 uur

door

Dimitra Andreou

geboren op 17 januari 1991
te Amarousio, Griekenland

Promotor: Prof. dr. R.J.M. Snellings

Copromotoren: Dr. P.G. Kuijer
Dr. L. Musa

Contents

1	Early universe in the ALICE experiment	5
1.1	A few moments after the Big Bang	5
1.2	Quantum Chromodynamics in the Standard Model	7
1.3	ALICE experiment in a nutshell	9
1.3.1	Large Hadron Collider	9
1.3.2	The ALICE apparatus	10
1.3.3	Inner Tracking System	13
1.3.4	Time Projection Chamber & Time Of Flight detectors .	13
1.4	Heavy Flavour production in Pb – Pb collisions	14
1.5	Future prospects with detector upgrades	17
1.5.1	ALICE upgrades for a High Luminosity LHC	17
1.5.2	Heavy flavour in a high precision era	21
2	Detector physics and technologies	23
2.1	Tracking detectors	23
2.2	Particle interactions with matter	28
2.2.1	Bethe-Bloch	30
2.2.2	Straggling function	31
2.3	Silicon detectors	31
2.3.1	Band Model	32
2.3.2	p-n junction	35
2.3.3	Monolithic Active Pixel Sensors	37
3	Upgrade of the ALICE Inner Tracking System	43
3.1	Detector specifications	43
3.2	The ALPIDE sensor	44
3.2.1	ITS in the MAPS era	46
3.2.2	Front-end electronics, architecture and features	47

3.3	Detector layout	49
3.3.1	Production and materials	55
3.4	Detector characterization	61
3.4.1	Electrical qualification	64
3.4.2	Ageing projection	81
4	Beauty measurements with the ITS upgrades	85
4.1	ITS upgrade performance	85
4.2	Λ_b measurements with ITS2 and ITS3 upgrades	87
4.2.1	Λ_b reconstruction	88
4.2.2	Monte Carlo sample	88
4.2.3	Selection of Λ_b with topological cuts	90
4.2.4	Analysis results	97
5	Discussion	101
	Appendices	105
A	New-alpide-software	105
A.1	Classification cuts of individual scans	105
	References	115
	Summary	117
	Samenvatting	119
	Acknowledgements	121
	Curriculum Vitae	123

Early universe in the ALICE experiment

1.1 A few moments after the Big Bang

QUESTIONS about the nature of our cosmos, its origin and evolution have intrigued humanity from the very early times. The theory towards the description of the beginning of the universe was proposed by George Lemaître [1] and was scientifically supported by Hubble's observation [2]. Since then the Big Bang theory is guiding the scientists in their search to understand the very first moments of the early universe [3]. After the Big Bang, the universe started rapidly to expand, an expansion that continues until today in a less rapid way and it is accompanied by a decrease in the temperature and the density of the universe. A few moments after the Big Bang, the four basic forces of nature, gravity, electromagnetism, the weak interaction and the strong interaction, became discrete and took the form we know today. At that time, the universe was in a state of a very hot and dense plasma, the Quark–Gluon Plasma, whose high temperature didn't allow the formation of particles. The Quark–Gluon Plasma contained bosons, quarks, leptons and their anti-particles moving freely. When the temperature was sufficiently low, the elementary particles started to bond together and to form hadrons, the subatomic particles which are composed of quarks and gluons.

The aim of the ALICE experiment [5] is to reproduce this state of matter, the Quark–Gluon Plasma, and study its properties while it is cooling down, expanding and forming the building blocks of our current world. The prop-

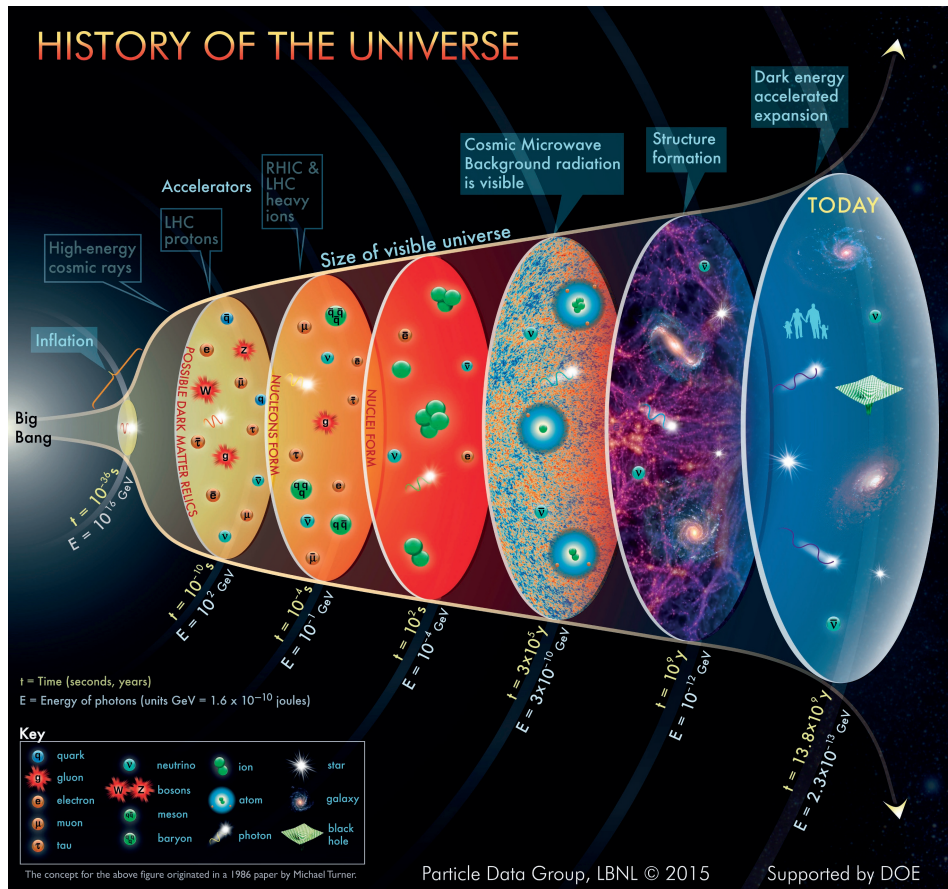


Figure 1.1: *Evolution of the universe [4].*

erties of the Quark–Gluon Plasma are crucial for the understanding of the theory of Quantum Chromodynamics (QCD), which is the part of Standard Model, describing the strongly interacting matter. The reproduction of the Quark–Gluon Plasma is done with heavy ion collisions in the Large Hadron Collider (LHC). When large nuclei collide, the region of space where the energy density is high, is larger than the size of a hadron. This is a key issue in order to achieve proper deconfinement of the Quark–Gluon Plasma and the reason why the interest of the ALICE experiment is focused on the Pb–Pb collisions. However, the ALICE detector is operating also in Pb–p, and p–p collisions in order to produce reference data for the nucleus–nucleus collisions, distinguish the different effects in the different systems and study effects in high-multiplicity p–p [6].

1.2 Quantum Chromodynamics in the Standard Model

The theory that describes the subatomic physics and its laws is the Standard Model [7] [8]. The fundamental particles of the Standard Model are divided into two categories, the fermions and the bosons. The fermions are the particles with a half-integer spin quantum number that obey the Fermi-Dirac statistics, whereas the bosons are integer spin particles that follow the Bose-Einstein statistics.

The fermions are further divided into quarks and leptons. There are 6 different flavors of quarks, the up (u), down (d), strange (s), charm (c), bottom (b), top (t) quark and their anti-quarks. The quarks are characterised by different properties which are: the spin, the mass, the electric charge and the color charge. Due to a phenomenon called color confinement which is present in the Quantum Chromodynamics, the quarks cannot be observed alone, but they bind with other quarks and they form hadrons, mesons or baryons. The quarks can experience all the forces of nature the strong interaction, the electromagnetism, the weak interaction and gravity.

In contrast, the leptons cannot experience the strong interaction. There are 3 generations of leptons, the charged electron, the charged muon and charged tau with their associate electrically neutral neutrinos, the electron neutrino, the muon neutrino and the tau neutrino. The force carriers of the Standard Model are the bosons. According to the Standard Model there is a spin 0 scalar boson, the Higgs boson and four spin 1 gauge bosons. The gauge bosons are: the photon, the electrically neutral weak boson Z, two types of electrically charged weak bosons W and 8 differently color charged gluons.

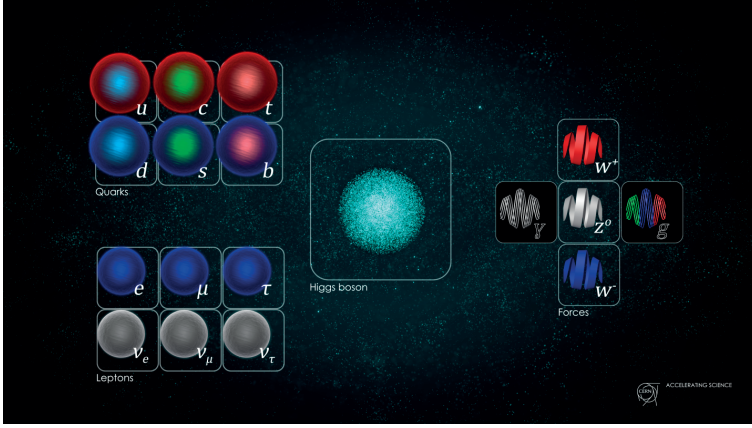


Figure 1.2: *Fundamental particles of the standard model [9].*

The field theory that describes the strong interactions and thus how the gluons interact with each other and how they combine with quarks and form hadrons, is expressed by the QCD Lagrangian:

$$L_{QCD} = \bar{\psi}_i(i\gamma^\mu\partial_\mu - m)\psi_i - 1/4F_\alpha^{\mu\nu}F_{\mu\nu}^\alpha - g_s\bar{\psi}_i\lambda_{ij}^\alpha\psi_j\gamma^\mu A_\mu^\alpha \quad (1.1)$$

where:

m : mass

ψ : Dirac spinor

μ : Lorentz index 0,1,2,3

γ^μ : gamma matrix

∂_μ : derivative

i : color index for the quark field

α : color index for the gluon field

λ : eight Gell-Mann matrices

g_s : strong coupling constant

A_μ^α : four potential gluon fields

$F_\alpha^{\mu\nu}$: color field tensor

The QCD Lagrangian is a representation of a field theory which is invariant under the non-Abelian SU(3) symmetry. The first term of the QCD Lagrangian is describing a free Dirac particle and gives rise to the quark propagators. The second term is the free Lagrangian of the gluon field from

which the gluon propagators are derived. In order for this term of the QCD Lagrangian to be gauge-invariant a new term is introduced in the QED field tensor. This modification gives rise to the three and four-gluon self interactions, which are responsible for the most important QCD features, asymptotic freedom, color confinement and chiral symmetry breaking. Finally the last term of the Lagrangian is the interaction term which describes the quark-gluon vertex.

The QCD theory describes the strongly interacting matter in two evolution phases the one of hadron gas and the one of QGP which are characterized by the temperature and the baryo-chemical potential μ_B , the measurement unit of the net baryon density. The hadron gas phase is characterized by moderate temperatures and densities with quarks and gluons being confined and the chiral symmetry spontaneously broken. On the contrary, as mentioned earlier in the QGP phase the temperatures and densities are significantly larger, the quarks and gluons are deconfined and the chiral symmetry is restored. The point where the phase transition takes place in terms of T and μ_B is given by the QCD phase diagram shown in Figure 1.3. The termination point of the first order phase transition line is defined as the critical point T_c , the study and the understanding of which are benchmarks for the heavy ion experiments [10]. The initially high temperature of the QGP produced in heavy ion collisions drops and the matter experiences a cross-over or a first order phase transition depending on the μ_B value. From the experimental aspect, by varying the energy of the collision, the initial temperature and the μ_B vary as well, with higher collision energies corresponding to higher temperatures and lower values of μ_B . In this way the exploration of different regions of the QCD phase diagram becomes available with the cross-over region drawing the attention as the colliding energies become higher.

1.3 ALICE experiment in a nutshell

1.3.1 Large Hadron Collider

The Large Hadron Collider (LHC) at CERN is the world's largest accelerating system devoted to High Energy Physics studies. The LHC is a 27 km ring that is located down to 100 m underground the Swiss-French border in the Geneva area. Inside the underground tunnels particle beams are accelerated to velocities close to the speed of light in opposite directions and guided by superconducting electromagnets. The beams collide in dedicated locations,

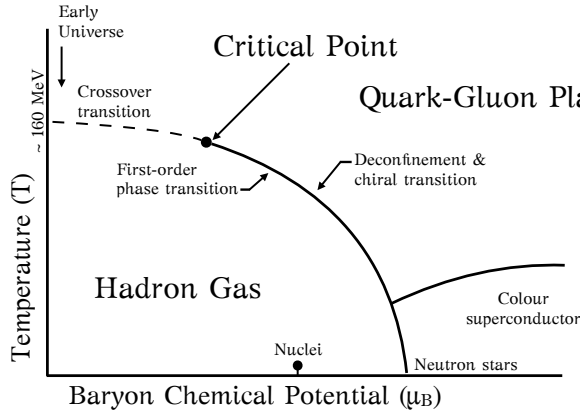


Figure 1.3: QCD phase diagram [11].

where large detector systems are built and are ready to capture the outcome of the collisions. The four main experiments at CERN are the ALICE, the ATLAS (A Toroidal LHC Apparatus), the CMS (Compact Muon Solenoid) and the LHCb (LHC-beauty) experiments that are dedicated to explore different pieces of the high energy physics (HEP) puzzle. The colliding beams in the LHC consist of proton-proton, ion-ion as well as proton-ion particles which are pre-accelerated in the PS and SPS accelerators before they enter the LHC ring. An overview of the CERN accelerator complex is presented in Figure 1.4. The LHC during the last year of operation before entering on an upgrade phase reached the collision energy of 13 TeV.

1.3.2 The ALICE apparatus

The ALICE detector is installed 56 m beneath Saint-Genis-Pouilly in France, occupying a space of $26 \text{ m} \times 16 \text{ m} \times 16 \text{ m}$ in length, height and width respectively. It consists of 19 different sub-detectors which according to their position in the ALICE apparatus they target on different particle measurements. The goal of the ALICE sub-detectors, which are surrounding the interaction point, is to reconstruct the path of the particles produced during the collision while they are sequentially decaying to their daughter particles which leave their footprint in the different sub-detectors. An overview of the ALICE sub-detectors is demonstrated in Figure 1.5.

The ALICE sub-detectors provide all the necessary information for the

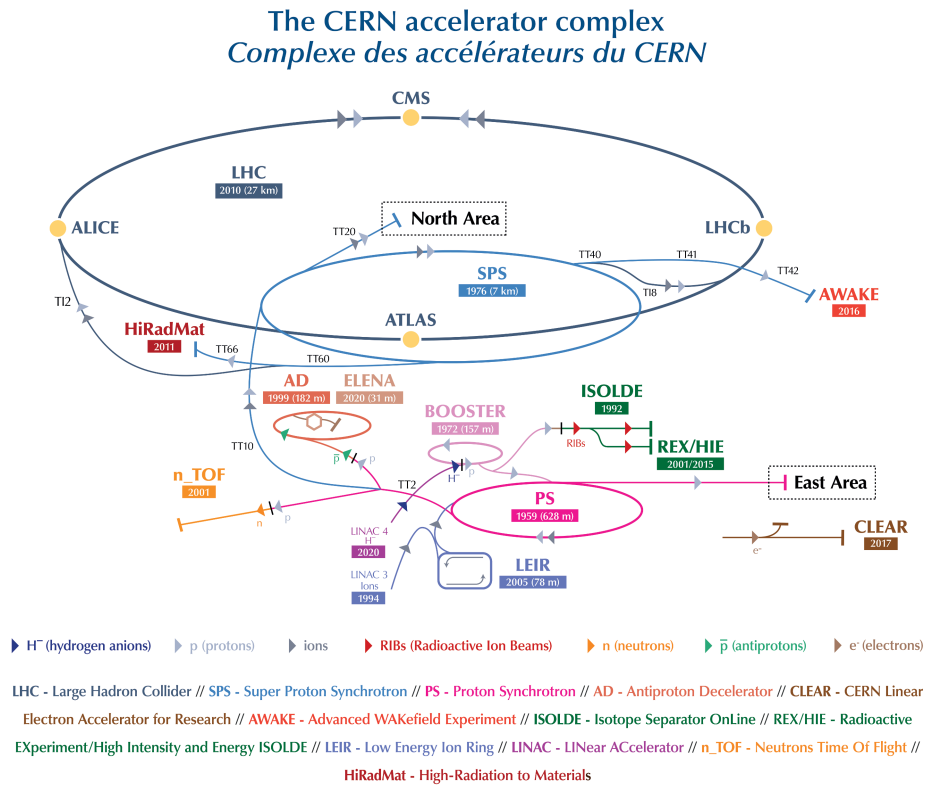


Figure 1.4: *The CERN accelerator complex. [12]*

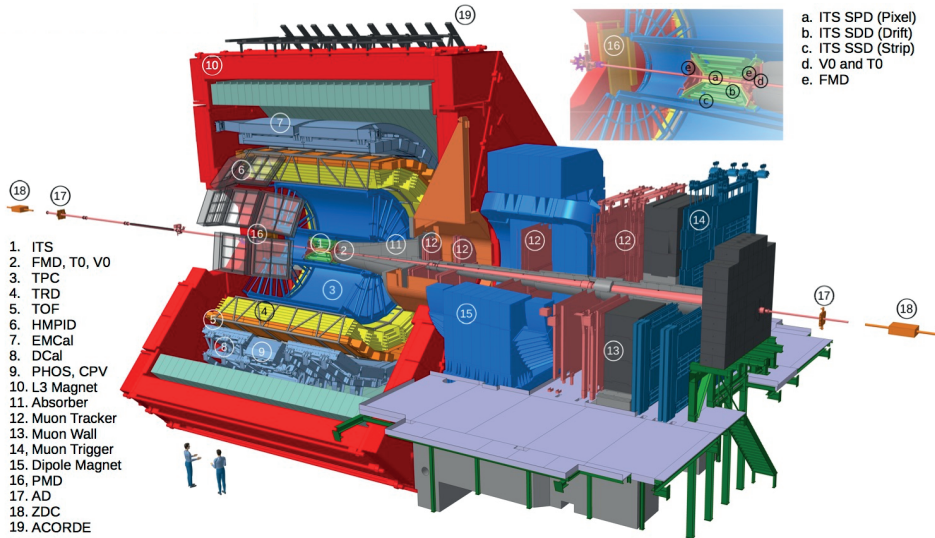


Figure 1.5: *The ALICE detector [13].*

reconstruction of the collision event and the particle tracks. A group of detectors are dedicated for the characterisation of the collision providing the number of the produced particles together with their distribution in space, as well as, collision time measurements with high precision. These detectors that grade the power level of the collision are the Zero Degree Calorimeter (ZDC), the FMD, the V0 and the T0 detectors.

The Inner Tracking System (ITS) together with the Time Projection Chamber (TPC) and the Transition Radiation Detector (TRD) are another sub group of detectors that are responsible for the particle's tracking. Starting from the closest possible distance from the collision, they are surrounding in cylindrical layers the interaction point while they are operating within the magnetic field. The track reconstruction capabilities of these detectors are very powerful with the ITS being able to distinguish particles that originate from the interaction point (prompt particles) from others that are the decay products of prompt ones which decayed a few microns from the interaction point. Along with the tracking the ITS and the TPC have Particle IDentification (PID) capabilities. The PID information given by the ITS, the TPC and the Time Of Flight (TOF) detectors is a crucial part of the particle's reconstruction. A more detailed description of these detectors is provided in the next part of this session.

The identification of lighter and thus faster particles is done by the High Momentum Particle Identification Detector (HMPID) and TRD detectors. With the electrons being identified by the latter one, the muons are finally captured by the muon spectrometer which is a group of sub-detectors installed in the forward region, in front of a thick absorber that denies the penetration of other than muon particles. Finally the "visible" light, the photons are measured by the crystal equipped Photon Spectrometer (PHOS), the Photon Multiplicity Detector (PMD) and by the Electro-Magnetic Calorimeter (EMCal). The lead-scintillator EMCAL is also responsible for the detection of narrow cones of particles, the particle jets.

1.3.3 Inner Tracking System

The heart of ALICE, the ITS, is the first detector that the emerging particles from the collision interact with. The role of the ITS, is the determination of the decay vertices and the particle tracks in the region with the highest particle multiplicities. As will be discussed in detail in Chapter 2, the requirement for the inner detector layers is a high granularity, low material budget detector that offers optimal pointing resolution and tracking efficiency. These are the key features of the ITS towards capturing heavy particles that decay in short distances from the interaction point and are abundant in the low momentum region.

The current ITS consists of six detector layers, which share three different technologies of the silicon imaging process equally distributed from the inner to the outer layer. The two innermost layers consist of Silicon Pixel Detectors (SPD) which are responsible for the precise determination of the decay vertex of charm and beauty. The two central layers of the ITS consist of Silicon Drift Detectors (SDD) which are further surrounded by the two outer layers of Silicon Strip Detectors (SSD). Through measurements of the particles' energy loss in the detector material, the particle identification enhances the tracking capabilities and the association of the reconstructed tracks with the TPC.

1.3.4 Time Projection Chamber & Time Of Flight detectors

The TPC detector is installed in the central barrel of ALICE and surrounds the ITS. The main goals of the TPC are the particle identification together with the determination of the tracks and the decay vertices of hadrons and leptons. The TPC cylindrical barrel has an active volume of 90 m^3 that is filled with gas which is the interacting medium where the traversing particles deposit

part of their energy. Through the particles' energy loss the identification of the particle species is achieved. The readout of the TPC is done through Multi-Wire Proportional Chambers (MWPCs) which are installed in the end caps.

The TOF detector is providing complementary information for the particle identification by measuring the time of flight of the particles from the time they start their journey from the interaction point until they reach the detector material. The TOF is equipped with an array of Multi-gap Resistive Plate Chambers (MRPCs) which together with the readout channels cover an area of 160 m^2 . The PID capabilities of the TPC and of the TOF are presented in Figure 1.6 which demonstrates the strong separation power for different particle species of the TPC and of the TOF in the momentum regions below 4 and $2.5 \text{ GeV}/c$ respectively.

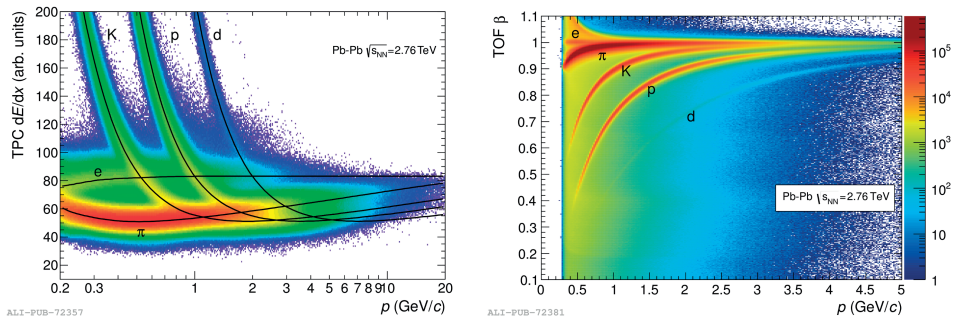


Figure 1.6: Particle identification with the TPC (left) and with the TOF (right) detectors. In the TPC case the energy loss dE/dx of electrons, protons, kaons, pions and deuterons is plotted as function of the momentum, while in the case of TOF the velocity β of the same particles is presented as function of the momentum.

1.4 Heavy Flavour production in Pb – Pb collisions

One promising way for the characterization of the QGP and its properties is by studying the heavy flavour particles and their behaviour that are produced in the heavy ion collisions. With the term heavy flavour are described all the mesons and baryons that are formed from at least one heavy flavour quark, a beauty (b) or a charm (c) one or from one of their anti-quarks.

The heavy flavour quarks are produced in the very early stages of Pb–Pb collisions through hard scattering processes, a characteristic that establishes them as excellent probes of the QGP since they are present in all stages of the collision.

Two important processes that are studied in the heavy flavour sector are the processes of the thermalization and the hadronization of heavy quarks in the medium. Starting from the thermalization process, while the heavy quarks are moving freely in the hot and dense plasma they may reach equilibrium with the medium. The relaxation or equilibration time of heavy quarks, given by Equation 1.2, is related to the heavy-quark diffusion coefficient \mathcal{D}_s which is among the most important transport coefficients for the characterization of the QGP properties. The limits on the heavy quark diffusion coefficient are set through precise measurements of the nuclear modification factors R_{AA} and of transverse momentum anisotropies v_n .

$$\tau_Q = \frac{m_Q}{T} \mathcal{D}_s \quad (1.2)$$

where:

m_Q : the quark mass

\mathcal{D}_s : the diffusion coefficient

T : the medium temperature

After the initial hard scattering phase the number of the produced heavy quarks is conserved throughout the interaction, while the partonic distribution in the momentum space is modified due to medium effects like collective flow. In addition, the heavy quarks interactions with the medium lead to the energy loss of their initial energy. The R_{AA} factor is used to study the energy loss of the partons by comparing the production yields of specific particle species produced in heavy ion collisions to the yields of the same particles produced in proton–proton collisions. On the other hand, the aforementioned momentum anisotropies, which in the azimuthal plane are defined as elliptic flow v_2 , are accessed through the measurements of the second harmonic coefficient of the Fourier decomposition of the azimuthal distribution. A precise measurement of the v_2 qualifies the particles degree of participation in medium collective flow.

In addition to the thermalization, the R_{AA} and v_2 observables are strongly affected by the hadronization process. The hadronization mechanisms of free quarks and gluons in order to form mesons and baryons are described by

various models. The different theoretical approaches include the fragmentation and the recombination processes as the hadronization mechanisms, which contribute together and in different fractions or independently in the hadronization [14]. In the high momentum regions the fragmentation process is expected to be dominant with the high p_T heavy quarks fragmenting directly in high p_T hadrons. On the contrary, in the low momentum region, the contribution of recombination in the hadronization process is expected to be higher. During recombination, the heavy quarks combine with the light quarks which are abundant in the low p_T region. The hadronization through recombination results in the enhancement of some particle species. In particular, recent results have shown an enhancement in the baryon to meson ratio in heavy ion collisions with respect to p-p, possibly due to recombination [15] [16]. The quantitative level of this enhancement is a key issue for the hadronization process and can be obtained through measurements of the different particle species. The measurements of the following baryon over meson ratios $\frac{\Lambda_b}{B}$, $\frac{\Lambda_c}{D}$ in a wide momentum range and especially in the low p_T are among the ALICE objectives for the coming years. The latest ALICE results on heavy flavour indicate that the first steps towards the investigation of the heavy flavour production are done and that a new path towards the low p_T is waiting to be understood. In the charm sector, the first measurement of the D^0 meson was recently reported to p_T down to 0 GeV/c. A measurement that was extended to the R_{AA} observable, and allowed the comparison of the different models and energy loss mechanisms. In addition, the first hints of $\frac{\Lambda_c}{D}$, baryon over meson, enhancement has been observed supporting the charm recombination scenario but at the same time leaving room for improvement in the future measurements. In the D meson family, new measurements on the $\frac{D_s}{D}$ indicate an enhancement of the ratio in Pb-Pb with respect to p-p, as it is predicted in case of recombination in a strangeness rich environment [17]. Finally, in the beauty sector measurements of the R_{AA} of the non-prompt D^0 produced from a b decay provide information on the beauty energy loss [18]. The aforementioned results opened the way towards the investigation of heavy flavour production which will be accessed with higher precision in the coming years.

1.5 Future prospects with detector upgrades

During the operation of the ALICE apparatus in Run 1 and in Run 2 a significant number of important measurements has been achieved in the heavy flavour sector revealing crucial information about the processes of hadronization and thermalization of heavy quarks in medium. The latest updates on charm and beauty started imposing constraints on the theoretical calculations, which need to be further explored with higher precision. A higher precision demands additional statistics, which can be achieved through the combination of the High Luminosity LHC (HL-LHC) upgrade with the sub-detector upgrades of the ALICE experiment. With the completion of Run 2 in 2018 and with the accumulated integrated luminosity exceeding the target of 1 nb^{-1} , the upgrades of the ALICE detectors took place during the second LHC Long Shutdown (LS2). The upgrade strategy of the detectors [19], was based on the full exploitation of the HL-LHC upgrade which will reach an interaction rate of 50 kHz in Pb–Pb collisions resulting to an increase of the instantaneous luminosity to values up to $\mathcal{L} = 6 \cdot 10^{27} \text{ cm}^{-2} \text{ s}^{-1}$ in Run 3 and in Run 4. The intermediate third LHC Long Shutdown (LS3) will allow a further upgrade of the ALICE ITS targeting to an improved performance of the ALICE tracker in the low momentum region. The fully equipped ALICE detector will be able to record data of 10 nb^{-1} during the next decade.

1.5.1 ALICE upgrades for a High Luminosity LHC

A brief description of the detector upgrades that ALICE has scheduled for Run 3 and for Run 4 is given in the following sessions.

Detector upgrades for Run 3

- **Beam pipe**

During LS2 the beam pipe geometry will be modified by reducing its radius from the present value of 29.8 mm to 19.2 mm, in order to allow the innermost layer of the ITS to approach the interaction point.

- **Trackers upgrade**

Towards the direction of an improved pointing resolution and tracking efficiency, a major upgrade of the ITS, the ITS2, will take place together with the installation of a new detector, the Muon Forward Tracker

(MFT) [20]. The ITS upgrade will offer a high granularity and low material budget detector equipped with a new lightweight mechanical design combined with the latest technology in silicon pixel sensors. The detector overview of the upgraded ITS is demonstrated in Figure 3.5. The first part of the current thesis is devoted to the detector studies that were performed during the ITS2 production phase and are in details presented in Chapter 3.

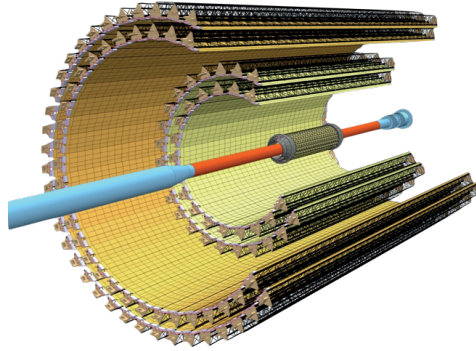


Figure 1.7: *Detector layout of the upgraded ITS.*

With the installation of the MFT detector which will cover a pseudo-rapidity range of $-3.6 < \eta < -2.5$, the Muon spectrometer will be enhanced with vertex capabilities and provide access to semi-muonic decays in the low momentum region. The new detector will consist of silicon pixel planes, sharing the same sensor and readout technology of the upgraded ITS.

- **TPC upgrade**

The upgrade of the TPC includes the replacement of the MWPCs by Gas Electron Multiplier (GEM) chambers and of the gating grid readout system by the new ReadOut Chambers (ROCs). The new readout system, that the GEMs can support, will allow the continuous data readout and thus the full event reconstruction while the particle identification capabilities of the stand-alone TPC will be retained [21].

- **Fast Interaction Trigger (FIT) detector**

A new forward trigger detector, FIT, is going to be installed in ALICE. FIT will be the primary trigger detector that will provide luminosity and

collision time measurements. The new detector will be also responsible for the determination of the multiplicity, the centrality, and the reaction plane of heavy ion collisions.

- **Readout electronics upgrade**

The readout electronics of many sub-detectors of ALICE will undergo an upgrade in order to be able to follow the increased particle rate. The readout systems of the Transition Radiation Detector (TRD), the TOF detector, the Photon Spectrometer (PHOS), the Muon Spectrometer and Zero-Degree Calorimeter (ZDC) will be upgraded [22].

- **Online-Offline Computing upgrade**

The ALICE Online-Offline Computing system, O^2 system, will be upgraded to a new software framework that together with a new computing facility will enable the continuously zero suppressed data readout and the real time online reconstruction. The system will be equipped with fast tracking algorithms and online clustering that will allow a rapid data extraction [23].

ITS upgrade for Run 4

During the LS3, a further upgrade is planned for the ALICE ITS, that targets high precision measurements of charm and beauty in the low momentum region. The strategy behind the ITS upgrade for Run 4, the ITS3, is based on the effort to get closer to the interaction point and reduce further the material budget. As is demonstrated in Figure 1.8, the material budget of ITS2, offers enough room for improvement with the silicon occupying only the 15% of the total material budget of the ITS2.

The detector design of the ITS3 upgrade, Figure 1.9, is based on a silicon-only inner barrel that will replace the inner barrel of the ITS2. For the ITS3 upgrade ALICE will benefit from the latest detector technologies that are becoming available in the silicon imaging field and which allow the elimination of additional components in the fiducial volume of the detector. The objective of an almost "massless" inner barrel in the ALICE tracker will lead to the enhancement of many heavy flavour measurements.

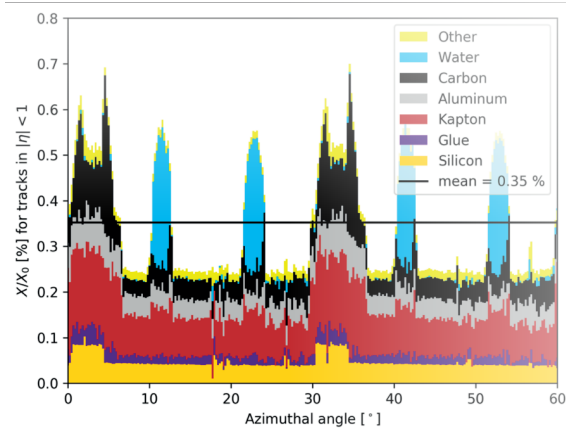


Figure 1.8: *Material budget of ITS detector during Run 3 [24].*

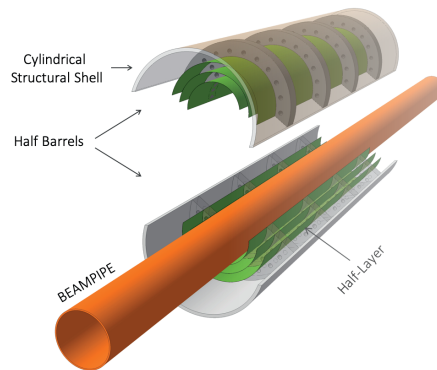


Figure 1.9: *Detector design for the future upgrade for Run 4 [24].*

1.5.2 Heavy flavour in a high precision era

The increased LHC luminosity in combination with the detector upgrades will open a new era of high precision measurements aiming to give answers to the remaining open questions of the behaviour of heavy flavour in the QGP. Through high precision measurements of v_n and of R_{AA} for charm and beauty in a large kinematic range, strong constraints will be imposed on the heavy quark diffusion coefficient and its dependence on temperature. These constraints will not only quantify the thermalization level of heavy quarks in medium but will also indicate which are the leading interactions mechanisms of heavy quarks with the QGP. Recent studies on the expected performance of the LHC experiments after the LS2 demonstrate an enhanced constraining power on the spatial diffusion coefficient with the detector upgrades and with the luminosity at the level of 10 nb^{-1} . As it is demonstrated in the left panel of Figure 1.10, for the expected reduction on the uncertainty of the D-meson R_{AA} measurements by a factor between two and five, a corresponding reduction of 50% and 20% is foreseen on the $2\pi T \mathcal{D}_s$ uncertainty. In the region around the critical temperature the values of the diffusion coefficient uncertainties are estimated to be 30 – 50% of the present values based on the projected R_{AA} and on the v_2 measurements (right panel Figure 1.10).

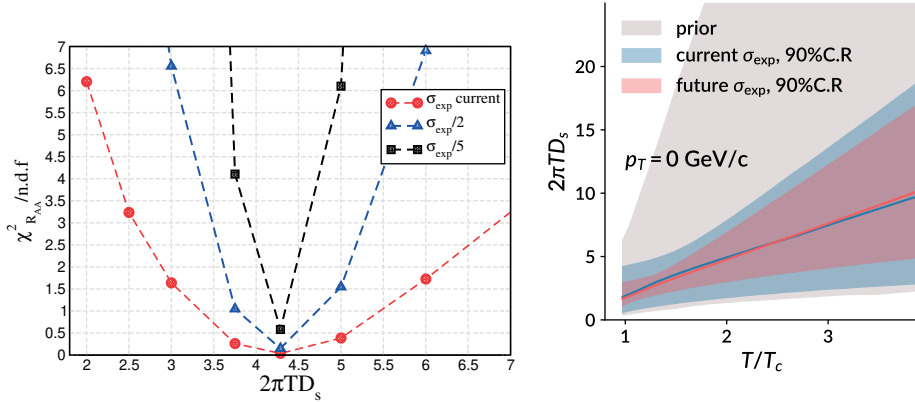


Figure 1.10: χ^2 as function of the spatial diffusion coefficient with the current and future experimental precision based on the Catania Fokker-Plank transport model (left). Spatial diffusion coefficient as function of the T/T_c for the current and the expected performance with a modified Langevin framework [25].

The high precision measurements in the low momentum region will not only give important information about the thermalization but also about the hadronization process. The unexplored low momentum region in the cases of strange mesons as well as of charm and beauty baryons, hides important information about the contribution of recombination in the hadronization process. The baryon to meson enhancement will be studied in a wider p_T range and the level of recombination contribution will be determined with higher precision. [25].

Performance studies in ALICE have shown that the ITS2 and the ITS3 upgrades, will open a new high precision era in heavy flavour measurements in a wide momentum range [26]. The improvement in the pointing resolution and the tracking efficiency that the upgrades will offer will allow the measurements of particles that were not accessible before due to the large combinatorial background and the enhancement of measurements that were earlier limited due to the lack of statistics. Through the ITS2 upgrade, the reconstruction of charged and neutral D mesons, D^0 , D^+ and D_s , will be significantly improved, an improvement which will be propagated to the B meson decays through the D meson daughters. Indicatively the measurement of the B^+ meson decaying to a \bar{D}^0 and a π^+ will be significantly improved. The improvement is reflected also on the measurements of charm and beauty baryons, namely for the Λ_c^+ and the Λ_b . The decay channel of Λ_c^+ to a $p K^- \pi^+$ has a small decay length, $c\tau \approx 60\mu\text{m}$, and thus the optimized separation of the primary to the secondary vertex will lead to the improvement of this measurement. With the further upgrade of the ITS3, all the above heavy flavour channels will be measured with higher precision in the low momentum region and new ones especially on particles with small $c\tau$ will be explored. Specifically, the measurements of Ξ_c^+ , Ξ_c^0 , Ω_c^0 with $c\tau$ 137, 46 and 80 μm respectively are expected to be visible due to the further enhanced primary to secondary vertex separation. The measurement of B_s meson, will become accessible too, benefiting from the improvement in the measurement of the non-prompt D_s . One of the benchmark channels of the ITS3 upgrade, is the one of the $\Lambda_b \rightarrow \Lambda_c^+ + \pi^-$. The study of the enhancement of the Λ_b measurement with the ITS3 upgrade with respect to the ITS2, is the topic of the second part of the current thesis and it is presented in Chapter 4.

Detector physics and technologies

2.1 Tracking detectors

*T*HE tracking detectors of the hep experiments are responsible for the precise determination of the particle tracks and the decay vertices. After the beam collision the charged particles are travelling in a curved path, due to the applied magnetic field, until they decay to their daughter particles which start their own journey. During their movement and depending on their characteristics, namely their mass and transverse momentum, they leave their footprint on the detectors through the energy deposition in the detector material. By tracing all the track points on the detector the track reconstruction is done and the particle's charge and momentum can be calculated. In the case that the mother particle was produced at the collision point, the particle is referred to as prompt particle and the reconstructed point where it was produced is the primary vertex. For particles with small decay length it is usually very hard to separate the primary to the secondary vertex, the vertex where the prompt particle decays to each daughters. For this reason optimized impact parameter resolution is required in order to extract precise information for the particles and their decays.

The determination of the particle's transverse momentum is done by the measurement of the track's curvature in the magnetic field. A point charge moving in a magnetic field experiences the Lorentz force which in the case of a particle of charge q moving in a constant magnetic field is described by

the Equation 2.1 [27].

$$\begin{aligned}
 \vec{F} &= |q| (\vec{u} \times \vec{B}) \implies \\
 p_T &= |q| B R \implies \\
 p_T \left[\frac{\text{GeV}}{c} \right] &= 0.3 |z| B[\text{T}] R[\text{m}]
 \end{aligned} \tag{2.1}$$

Where:

B : is the constant magnetic field in Tesla.

R : is the bending radius of the track.

z : is the particle charge in units of the elementary charge, $z=q/e$.

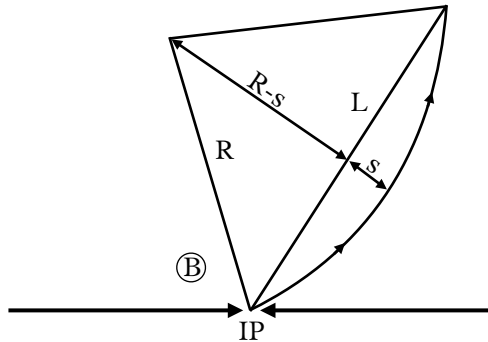


Figure 2.1: Schematic representation of the track geometry for the sagitta calculation.

The bending radius R is obtained from a circle fit in the measured points along the track. For the uncertainty on the transverse momentum measurement, in a simple case, the uncertainty on the bending radius is calculated through the uncertainty on the sagitta measurement which is obtained by the geometry of the system demonstrated in Figure 2.1. The

approximate relation between the bending radius and the sagitta, in the case of $s \ll L$ is expressed in the Equation 2.2.

$$s = \frac{L^2}{8R} \quad (2.2)$$

By combining the Equations 2.1 and 2.2, the transverse momentum resolution is calculated and expressed in Equation 2.3 indicating a dependence on the magnetic field and on the path length, the increased values of which contribute to the improvement of the momentum resolution.

$$\left. \frac{\sigma_{p_T}}{p_T} \right|_{track} = \frac{\sigma_s}{s} = \sigma_s \cdot \frac{8 p_T [\text{GeV}/c]}{0.3 |z| (L[\text{m}])^2 B[\text{T}]} \quad (2.3)$$

The high precision measurement of the sagitta is strongly contributing to the small uncertainty on the transverse momentum measurement. The uncertainty on the track measurement depends on the single point accuracy $\sigma_{r\phi}$ determined by the intrinsic detector resolution, the number of single point measurements and the space in between them along the track [28] [29]. The intrinsic detector resolution depends on the detector characteristics.

In the transverse momentum uncertainty there is an additional term due to the multiple scattering. When charged particles are traversing a medium they get deflected by many small angle scatters.

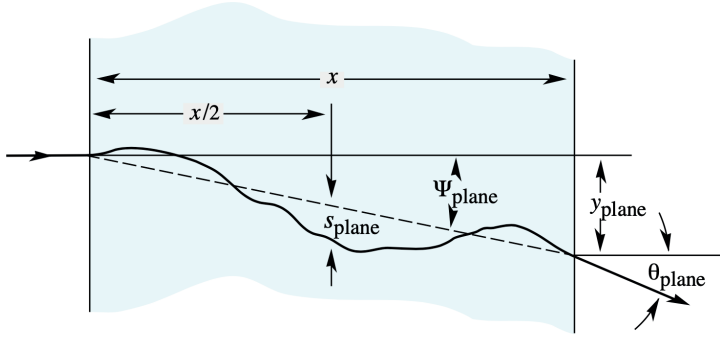


Figure 2.2: Multiple scattering of an incident particle in the material. The different quantities for the multiple scattering characterization are demonstrated. [30].

The Coulomb scattering distribution is well described by the theory of

Molière [31] and in the case of small angles a Gaussian approximation is used for the deflection angle estimation, Equation 2.4, which is used for the calculation of the multiple scattering uncertainty term [29]. The two uncertainty contributions, the one of the track measurement and the one of the multiple scattering are added in quadrature for the calculation of the transverse momentum uncertainty.

$$\theta_{ms} = \frac{13.6\text{MeV}}{\beta c p} z \sqrt{\frac{X}{X_0}} \cdot [1 + 0.038 \ln \frac{X}{X_0}] \quad (2.4)$$

Where:

p : is the momentum.

βc : is the velocity.

z : is the charge number of the incident particle.

$\frac{X}{X_0}$: is the thickness of the scattering medium in radiation lengths.

In addition to the momentum measurement, the determination of the track's impact parameter and its resolution is necessary for the particle tracking. The impact parameter d_0 is defined as the closest distance of the track from the primary vertex of a collision. A high precision measurement of the impact parameter is required and can be obtained by minimizing the uncertainty contributions. The uncertainty of the impact parameter consists of two terms, the uncertainty due to the detector geometry and the uncertainty due to the multiple scattering, Equation 2.5, which are added in quadrature. If a two layer detector design is taken under consideration, Figure 2.3, with the innermost layer directly positioned on the beam pipe and having a total thickness X and a joint radiation length X_0 , the $\sigma_{geometry}$ is given by the Equation 2.6 [32].

$$\sigma_{d_0} = \sigma_{geometry} \oplus \sigma_{MS} \quad (2.5)$$

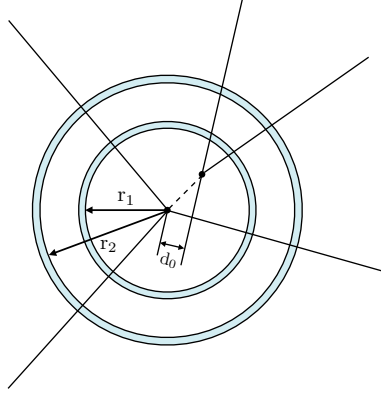


Figure 2.3: *Schematic representation of the impact parameter of a track with measured points on a two layer detector.*

$$\sigma_{geometry} = \sqrt{\frac{r_2^2 \sigma_1^2 + r_1^2 \sigma_2^2}{(r_2 - r_1)^2}} \quad (2.6)$$

The $\sigma_{geometry}$ depends on the radius of the detector layers and on the space point resolution of the track points. In order to minimize the uncertainty on the measurement, high precision of the tracking points is required and the first detector layer should be installed as close as possible to the interaction point. The second term of the resolution, the one imposed by the multiple scattering, with the aforementioned assumptions on the simplified detector design, is given by the Equation 2.7 and it is derived using the θ_{ms} Equation 2.4.

$$\sigma_{MS} \approx r_1 \theta_{ms} \quad (2.7)$$

As it is demonstrated, the d_0 resolution as well as the momentum resolution strongly depend on the detector design and on the effects of the multiple scattering. In order to minimize the uncertainties, especially on the measurements of low momentum particles that ALICE will aim in the next runs, the reduction of the detector material budget and of the radial distance of the first layer to the interaction point are among the priorities of the ALICE ITS upgrades.

2.2 Particle interactions with matter

The detection of particles and their characteristics is done through their energy deposition in the detector material. In order to understand the energy deposition mechanisms of particles, the interaction mechanisms with matter will be discussed. Particles can interact with atoms, with atomic electrons and with nuclei. The interaction mechanisms of heavy (p, d) and light (e^- , e^+) charged particles as well as the ones of photons are described in the following session.

Charged particles are surrounded by a Coulomb field and they can interact with electrons or with nuclei of atoms in matter. Coulomb interactions with nuclei are responsible for the angular deflection of charged particles in a material. In the elastic scattering, during the multiple scattering interactions of charged particles with the nuclei, the kinetic energy of the particle in the center of mass frame is conserved, but the propagating direction of the particle is modified. Detailed description on the quantitative effect of the multiple scattering was given in the previous section. In the inelastic scattering, when a particle is traversing a medium, the coulomb interactions of the particle with the atomic electrons of the material lead to the excitation or the ionization of atoms due to the energy absorption. The different effects of the charged particles' interaction mechanisms are described below [33].

- **Ionization**

When a charged particle is traversing the active material of the detector it interacts with the atomic electrons that are in the outer shell of the atom. If the incident particle transfers enough energy to the electron, larger than the binding energy, then the electron is completely removed from the atom and can move freely.

- **Excitation**

In the case of excitation, the incident particle excites the electrons of the atom by transferring enough energy to them to move from a lower to a higher energy level.

- **Bremsstrahlung**

The inelastic scattering of charged particles with the atomic nuclei leads to the production of bremsstrahlung photons, resulting to emission of electromagnetic radiation.

- **Cherenkov radiation**

When a charged particle is travelling in a medium with velocity higher than the speed of light in that medium, Cherenkov light is emitted in a conical shape.

- **Transition radiation**

The emission of transition radiation occurs when a charged particle crosses the boundary of two media with different dielectric constants.

The most relevant interaction mechanisms of photons are described below.

- **Photoelectric effect**

When a photon is totally absorbed by a material and enough energy is transferred to the bound atomic electrons, the latter ones start being emitted. This process is described as the photoelectric effect and leads to the emission of photoelectrons.

- **Pair production**

Another effect of the photon interactions is the pair production. During the pair production a photon is transformed into an electron-positron pair. The minimum photon energy in order for the pair production to take place is the sum of the rest mass energies of the electron and the positron, 1.02 MeV. The interaction of the positron with one of the electrons of the detector material can lead to annihilation. Through the annihilation process two photons of 0.511 MeV energy will be created.

- **Compton scattering (Incoherent scattering)**

The Compton scattering is the effect of the inelastic scattering of a photon with a loosely bound electron. The incident photon is scattered by the electron, which is referred to as recoil electron after the scattering, and the photon is deflected from the initial path. At the same time part of the initial kinetic energy of the photon is transferred to the recoil electron that is ejected. The energy transfer depends on the energy of the incident photon and on the scattering angle.

In addition to the above mechanisms, photons experience further interactions, namely the Rayleigh and Thomson scattering as well as photonuclear interactions.

2.2.1 Bethe-Bloch

Throughout the inelastic interactions of the charged particles with the detector material and more precisely during the processes of ionization and excitation, the particles are transferring part of their energy to the detector material. The average rate of the particle's energy loss in the detector material is known as stopping power and it is described by the Bethe-Bloch Equation 2.8¹ per unit path length of a particle [30].

$$-\left\langle \frac{dE}{dx} \right\rangle = K \frac{Z}{A} \frac{z^2}{\beta^2} \left[\frac{1}{2} \ln \frac{2m_e c^2 \beta^2 \gamma^2 W_{max}}{I^2} - \beta^2 - \frac{\delta(\beta\gamma)}{2} \right] \quad (2.8)$$

Where:

$K = 4 \pi N_A r_e^2 m_e c^2$: is a constant where m_e the electron mass, r_e the classical electron radius and N_A is the Avogadro number.

β : is the ratio of the particle's velocity over the speed of light .

γ : is the relativistic Lorentz factor.

Z : is the atomic number of the absorber.

A : is the atomic mass of the absorber.

z : is the charge of the incident particle in electron units.

W_{max} : is the maximum energy that can be transferred in a single collision.

I : is the mean excitation energy of the atom.

$\delta(\beta\gamma)$: is a density effect correction.

As it is shown by the Bethe-Bloch formula, the mean rate of the energy loss depends on the velocity and the charge of the incident particle as well as on the characteristics of the traversed medium. However there are cases where the energy transfer that is considered is restricted, $T \leq W_{cut} \leq W_{max}$. In very thin detector layers the energy that is deposited in the material can be less than the maximum possible due to energetic knock-on electrons (δ

¹This form of the equation stands for the region $0.1 \lesssim \beta \gamma \lesssim 1000$ with an accuracy of a few percent.

electrons), that escape and carry off fraction of the energy. In cases like this, the Equation 2.8 is modified and the restricted energy loss rate is given by the Equation 2.9 [30].

$$-\left. \frac{dE}{dx} \right|_{T < W_{cut}} = K \frac{Z}{A} \frac{z^2}{\beta^2} \left[\frac{1}{2} \ln \frac{2m_e c^2 \beta^2 \gamma^2 W_{cut}}{I^2} - \frac{\beta^2}{2} \left(1 + \frac{W_{cut}}{W_{max}} \right) - \frac{\delta}{2} \right] \quad (2.9)$$

2.2.2 Straggling function

The distribution of the energy lost by a particle that is crossing a path x is given by the energy straggling function. The amount of the energy lost it is affected by statistical fluctuations on the number of the collisions and on the energy transfer of every collision [34]. Consequently, the probability density function (PDF) that describes the particle's energy loss depends on the thickness of the material. In the case of thick absorbers where the number of collisions is larger and the energy loss exceeds the 1/2 of the initial energy the PDF is a Gaussian approximation. For thin absorbers the energy loss is described by the Landau distribution. In this case, the mean energy loss is displaced from the peak due to the high energy tail. The position of the peak defines the most probable value (MPV) of the energy loss. In the case of ultra thin absorbers the energy loss distribution is well described by the Bichsel functions [35]. In particular for very thin active silicon layers the full width half maximum, w , of the energy loss distribution per unit thickness, is broader than in thicker layers and the MPV of the energy loss per unit thickness shifts towards lower values as the thickness of the silicon becomes smaller, Figure 2.4.

2.3 Silicon detectors

Silicon (Si) is one of the most abundant elements that can be found in nature, widely used in many applications and with a long tradition in the trackers of high energy physics experiments. Silicon belongs to the family of semiconductors which are characterized by their electrical conductivity lying in between the range of a conductor and an insulator. The inner structure and the energy bands of silicon are described in the following section.

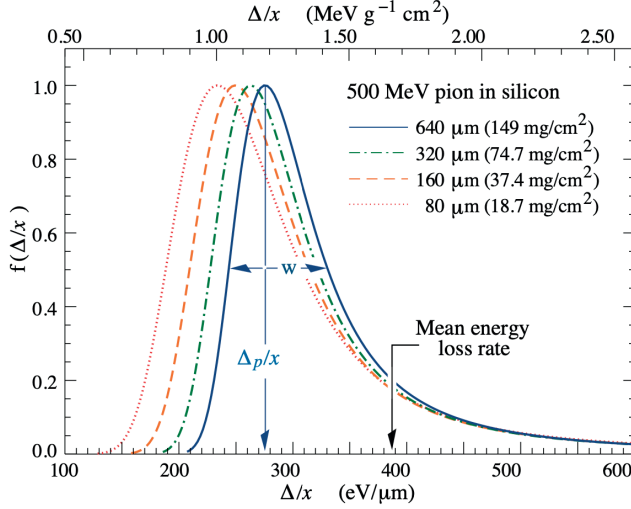


Figure 2.4: Straggling functions of 500 MeV pions traversing silicon layers of different thickness. The PDF's are normalized to unity at the MPV Δ_p/x . [36]

2.3.1 Band Model

When atoms are bound to form solid state structures, the atomic electrons share common energy bands. The theoretical model that describes the energy bands is the band model also referred to as solid state band theory.

In the case of pure semiconductors, the intrinsic semiconductors, and more particularly in the pure silicon case, each Si atom has four valence electrons. The remaining four electrons create covalent bonds that are shared with neighbouring silicon atoms. In this way a semiconductor structure is formed as it is demonstrated in Figure 2.5. The energy bands that are described by the band theory are demonstrated in Figure 2.6 and are described below.

- **Valence band**

The valance band, is the energy band that is usually fully or partially filled. In intrinsic semiconductors, at the temperature of 0 K all the valence electrons that are bonded with covalent bonds are lying in the valence band.

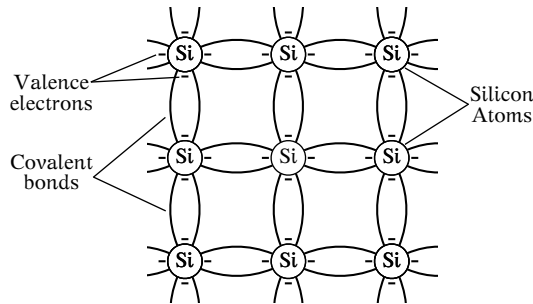


Figure 2.5: *Atomic structure of pure silicon*

- **Band gap**

Above the valence band lies the band gap which cannot be occupied. The size of the band gap is indicative of the electrical conductivity of a material. In the case of conductors there is no band gap, whereas in the insulator case the band gap is very large. The size of the band gap in Si at room temperature is $E_g = 1.12$ eV.

- **Conduction band**

Above the band gap there is the conduction band which is not or partially filled. In the case of ionization of an atom, if sufficient energy is given to the valence electrons they can break the valence bonds and jump from the valence band to the conduction band leaving behind a hole. In the case of Si the average energy required for the creation of an electron-hole pair is 3.6 eV, which is larger than the E_g since part of the energy goes into crystal excitations [37].

The conductivity of the semiconductors can be altered by increasing the temperature or by adding impurities in a pure structure, a process called doping. The covalent bonds of the shared electrons in a pure silicon structure are very strong and they cannot break at 0 K temperature. If the temperature is increased in the material, it will be adsorbed by an electron which will break the bond and if the thermal energy is high enough it will move to the conduction band, creating a hole in the valence band. The thermal generation of electron-hole pairs increases the intrinsic charge carrier concentration. The

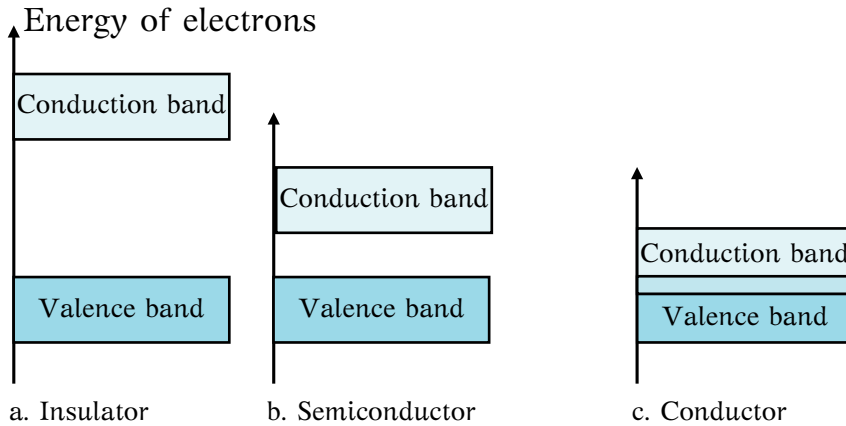


Figure 2.6: *Energy bands of semiconductors, conductors and insulators*

outcome of this process is the decrease of the material resistivity and the increase of the semiconductor conductivity [38].

A different way to alter the conductivity is by adding impurities in the structure with doping. The doping is done by replacing one silicon atom by the atom of a neighbouring element to the Si in the periodic table. There are two different types of doping that are presented below.

- **p-type**

In the p-type, the doping is done by replacing the Si atom by another one from the III group elements which has three valence electrons, usually a Boron (B) atom. With the replacement of the Si atom, only three covalent bonds will be formed leaving one hole in the crystalline structure. In the p-type doping the number of holes is larger than the number of free electrons.

- **n-type**

The n-type doping is usually done by replacing with V group elements, like Phosphorus (P) atoms which have five valence electrons. In this case all the valence electrons of the Si make covalent bonds with the P electrons and one electron will remain leading to an excess of electrons. This will result to a n-type semiconductor.

2.3.2 p-n junction

The p-n junction or p-n diode, is created when two differently doped silicon layers an n-type and a p-type are brought together. When an n-type and a p-type materials are joint the concentration difference leads to the diffusion of the charge carriers of the one side into the differently doped side. The electrons of the n-type cross the junction and recombine with the holes in the p-type. Similarly the holes diffuse into the n-type. This procedure creates positive and negative atoms near the junction, which is depleted from the free electrons and holes. The region in the p-type that has only negatively charged ions together with the region in the n-type that remains with positive ions is defined as the depletion region, or space-charge region as it is also named. In the depletion region an electric field is developed resulting to a built-in potential V_{bi} , Equation 2.10, which does not allow the electrons to cross the junction.

$$V_{bi} = \frac{k_B T}{q} \ln \left(\frac{N_A N_D}{n_i^2} \right) \quad (2.10)$$

Where:

k_B : is the Boltzman constant.

T : is the temperature.

q : is the unit charge.

N_D, N_A : are the doping concentrations of donors and acceptors.

n_i : is the intrinsic carrier concentration.

By applying external voltage to the diode, the diode can be biased to the forward or to the reverse direction. In the forward biasing case, positive voltage is applied to the p-type and negative to the n-type. In this case, the width of the depletion region will be reduced since the external voltage leads to the reduction of the voltage across the junction from V_{bi} to $V_{bi} - V_{fb}$.

On the contrary, in the reversed bias case the negative voltage is connected to the p-type and the positive to the n-type. The applied external voltage has the same direction as the V_{bi} and the free charge carriers are further removed from both sides. In this way the size of the depletion region is increased as

it is expressed in Equation 2.11. The energy band diagram in case of reverse bias is demonstrated in Figure 2.7.

$$W(V) = \sqrt{\frac{2\epsilon\epsilon_0}{q} \frac{N_D + N_A}{N_A N_D} (V_{bi} + V_{rb})} \quad (2.11)$$

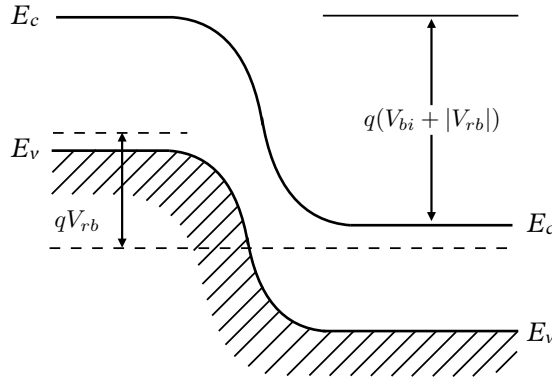


Figure 2.7: Schematic representation of the energy band of a reversed bias *p-n* junction.

However, there are a few charge carriers present in both regions. These minority charges can cross the depletion region and introduce a current flow which is called leakage current. The leakage current is induced even in the case of an ideal diode, by the diffusion of the charge carriers through the space-charge region. However, the most dominant contribution to the leakage current is usually from the thermal generation of electron-hole pairs in the space-charge region due to impurities in the material and defects in the silicon that are acting as generation-recombination centres [39].

The volume of the depletion region can be also increased by increasing the resistivity of the material. The resistivity of a semiconductor is given by the Equation 2.12.

$$\rho = \frac{1}{\sigma} = \frac{1}{q(\mu_e n + \mu_h p)} \quad (2.12)$$

Where:

σ : is the conductivity.

μ_e, μ_h : are the mobility of electrons and holes.

n, p : are the negative and positive charge carrier concentrations.

Another important characteristic of the diode is the junction capacitance which should be kept at low values in order to avoid limitations on the detector response. The capacitance to the backside, similarly to the case of a parallel plate capacitor, is given by Equation 2.13, indicating a dependence on the width of the depletion zone which can be adjusted through the external bias voltage. Consequently, an increase in the bias voltage leads to the reduction of the junction capacitance.

$$C = \epsilon \epsilon_0 \frac{A}{d} \quad (2.13)$$

Where:

ϵ : is the dielectric constant of the material.

ϵ_0 : is the permittivity of free space.

A : is the junction area.

d : is the width of the depletion zone.

All the aforementioned characteristics of a p-n junction, the resistivity, the depletion width, the capacitance play a crucial role in the detector performance and need to be optimized in the detector configuration.

2.3.3 Monolithic Active Pixel Sensors

As was discussed in the beginning of this chapter, the requirements of HEP experiments for their tracking systems impose the need of low material budget detectors that provide an optimized impact parameter resolution. Towards this direction, the Complementary Metal-Oxide Semiconductor (CMOS) Monolithic Active Pixel Sensors (MAPS) are currently the best choice for the trackers in many HEP experiments, namely for the Solenoid Tracker at RHIC (STAR) and ALICE. The use of CMOS technology in MAPS allows the elimination of additional electronics for the sensor readout since the readout and the silicon are integrated in one compact device, contrary to hybrid detectors where the

Application Specific Integrated Circuit (ASIC) is bump-bonded to the sensor. Consequently, the thickness of the detector is significantly reduced leading to ultra thin pixel detectors and reducing the effect of the multiple scattering.

Charge generation and signal formation

The reduction of the thickness of the active area implies that the generated charge is reduced as well. In silicon sensors with an active layer of $\sim 300 \mu\text{m}$ the generated charge produced by a Minimum Ionizing Particle (MIP) is larger than the charge generated in a MAPS with an epitaxial layer of $25 \mu\text{m}$ thickness. In the latter case a traversing MIP generates approximately $1500 e^-$. A lower collected charge Q_{col} results to a lower signal $\Delta V_{col} = Q_{col} / C_p$ with C_p the pixel-input capacitance. In order to compensate for this the pixel-input capacitance has to be reduced. The optimization of the Q_{col} / C_p ratio is of paramount importance for MAPS and is a key point during the manufacturing and the design of the sensor.

The signal formation on the collecting electrode is described by the Ramo-Shockley theorem [40] [41]. The charge starts being detectable not when it reaches the electrode but already the moment that it starts moving. The movement of the charge e with velocity v induces a current on the electrode given by Equation 2.14.

$$i = e E_w v \quad (2.14)$$

Where:

E_w : is the weighting field.

The weighting field describes the coupling of the charge to the collecting electrode and it can be calculated for different electrode arrangements, with grounded electrodes or electrodes connected with impedance elements, but also for non-linear detector materials [42] [38].

The weighting field can be obtained from the weighting potential. For infinite electrodes the weighting potential depends linear on the position (depth) in the sensor. For finite electrodes, in particular when the electrode size is in the same order as the sensor thickness or below, this is no longer the case.

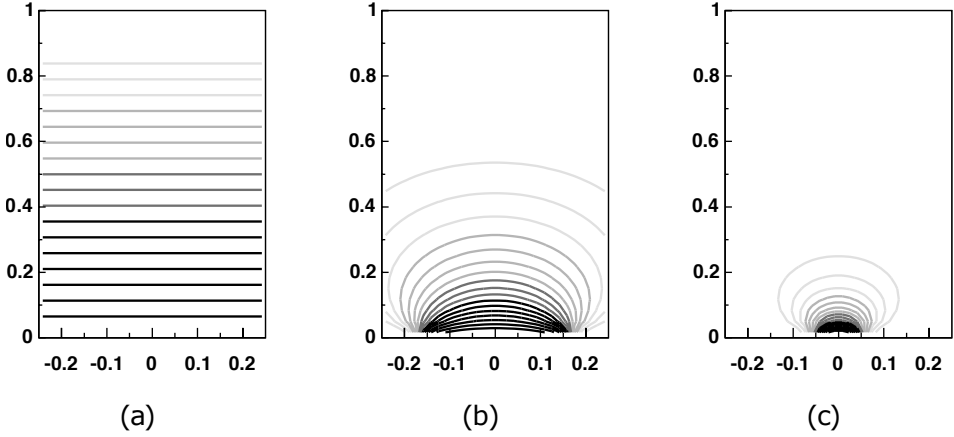


Figure 2.8: *Weighting potential for three different detector configurations. Plot (a) corresponds to the weighting potential in the case of infinite parallel plates, while plot (b) and (c) correspond to sensors with collection electrodes of size 1/3 and 1/10 of the wafer thickness respectively [39].*

In pixel detectors where the collecting electrode is smaller than the wafer thickness, the weighting potential becomes considerable in the region around the electrode. For smaller dimensions of the collecting electrode, the region where the weighting potential approaches zero is increased. The weighting potential for different detector configurations is demonstrated in Figure 2.8. Due to the above effect which is also known as small pixel effect, most of the signal is induced for the charge moving in the proximity of collection electrode.

Once all the charge has reached the collection electrode, the collected charge is obtained from the integral of the induced signal. It is thus important, the integration time of the electronics to be larger than the charge collection time. This is also the case for the sensors of the upgraded ALICE ITS that are discussed in Chapter 3.

MAPS inner structure

The detector design of a standard MAPS contains a lightly doped high resistivity p^- type epitaxial layer on top of a highly doped p^+ substrate. In between the p^- type epitaxial layer and the p^+ substrate an isotype junction

is created, due to the difference in the doping concentrations, resulting to a reflective barrier potential which is given by Equation 2.15.

$$V = \frac{k_B T}{q} \ln\left(\frac{N_+}{N_-}\right) \quad (2.15)$$

Where:

N_+ and N_- : are the high and low doping concentrations, respectively, which differ by several orders of magnitude.

The role of the barrier potential is to reflect the electrons that were created in electron-hole pairs from the ionization of the material from an incident particle, and force them to stay in the epitaxial layer. Inside the epitaxial layer the electrons thermally diffuse until they reach the depletion region of the p-n junction or until they recombine with holes in the material. The p-n junction is formed by the epitaxial layer and the N-well charge collecting diode, that is placed on top of it. Once the electrons enter the depletion region they drift until they get collected by the N-well.

However, part of the electrons will get collected by the other N-wells, of the PMOS transistors, that are on top of the epitaxial layer. This results to penalization of the charge collection and to a low efficiency. In order to overcome this problem, a quadruple-well process is developed in the standard, bulk CMOS process, that allows the presence of both NMOS and PMOS transistors on the epitaxial layer without influencing the charge collection [43]. During this process a deep P implant, deep P-well, is added underneath the N-well of the PMOS transistor creating a barrier with the epitaxial layer. In this way the charge carriers that thermally diffused towards the N-well, get reflected back in the vicinity of the epitaxial layer.

The charge collection by diffusion in MAPS is very slow and the sensors are sensitive to radiation damage effects [44]. In order to increase the radiation hardness of MAPS the charge collection by drift needs to be enhanced. This is usually done by increasing the depletion region around the p-n junction, the region where the electrons drift. In the case of MAPS where $N_D \gg N_A$ the depletion width Equation 2.11 is modified as Equation 2.16.

$$W(V) = \sqrt{\frac{2\epsilon\epsilon_0}{q} \frac{(V_{bi} + V_{rb})}{N_A}} \quad (2.16)$$

The depletion region is increased in case of a high resistivity epitaxial layer [45] but as it was also previously discussed by applying reversed bias

voltage to the diode. The latest versions of MAPS contain a high resistivity epitaxial layer and bias voltage is applied that leads to a partially depleted sensor. However, the rapidly evolving MAPS technology is moving towards the direction of fully depleted sensors, higher in radiation hardness.

Upgrade of the ALICE Inner Tracking System

3.1 Detector specifications

*T*HE upgrade of the ALICE Inner Tracking System during the LS2 along with the increased instantaneous luminosity in Run 3 will address the physics questions of the ALICE program through high precision measurements of heavy flavour hadrons, low-mass dileptons and quarkonia. In order to access these measurements in a wide momentum range and increase their precision, a large amount of statistics needs to be accumulated and the upgrade strategy of the ITS has to offer improved pointing resolution and tracking efficiency. In view of this direction an optimized detector design and cutting edge detector technologies were used in order to meet the requirements of an optimized tracker with low material budget installed at the minimum possible distance to the interaction point. The key features of the ITS upgrade are described below.

- **Distance to the interaction point**

The innermost layer of the upgraded ITS will be positioned at a radial distance of 23 mm from the interaction point, closer than the ITS1, benefiting from the reduction of the beam pipe radius.

- **Detector technology**

The 6 layers of SPD, SDD and SSD of the ITS1 will be replaced by seven layers of CMOS MAPS. The use of pixel detectors, with a reduced

pixel pitch from the SPD value of $50 \times 425 \mu\text{m}^2$ down to $29 \times 27 \mu\text{m}^2$ of the ALPIDE, in all detector layers will contribute to the improvement of the pointing resolution and tracking efficiency.

- **Reduction of material budget**

The use of MAPS that combine the silicon active area with the electronics in one device allows the reduction of the thickness of the sensor to values down to $50 \mu\text{m}$ for the inner layers. The power consumption is also reduced allowing the reduction of material budget connected to power and signal cabling by a factor of 5. The above factors along with modifications in the support structures and the cooling reduces the material budget of the inner layers from $1.14 \%X/X_0$ (SPD) down to $0.35 \%X/X_0$.

- **Read-out rate**

The detector read-out rate capability will increase from the current 1 kHz to 100 kHz and to 400 kHz for Pb–Pb and p–p collisions respectively. This is a factor 2 more than the required interaction rate for Run 2.

All the above modifications will improve the pointing resolution and the tracking efficiency as it is quantitatively demonstrated in Figure 3.1. For the corresponding performance plots real data of Pb–Pb events were used and additional were simulated with a MC tool taking into account the upgrade specifications. The pointing resolution in the momentum region of $0.5 \text{ GeV}/c$ will be improved by a factor of 3 and 5 in the $r\phi$ and z plane respectively. The tracking efficiency will be enhanced in the low momentum region benefiting from the increased number of track points due to the installation of an additional detector layer and of the improved single point resolution.

3.2 The ALPIDE sensor

The ALPIDE sensor was designed for the upgrade of the ALICE ITS in order to comply with the upgrade requirements set by the physics goals and the experimental conditions. All the sensor requirements of the ITS upgrade concerning the radiation hardness, the fake hit rate, the spatial resolution and other characteristics regarding the inner and outer layers of the ITS are described in Table 3.1 [46].

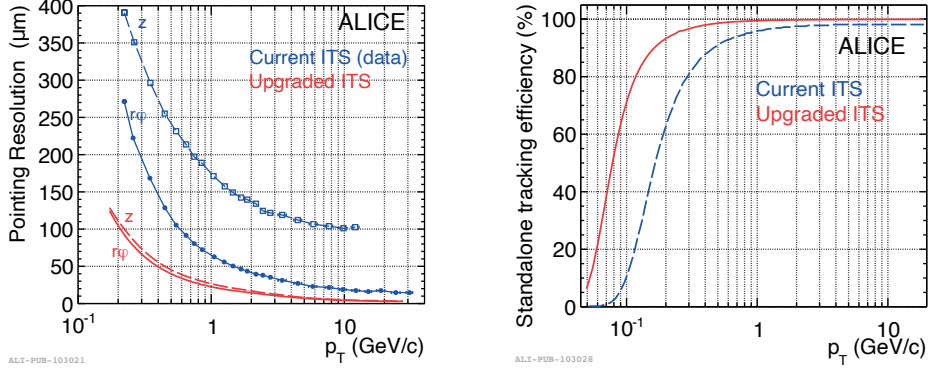


Figure 3.1: Pointing resolution (left) and tracking efficiency (right) as function of the transverse momentum, with ITS1 and ITS2.

Parameter	Inner Barrel	Outer Barrel
Chip size	15 mm × 30 mm	
Chip thickness	50 μm	100 μm
Spatial resolution	5 μm	10 μm
Detection efficiency	> 99%	
Fake hit rate	$< 10^{-6} \text{ event}^{-1} \text{ pixel}^{-1}$	
Integration time	< 30 μs	
Power density	$< 300 \text{ mW/cm}^2$	$< 100 \text{ mW/cm}^2$
TID radiation hardness ¹	2700 krad	100 krad
NIEL radiation hardness ¹	$1.7 \times 10^{13} \text{ 1 MeVn}_{\text{eq}}\text{cm}^{-2}$	$1 \times 10^{12} \text{ 1 MeVn}_{\text{eq}}\text{cm}^{-2}$

Table 3.1: Sensor requirements for the upgrade of the ALICE ITS [46] [47] [48]

Different specifications of MAPS prototypes were evaluated in order to optimize the detector performance and finalise the design of the ALPIDE. The different parameters that were studied included the pixel size, the thickness of the epitaxial layer, the geometry of the collection diode and other specifications [44]. The common goal for the fine tuning of the aforementioned parameters was the optimization of the Q_{col}/C_p ratio. An increased Q_{col}/C_p results to

¹The values include a safety factor of ten.

an improved signal to noise ratio. The final design characteristics of the ALPIDE sensor are described in the following section.

The performance of the ALPIDE was evaluated with laboratory measurements and with test beams and was found to comply with the requirements of the detection efficiency and of the fake hit rate [49]. Indicatively, the detection efficiency and the fake hit rate were studied as function of the threshold and revealed that for a wide range of charge thresholds the ALPIDE is well inside the set requirements. In general, low values of the charge threshold increase the detection efficiency. Nevertheless, the threshold should be as low as it allows the fake hit rate to be in the acceptance. From the above studies the optimal threshold range was revealed. However, chip to chip variations in terms of the charge threshold exist. The effect of the chip by chip threshold tuning is one of the electrical characteristics that are studied with the developed software that is in detail described in this chapter. It will be demonstrated that a uniform response of the sensors throughout the modules and the staves can be achieved.

3.2.1 ITS in the MAPS era

The ALPIDE sensor, the building block of the upgraded ITS, is member of the family of CMOS MAPS. The selection of the MAPS technology in the ALICE tracker was done towards the direction of the reduced material budget and the high granularity that monolithic sensors can offer. The ALPIDE chip is fabricated by TowerJazz with the 180 nm CMOS Imaging Sensor process with full in-pixel circuitry. The sensor covers an area of 15 (Y) \times 30 (X) mm and hosts 1024 \times 512 pixels arranged in columns and rows respectively. In the direction of an improved charge collection a high resistivity ($> 1 \text{ k}\Omega \text{ cm}$) p-type epitaxial layer is built on top a p-type substrate. The implementation of full CMOS circuitry in every pixel is possible with the presence of both types of NMOS and PMOS transistors on top of the p-type epitaxial layer. As it was previously discussed, the implementation of this feature is allowed with the presence of a deep P-well that is shielding the N-well, avoiding a possible charge loss. One of the benefits of this approach is that the signal discrimination is done inside every pixel with the realization of in-pixel discriminators. This feature allows for a more efficient read-out scheme than the one of the rolling shutter, in which the discriminators are placed in the end-of-column circuitry. In the latter case, the analogue signals of the pixels are driven through the column lines in order to be discriminated, resulting to

a sensor with lower speed and higher power consumption [50]. Finally, the small size of the N-well diode, $\sim 2 \mu\text{m}$ diameter, significantly smaller than the pixel pitch, results to a small capacitance.

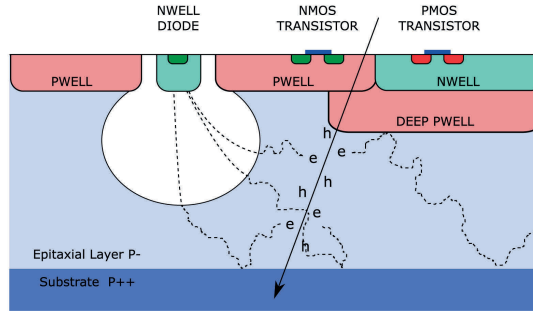


Figure 3.2: *Schematic representation of a MAPS inner structure and operation principle.*

The key features of the TowerJazz process and the cross section through a MAPS are represented in Figure 3.2. When an incident particle is traversing the silicon it ionizes the material creating electron-hole pairs. The resulting charge is moving towards the depletion zone, and it is collected by the N-well diode. The charge collection from this area is done by drift and from the non depleted region by diffusion. The size of the depletion volume in the ALPIDE can be increased by applying back bias voltage resulting in better charge collection with a partially depleted sensor.

3.2.2 Front-end electronics, architecture and features

Once the charge is collected by the N-well diode it is propagated to the electronic circuit of the pixel which consists of an input stage, that includes the aforementioned collection diode, a diode reset circuit and an injection capacitor, an analogue front-end part (amplifier/shaper and discriminator) and a digital section. The silicon active area and the front-end of the pixel are always active. The collection of the charge deposited by a particle, creates a voltage drop in the input node `pix_in`. The charge collection time is below 100 ns and within 100 μs the voltage is reset to the baseline value. The reset of the pixel is done by the diode reset which features a small size and has a small contribution to the input capacitance. The input capacitance consists of the junction capacitance and of the circuit capacitance. The latter one

consists of the capacitance of the input transistor, of the routing lines and of the reset mechanism. The injection of test charges in the circuit is also possible by applying a voltage step VPULSE through the injection capacitor C_{inj} .

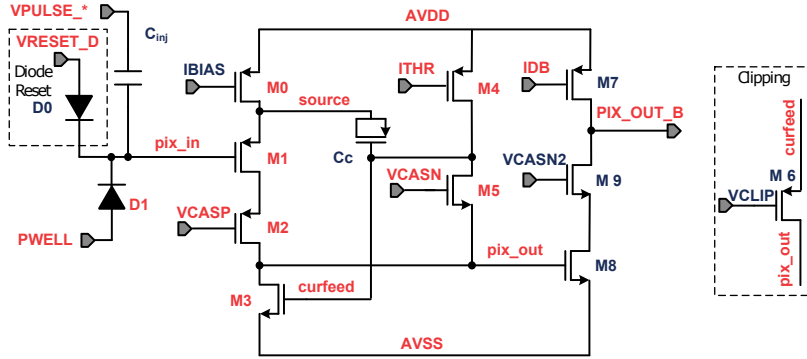


Figure 3.3: Schematic representation of the analogue part of the ALPIDE, consisting of the collection diode $D1$, the reset diode $D0$, the injection capacitor C_{inj} , the amplifier/shaper and the discriminator.

The induced voltage step goes through the pix_in node to the analogue pixel front-end for amplification, shaping and discrimination. In this region an analogue pulse is shaped, with peaking time less than $2\ \mu s$, which is compared to the threshold level. The threshold level can be adjusted for all the pixels of the chip globally, by tuning the $ITHR$, the $VCASN$ and IDB Digital-to-Analogue Converter (DAC) 8-bit settings. The level of the threshold increases with increasing $ITHR$ or IDB and decreases with an increasing value of the $VCASN$. In addition a clipping mechanism is present in the circuit that limits the pulse duration for very large signals. If the voltage at the pix_out is higher than the threshold, a discriminated output PIX_OUT_B is generated [51].

The PIX_OUT_B node is connected to the digital part of the circuit that includes a multiple-event memory region (3 hit storage registers), a register for masking the pixel and a pulsing logic. When a STROBE signal is sent to the pixel ²a hit is recorded if the STROBE arrives during the time the pulse is above threshold. In this case the hit information is stored in a state register. When a hit is recorded on a pixel and only then the pixel is

²STROBE signals are sent globally to the pixels

read-out, the information about its address are sent to the periphery of the chip through the Address-Encoder Reset-Decoder (AERD) circuit [52] and the pixel is reset in a state ready to record the next hit. The pixel columns of the chip are grouped in double columns, each one of them sharing a common priority encoder located in the in between region of the columns, Figure 3.4. This hit-driven readout architecture with zero-suppression allows a sufficient reduction of the readout time and the power consumption.

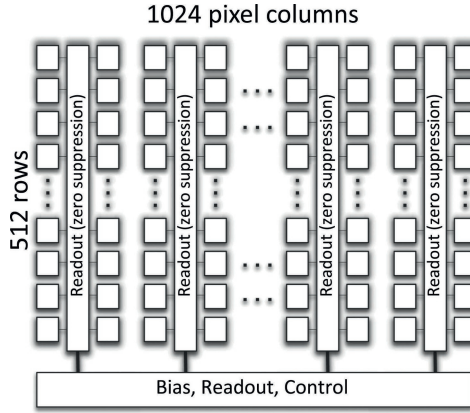


Figure 3.4: Readout architecture of the ALPIDE sensor.

3.3 Detector layout

The upgraded ITS covers an active silicon area of 10 m^2 offering a radius coverage of 22–400 mm and a pseudorapidity coverage of $|\eta| < 1.22$ for tracks from 90% of the luminous region. The detector complies with the radiation level requirement of 2.7 Mrad TID and $1.7 \times 10^{13} \text{ 1 MeVn}_{\text{eq}} \text{ cm}^{-2}$ NIEL and will operate in a 0.5 T magnetic field. As it is shown in Figure 3.5 it consists of seven detector layers which are organized in two barrels, the inner barrel and the outer barrel. An optimized mechanical design is used that allows a smooth installation of the inner barrel and an easy removal for future maintenance. The design is similar for the two barrels, sharing the same technological solutions but adjusted to the requirement of reduced material budget for the inner layers. The outer barrel is subdivided into two middle layers and two outer layers.

The outer layers consists of staves, each one of them is made up from

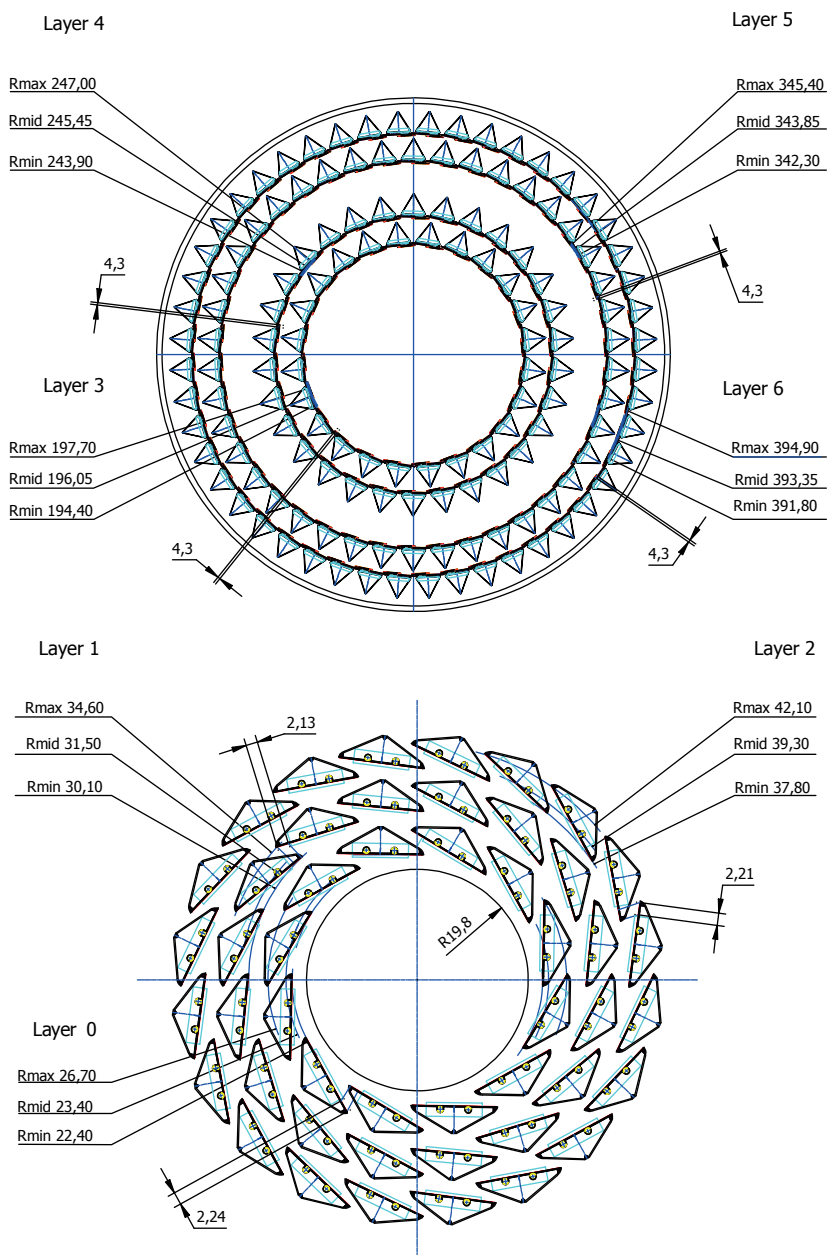


Figure 3.5: Schematic representation of the detector layers of the inner (bottom) and outer (top) barrels.

two half-staves that host two rows of seven outer barrel modules. The same configuration is used in the middle layers with the difference that the staves are shorter since they host two rows made up by only four outer barrel modules. Each outer barrel module consists of two rows of seven ALPIDE sensors. The thickness of the ALPIDE sensors in an outer barrel module is 100 μm whereas the ALPIDE sensors that are used in the inner barrel have thickness 50 μm . Moving to the three inner barrel layers, they consist of 48 staves each one of them constructed by an inner barrel module. The inner barrel modules consist of 9 sensors arranged in one single row, the one after the other. The schematic representation of the ALPIDE topology in the inner and outer modules and staves, is demonstrated in Figure 3.6. Another important characteristic of the ALPIDE is also shown in the latter Figure and it is the possibility to be programmed in order to serve in two different modes, in master-slave logic. An ALPIDE sensor operating as a master is a fully independent sensor that can receive control commands and transmit the data. On the contrary an ALPIDE chip operating as a slave depends on a master chip for the data collection and transmission. The sensors of an inner barrel module are all operating as master chips and are independent, whereas in the outer module case both types of modes are present. Each row of chips begins with a master chip and the rest six are operating as slaves, meaning that the master of the row is responsible for the data collection and transmission of all the chips of the row. The data exchange, is done through a OB Module Local DATA Bus which is interconnecting the parallel DATA ports of the chips. The unique identification of each sensor is also part of the ALPIDE design logic and it is accessible through a 7 bit number, the Chip ID. The [3:0] four bits of the Chip ID provide information about the chip's position on a module and in the outer barrel case about the row (top or bottom) that the chip belongs. The [6:4] three bits of the Chip ID identify the position of the module in the staff that the chip belongs to.

The readout logic is fully implemented inside the ALPIDE eliminating the need of additional active components and electronics in the sensitive area. The control and high speed links of the inner and outer barrel modules and staves are schematically represented in Figure 3.8. In the inner barrel case, each one of the sensors has its own high speed link for data transmission, whereas in the outer barrel case there are 14 high speed links (or 8 for the middle layers) for every half staff. The data rate per link for the inner barrel

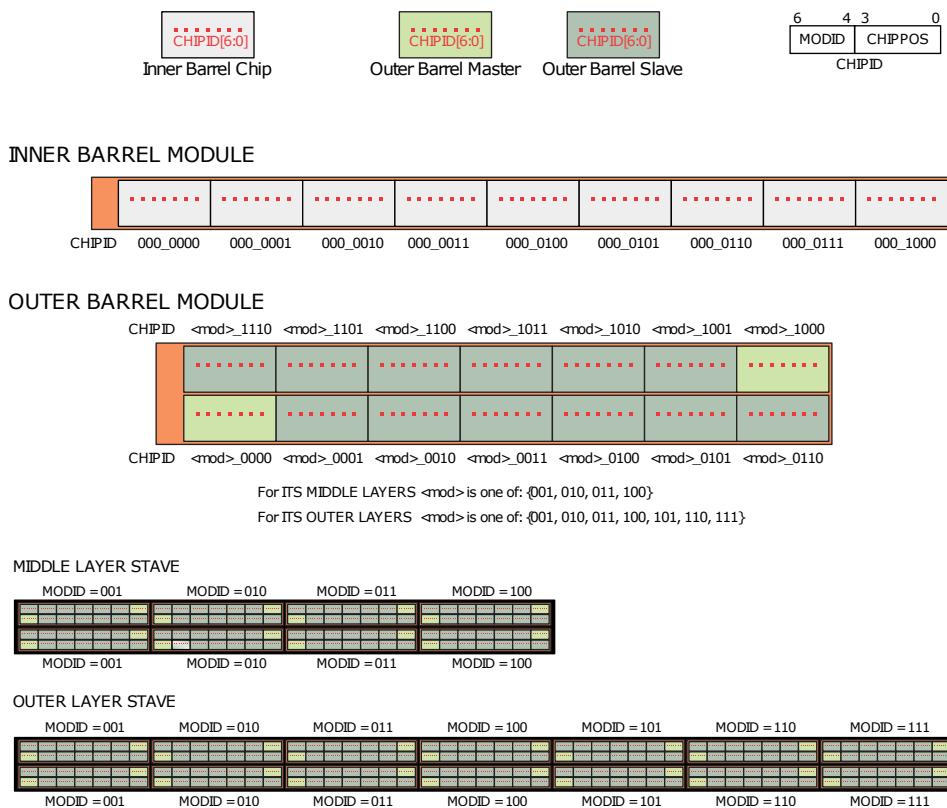


Figure 3.6: *ALPIDE* operating modes and identification topology [53].

is 1.2 Gb/s³ and for the outer barrel 400 Mb/s.

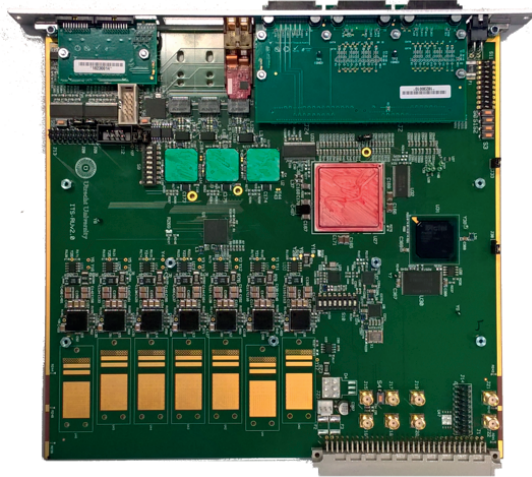
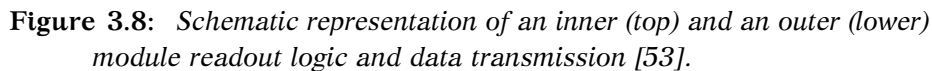


Figure 3.7: *ITS readout unit.*

The data transmission is done through 8 meter twinax cables to 192 readout units that are installed in a medium radiation environment. The readout units are responsible for the control of the power supply and for the transmission of the clock and control signals and the data, to and from the detector [54]. Each readout unit is connected to an entire IB or OB stave. The individual components of the readout unit are shown in Figure 3.7. The main component is a Field-Programmable Gate Array (FPGA) which is responsible for the sensor control and the handling of the data collection and formatting. The readout units are optically connected to the Common Readout Units (CRU) for the data transmission. The connection is done through the Gigabit Transceiver Optical Links (GBT) that are present in the readout units and comply with the radiation level of the environment. The trigger and control information are derived from the Central Trigger Processor (CTP) to which the readout boards are connected.

³The inner barrel links can operate at lower rates of 600 Mb/s or 400 Mb/s.



3.3.1 Production and materials

The beginning of the production of the ITS upgrade is the preparation of the ALPIDE sensors. The ALPIDE production starts with the processing of the CMOS wafers that is done by TowerJazz and it is followed by the thinning and dicing of the wafers, Figure 3.9. The sensors are stored in trays and are delivered to dedicated sites where a pixel chip series test takes place for their electrical characterization.

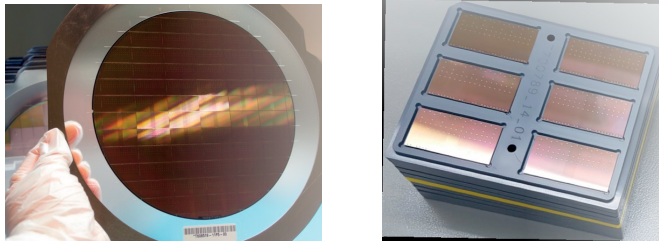


Figure 3.9: *ALPIDE wafer (left) and diced ALPIDE chips (right).*

The ALPIDE sensors are then distributed to OB module production sites and to CERN (IB production) where the module assembly takes place. The modules are constructed, electrically characterized and then sent to the stave production sites. The stave assembly and characterization is the last step before the detector components are delivered to CERN for additional characterization and for the on ground commissioning. Detailed description of the production for the outer and inner barrel is listed in the following section.

Outer Barrel assembly and components

- **Outer Barrel module**

The Outer Barrel module or Hybrid Integrated Circuit (HIC), as it is also named, consists of a Flexible Printed Circuit (FPC), two rows of seven ALPIDE sensors and six aluminium cross cables. The OB FPC, demonstrated in (Figure 3.10), is a two-layer copper printed circuit that is used for the distribution of the power, the clock and control signals and for the data transmission. In the OB case, there are two types of FPC produced, the Type A and the Type B. The Type A FPC is used for modules that are in positions 2-7 on the outer layer half staves,

whereas the Type B FPC is used for OB modules that are in the first position of a half stave. The Type B FPC is slightly longer than the Type A, due to the presence of an additional line of soldering pads for ground connection.

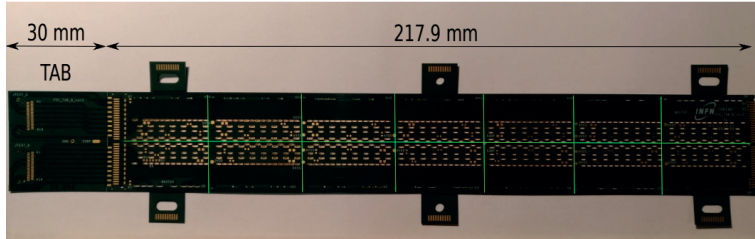


Figure 3.10: *Type B FPC of an outer barrel module.*

The two layers of the copper are separated by a polyimide layer and covered by a solder mask in both sides in order to prevent the corrosion of the metal. The FPC is equipped with vias that are first plated with a nickel layer that is gold plated afterwards.

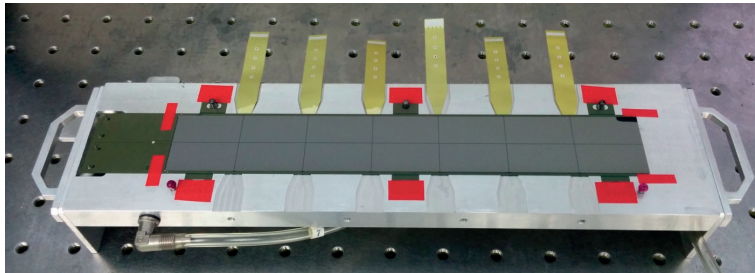


Figure 3.11: *Outer barrel module.*

The sensors are glued to the FPC with high precision. The vias of the FPC, that are connected with the metal layer of the FPC, provide the electrical connection with the sensors. The electrical connection is done with wire bonding that connects the vias of the FPC with the metal pads that are present in the ALPIDE sensor. In the ALPIDE chip the vias for the power supply are distributed over the full surface of the chip while the I/O connections are placed along the one side of the chip. This new feature with respect to other silicon pixel detectors, in which the vias are realized in the edge(s) of the chip, improves the power connection

and the electrical quality [46]. Schematic representation of the FPC layers and of the wirebond geometry are demonstrated in Figure 3.12. The power supply of the FPC is done through the cross cables that are soldered to the power and ground planes of the FPC, Figure 3.11. The readout of an OB module is done through connectors that are soldered in the extension of the FPC, the tab. The tab is present in the design only for testing purposes during the production and it is cut afterwards with dedicated tooling. In the case of modules with Type A FPC the tab is cut in order to allow the interconnection of the modules of a half stave, whereas in the case of modules with Type B FPC the tab is cut to allow the soldering of the first module of the half stave to the FPC extension as it will be later discussed.

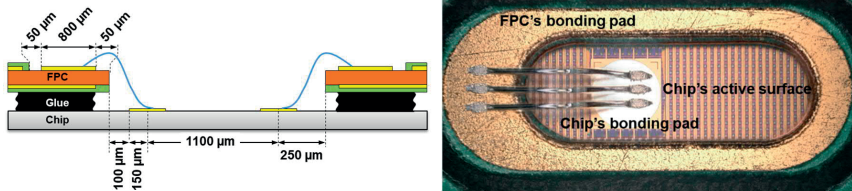


Figure 3.12: *Electrical interconnection of ALPIDE sensors to the FPC [55].*

- **Outer Barrel staves**

The OB staves of the outer and middle layers have the same production process with the only difference being in their length which is adjusted to approximately the length of seven and four modules, 1500 mm and 900 mm respectively. The stave assembly procedure starts with the construction of the individual half staves. Each OB half stave has a carbon-fiber cold plate (CP) for the cooling and for mechanical support purposes. Inside the cold plate, two polyimide cooling pipes are installed that are responsible for the water circulation throughout the length of the half stave. The choice of polyimide as the material was done due to the low material budget and the high radiation hardness that polyimide offers. On top of the cold plate the OB modules are glued after they are aligned with a high precision measurement machine. The aligning tool adjusts the modules on the cold plate by aligning the chip markers

that are present in every ALPIDE sensor. The electrical interconnection of the OB modules is done by soldering the pads of the sub-sequent modules. The first module of the half stave is soldered to the FPC extension which is further connected to dedicated cables for the data readout.

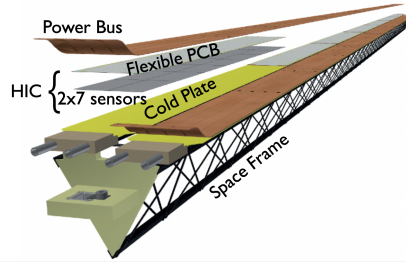


Figure 3.13: *Schematic representation of OB stave layers.*

After assembly and testing, the two half staves are installed in the support structure of the OB stave that is the space frame (SF). The installation of the half staves on the space frame is done with the gluing of each half stave's cold plate on the space frame. An overlap of the two half staves is foreseen in order to eliminate the dead areas in the detector. The space frame is a lightweight mechanical support structure made up out of carbon fibres benefiting from the stiffness that the material offers. The last step of the stave production is the connection of the power bus and the bias bus (for reverse bias voltage supply) with the cross cables. The cross cables of every half stave are soldered to the power and to the bias bus cables which are then folded on top of each half stave. The position of the power and bias bus is secured with means of u-arms that are glued on the half staves.

Inner Barrel assembly and components

The production of the inner barrel from the module to the barrel assembly was completely done at CERN. The inner module production includes the mechanical and electrical interconnection of one row of 9 ALPIDE sensors to the inner barrel FPC. The sensors are aligned to the FPC with a 5 μm accuracy and glued to the FPC after the glue distribution in dots by means of a gluing mask. The sensors are electrically connected to the FPC with wire bonds similarly to the procedure followed for the outer barrel modules.



Figure 3.14: *OB stave of the outer layer.*

However, the inner barrel FPC has major differences with respect to the outer barrel one. The size of the inner barrel FPC is narrower (one row) and the metal material is different. The inner barrel FPC consists of two conducting layers of aluminium with a polyimide substrate in between. The FPC provides 9 differential lines (high speed links) for the data transmission, two differential lines for the clock and slow control signals as well as the analogue, digital, ground and bias voltage supply.

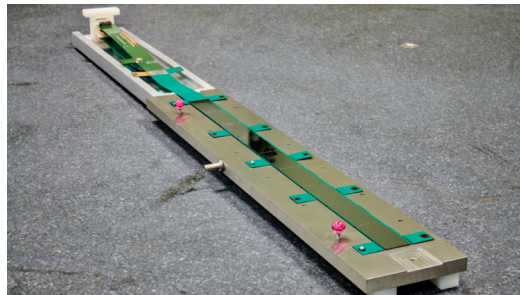


Figure 3.15: *Inner barrel module.*

The inner barrel module is glued on the inner barrel cold plate which is

equipped with the cooling tubes and it is embedded in the space frame. The inner barrel space frame is 290 mm long and has a weight of ~ 1.7 g.

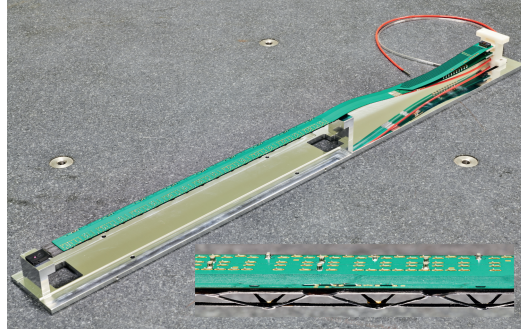


Figure 3.16: *Inner barrel stave.*

Barrel assembly and mechanics

The mechanical design of the support and service structures of the upgraded ITS was done in order to ensure the main prerequisites of the upgrade strategy. The major requirements for the assembly procedure is the accurate installation of the detector to fully exploit the high granularity, to be installed at the closest distance to the interaction point and to benefit from a reduced material budget in the sensitive area. At the same time the cabling for the power and data transmission as well as for the cooling is routed through the service structures of the system which are only in one side of the detector. The barrel design ensures the thermal and mechanical stability throughout the years but at the same time allows the easy insertion and removal of the detector for the scheduled maintenances. The optimal mechanical design, is beneficial not only for the ITS itself but also for the installation of the new MFT and of FIT system.

The two barrels of the upgraded ITS, the inner and the outer barrel, are assembled in half barrels which are then mounted together to form a full barrel, Figure 3.17. Each detector half layer consists of a Cylindrical Structural Shell (CYSS) in the two ends of which the end-wheels are connected. The end-wheels are light composite end-rings that allow the accurate installation of the detector staves. The end-wheels have a different size and geometry in the two extremities, with the one being squared-shaped and the other one

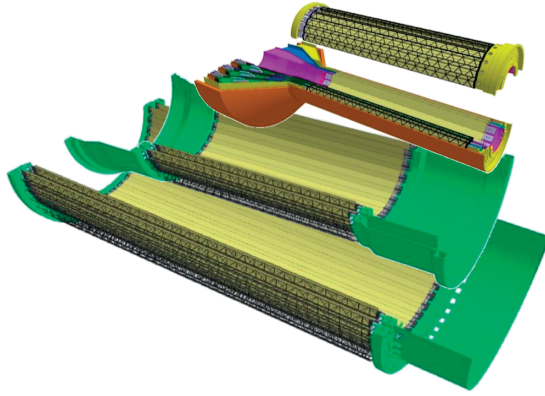


Figure 3.17: *ITS barrels.*

V-shaped to serve as a feed-through for the cabling. In case of the OB, the four layers are grouped in two independent assembly structures which are adjusted together with two Conical Structural Shells (COSS). The CYSS and COSS are light support structures each one made up by two layers of carbon fibres spaced by an Airex core. The IB and OB half layers are demonstrated in Figures 3.18 and 3.19 respectively.

3.4 Detector characterization

During the production phase of the ITS upgrade, the detector construction was accompanied by a wide variety of tests whose aim was the characterization and qualification of the detector components and their quality ranking for the selection of the modules and staves with the highest performance to be installed in the new ITS. In addition to these tests a number of ageing tests were performed for a number of detector modules and staves to verify their functionality and condition in a ten year projection. Detailed description of the tests for the electrical characterization, the ageing and the reliability of the detector is given in the following section together with the most relevant laboratory measurements that indicate the exceptional performance and uniform response of the detector components of the ALICE ITS.

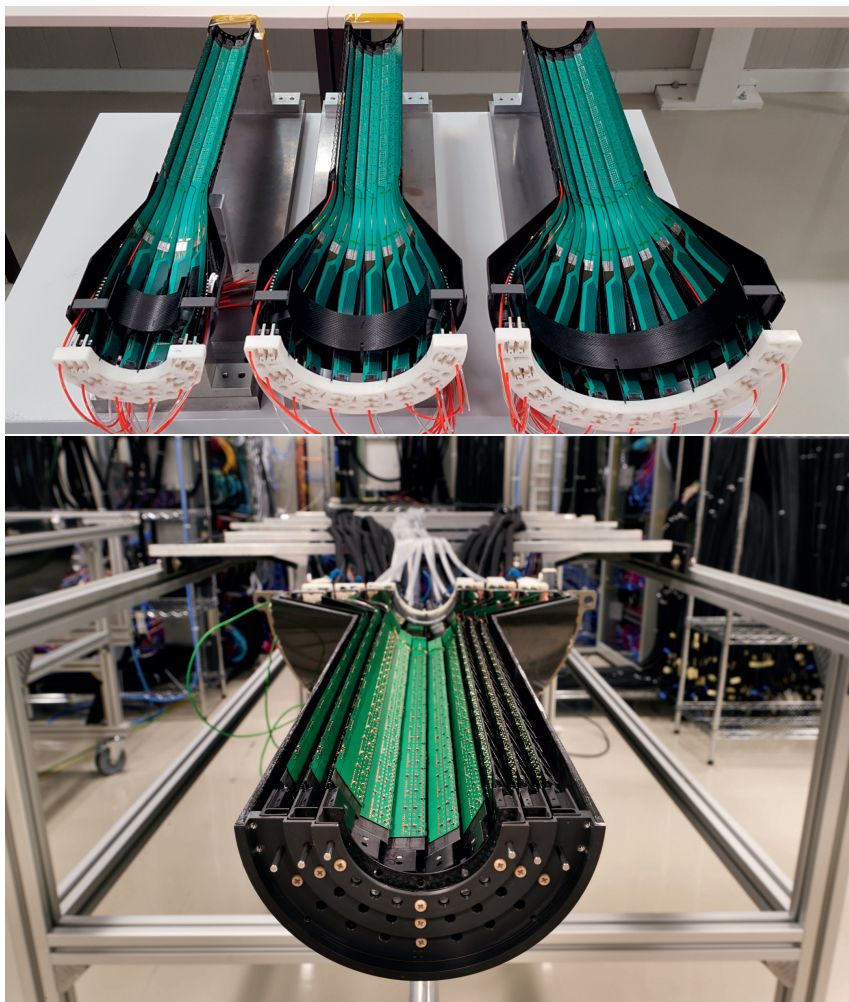


Figure 3.18: *Half layers of the Inner Barrel.*

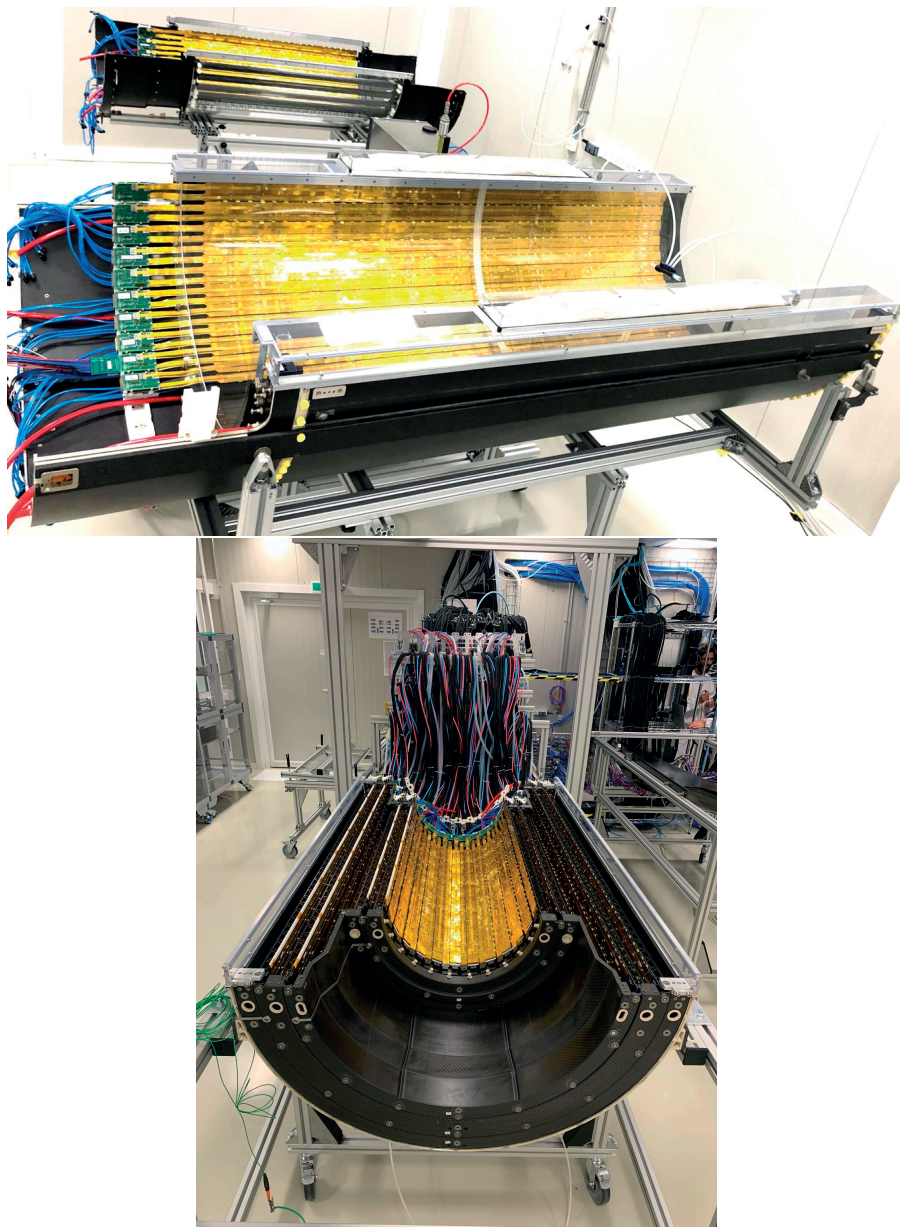


Figure 3.19: *Outer Barrel layers.*

3.4.1 Electrical qualification

The electrical characterization of the detector modules and staves is a crucial part of the production phase. The human and mechanical intervention on the detector components at each production level could result in a physical or electrical damage on them. For this reason a plan was defined with dedicated electrical tests to be executed after every production step. The testing sequence during the production is demonstrated in Figure 3.20.

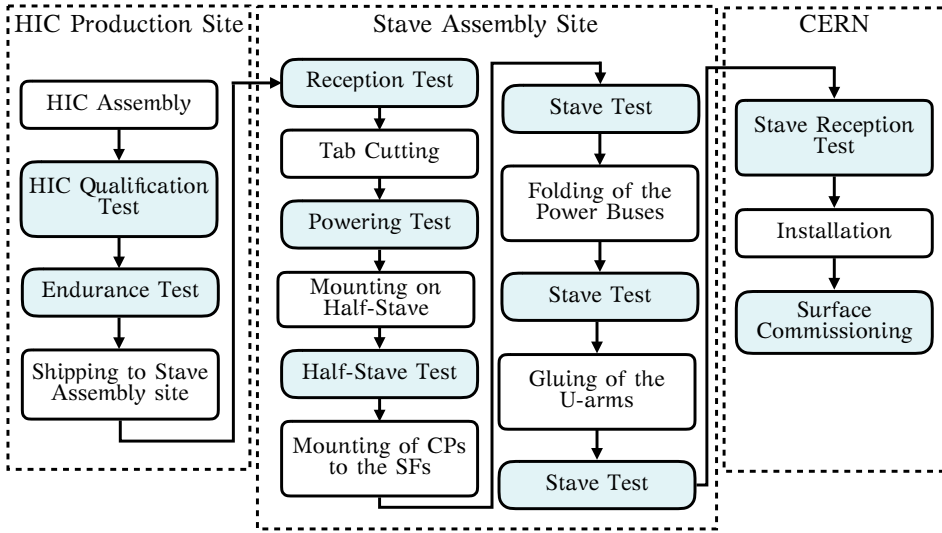


Figure 3.20: Testing overview of the detector components during the production phase.

Upon the assembly of an OB or IB HIC, a HIC qualification test is performed that includes multiple tests regarding the digital and analogue performance of the component. In the OB case the qualification test is followed by an endurance test whose role is to check the electric response of the OB modules after multiple power cycles. The endurance test is performed in parallel for ten OB modules at a time inside a light proof black box. This is the last test the OB modules undergo before they are sent to the stave assembly sites. In the stave assembly sites a reception test is performed on the modules which is required in order to validate that there was no damage during the transportation. The tab is then cut from the modules and a powering test is performed. This is the last test an OB module undergoes

since after it is assembled in a half stave. The half stave test is then performed on the half stave for its qualification and it is followed by multiple stave tests after each step of the stave assembly. The staves are shipped to CERN where a stave reception test is done.

The full electrical characterization is done with a software package that includes the aforementioned tests, which are provided to the users through a user friendly graphical interface. Upon the execution of the test and depending on the outcome, the component under test gets automatically classified and all the result files as well as the classification are stored in a commonly used database. The immediate access to the available components and their results allows the efficient selection of the highest quality components for the installation.

Laboratory equipment

At every production stage and depending on the Device Under Test (DUT), dedicated laboratory equipment is required. In order to test the performance of the DUTs under as realistic conditions as possible the equipment was chosen to be equal or equivalent to the one foreseen in the final experiment. An overview of the setup devices used for the electrical characterization of the modules, the half staves and the staves is listed below.

- **Test box**

In the case of a qualification and of an endurance test the modules are installed in a black lightproof box that provides shielding and ventilation. The box is equipped with specific rails for the installation of the support plate of the module(s) and extra space for the cabling. In the case of the endurance test the box for the OB modules is shown in Figure 3.21.

- **Power & break out boards**

The power boards are used during the production phase of the ITS upgrade for the powering of the modules and (half) staves. In the final detector setup the power boards are connected to the CAEN power supplies and to the staves. Every power board consists of two power units (left and right) with each one of them having a slot in the front side where a breakout board can be mounted, Figure 3.22. The breakout board is an extra component of the power unit that hosts vias for

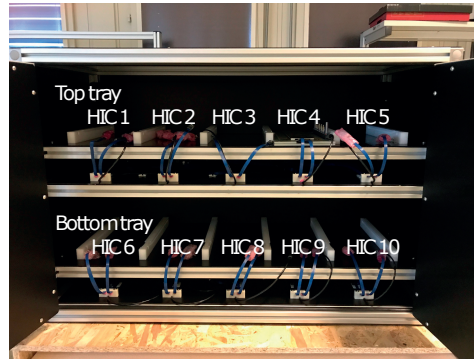


Figure 3.21: *Front view of the endurance box.*

the digital, the analog, the bias and the ground supply voltages. The power cables connect the breakout board with the DUT. In case of an OB module, the breakout board is connected to the OB module power adaptor for a single module test, while in the case of an OB half stave the breakout board is connected to an OB half stave powering bar. For the testing of an entire OB stave, after the final power and bias bus installation to every half stave, the power supply is done through the connection of the power and the bias buses to the power board via dedicated filter boards.



Figure 3.22: *Right power unit of the power board.*

- **OB module power adaptor**

The connection of the power cables starting from the power board to an OB module is done through a spring loaded power adaptor, which offers a reversible power connection without damaging the cross cables. The power cables are connected to the analogue, digital, bias and ground pins of the adaptor. The module powering is done by the contact of the adaptor pins with the module cross cables. The OB module power adaptor is demonstrated in Figure 3.23.

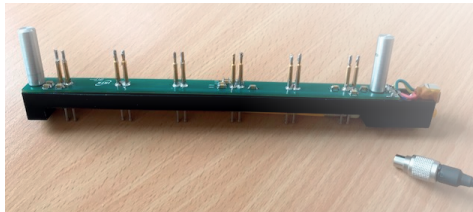


Figure 3.23: *Power adaptor of OB module.*

- **OB half stave powering bar**

In the case of an OB half stave, the OB module power adaptors are mounted on a side support bar. The power supply of the power adaptors is done through a wire model of the power bus that is demonstrated in Figure 3.24.

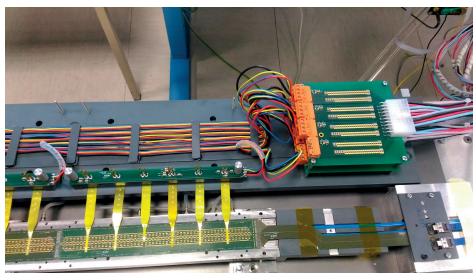


Figure 3.24: *OB half stave powering connection.*

- **MOSAIC board**

The MODular System for Acquisition Interface and Control (MOSAIC) board is a readout board [56] developed for the testing of the ITS

upgrade components, from chip to stave level and it is an essential part of the ITS production test setup.

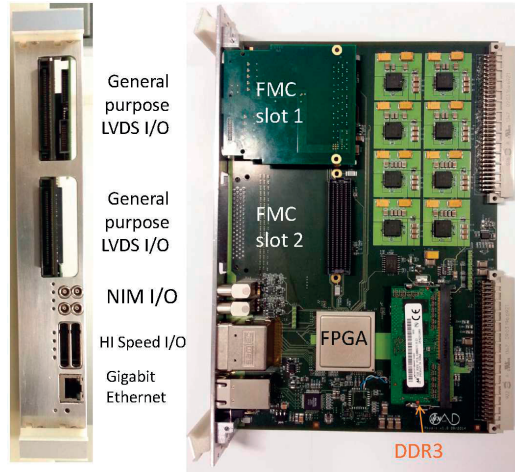


Figure 3.25: *Front view (left) and side view (right) of the MOSAIC board.*

The main component of the MOSAIC is an FPGA that is responsible for the readout. The data transmission from the detector component to the MOSAIC is done through high speed serial links that are read out by the ten receivers that are present in the board. In addition, the board allows the use of slower channels, such as Low Voltage Differential Signals (LVDS) lines. The communication between the MOSAIC and an external computer is done via TCP/IP connection that the MOSAIC offers. A number of LEDs is also present in board to indicate the status of the MOSAIC. Finally four input/output LEMO ports that allow the easy monitoring of important signals such as the trigger and the clock.

- **Power supplies**

Power supplies are required for the powering of the power boards. In the final detector setup the power supply is done with CAEN power supplies.

- **Oscilloscope**

The oscilloscope is required for the DCTRL scan, which is among the scans included in the software that it is discussed later.

Software and Graphical User Interface

For the electrical characterization of the ALPIDE sensors, the modules and the staves, a software framework was developed that is integrated in a Graphical User Interface (GUI). The new-alpide-software package was distributed to the module and staff production centres as the ultimate tool for the characterization and the qualification of the detector components in all production stages. The guidelines for the development of the software framework were to create a program with simple architecture that is organised in blocks, can be easily adjusted to include more tests and have a flexible readout logic that allows the testing of different DUTs, HICs, half staves and staves, and the use of different readout boards.

The communication of the main part of the software with the other devices of the setup, other than the DUTs, is done with libraries. The MOSAIC board is provided with a firmware package and a c++ library that allows the communication with the board. Similarly, the readout unit has its own library in the new-alpide-software directory. Apart from the connectivity with devices the software provides remote access and communication with the database where a read and write interaction is required. The access to the web interface of the database is done through a library which makes use of the functions of the Application Programming Interface (API) of the database. The access to the database is limited to registered users whose access is enabled with a CERN user certificate issued in their CERN account. The user identification for the database communication is done through the Kerberos network authentication protocol which is set up upon then use of the software.

The basic pillars of the new-alpide-software are the abstract classes that are implemented to serve the basic steps of initializing the setup, establishing communication with the readout board(s), configuring the sensors of the DUTs, executing a scan and performing the analysis. The abstract classes are then extended to the derived classes which inherit and use the high level functions. The initialization of the setup is done in two steps. The first one is the decoding of an input configuration file with a class developed for this purpose. The configuration file, that is provided by the user, contains all the specific information regarding the setup, the type of the DUT and readout board and the values of the configurable settings that are used in the tests. The configuration file allows also the deactivation of part of the sensors/modules of the device. The second part of the initialization is the

creation of the basic objects that will be used throughout the test and their configuration. The control of the readout boards is done through an abstract class which is extended to three derived ones each one of them supporting one readout board type, the ALPIDE readout unit, the MOSAIC board and a Data acquisition (DAQ) board. The readout board class is responsible for the establishment of the board and sensor communication, for the storage of unique identifiers for each sensor for direct access and distinguishability as well as for the setting and sending of the trigger commands to the sensors and for the reading of the received event data in an undecoded format. Each one of the readout board classes has its own board configuration class for the configuration of the boards and of the readout. Similar strategy is followed for the power boards which have dedicated classes for the power board initialization and configuration. The latter ones provide control of the power board and of all the voltages and currents. A set of functions is also included for the power board calibration in order to correct from possible voltage drops and be able to exploit the sensors in full performance in their optimal settings.

The basic chip interface and the map of the ALPIDE registers are provided in a specific ALPIDE class which along with two configuration classes are responsible for control of the sensors. The latter ones allow the standard configuration of the sensors, the setting of the sensor parameters and the extraction of the sensor properties. For the module identification and control a specific class was developed and another one for its configuration. Through the basic HIC class, the information regarding the module, the devices it is connected to, the sensors it contains as well as the voltage and current characteristics, can be retrieved. Dedicated functions allow the classification of a module based on the scan outputs and on the comparison with previous results. The HIC configuration class on the other hand is responsible for the global HIC parameter configuration.

After the initialization and the configuration of the setup the user can perform different test types that include one or more scan types depending on the production level and needs. The majority of the test types require the data extraction from the sensors and the data decoding. In the new-alpide-software package the reading of the event data and the data decoding are controlled by different classes. Two classes exist for the data decoding, the board decoder class and the ALPIDE decoder class. A separate data taking class is responsible for combining the functionality of the aforementioned classes, retrieve and decode the data from the sensors.

Each scan type consists of a scan, an analysis and a result object that are created in a scan factory class. The factory class contains the definition of all the different scan types that can be included in the different test types. Starting with the different scan objects, they belong to different scan classes that are derived from a common base scan class. Each scan class contains the scan parameters and the basic functions for the initialization, the execution and the termination of the scan. The scan class is also responsible for the filling of the histograms (only in relevant scan types) which are created from a dedicated histogram class and are further analysed from the analysis class. The configuration of the scan is done by a scan configuration class which includes all the default values of the scan settings. In addition, the scan configuration class contains all the upper and lower cuts upon which each HIC, IB or OB, gets classified. The analysis and the result objects are created by different analysis classes that are inherited from a base analysis class, similarly to the procedure followed for the scan objects. The analysis class is responsible for the execution of the steps of the analysis strategy, for the extraction of the analysis parameters, from the histograms (if applicable), and for the comparison of their values with the predefined cuts for the classification. At the end of each scan the module gets classified for the individual scan. The output files of the analysis are stored locally but at the same time can be attached to the corresponding activity in the database together with the classification and the values of crucial parameters.

The new-alpide-software is nicely integrated in a GUI which is the communication tool between the users, the detector components and the database. The GUI uses all the abstract and derived classes of the software and through their functionality gives full access on the detector but at the same time protects from wrong actions that could result in misleading test outputs or damage on the detector components. The main window of the GUI is demonstrated in Figure 3.26 and it is divided in two panels. The right panel is devoted for the representation of the DUT layout. A schematic representation of an OB/IB module or (half) stave is displayed in the object layout indicating the (non) working chips or modules respectively. The color coded display allows the users to get a quick overview of the quality of the module/ (half) stave and spot basic functional problems. The display colors of the object overview are adjusted in the GUI based on the outcome the initial register readback test, that will be later discussed. Modules that are marked as red have zero working chips, the green ones have all of the chips functional while in case of orange modules, the number of working chips

the OB module contains is larger than 0 and smaller than 14. In the case of an OB (half) stave the user is able to select a module whose chip map will be displayed and investigate further the status. On the left panel of the main window the test type is displayed (here: an OB HIC Qualification Test) along with the list of the scan types it includes and their status during the execution of the test. The user can select from the menu of Actions the desired way of performing a test with or without database connection and in the first case when to write the results to the database once the test is completed. The main window is the basic window of the GUI from which the secondary windows for the initialization of the test, the configuration of the setup, the database communication and the treatment of the results, appear.

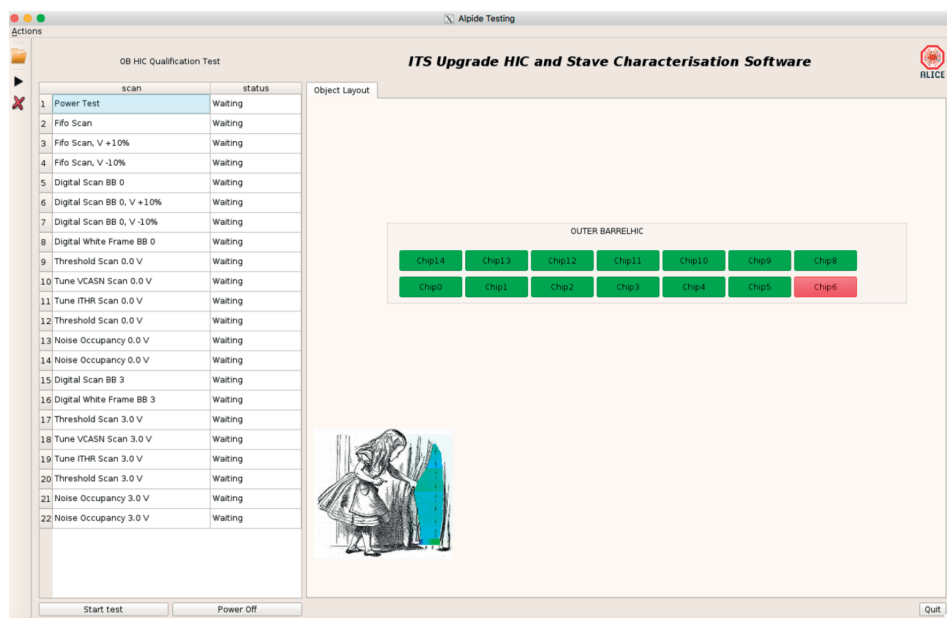


Figure 3.26: Main window of the graphical user interface.

In the beginning of every test the GUI checks if the power board is calibrated and in case it is not a calibration is performed in order to program the correct set value for the desired output voltage, to correct for the voltage drop in the setup and the offset in the current measurement. In case the imminent test will be database connected the user can select the desired database to store the future outcome of the test. The two-database option is there only for dedicated users and concerns a "Test" and a "Production"

database. The official and only option for normal users is the "Production" database, leaving the other option open only for testing and debugging purposes. Every test in the GUI starts with a settings window where the users should complete their credentials and location, choose the test type they want to perform and provide the identifier(s) of the DUT(s). The credentials of the user are required to verify the access of the user in the database system and to link him as the responsible user for the test execution in the database. The GUI verifies that the user and the component id are properly registered in the database and allows the location selection from a list that includes only the locations dedicated to perform the selected test. Additional verification is done on the testing sequence of the component, ensuring that all electrical tests required before the current one were performed and successfully logged in the database. In this way a possibility of bypassing a test during the production is eliminated. In case of a problem in the database communication, of missing information or of an outdated software, a notification window indicates the problem to the user and the test is aborted. Problems at this stage of the test could emerge not only from a non proper supply of information but also from wrongly registered information in the database. Indicatively, a wrong assignment of modules in a stave could be noticed by the GUI at this level. Complementary to the input details the user needs to provide a specific configuration file with the component type and with values of configurable settings. As it was earlier discussed the configuration file is used by the GUI for the initialization of the setup. In the case that all the information are provided properly and the configuration is completed a list with all the scan types that belong to the test is constructed and displayed in the left panel of the main window. The user can start the test any time and will be continuously informed about the execution status of each scan (the individual scans are executed sequentially). When a scan is completed a color coded display will indicate the classification of the scan. The different scans are classified as Gold, Silver, Bronze or Not Working (Red). In the half stave case the color of the scan indicates the classification of the worst classified HIC. In case an exception is thrown due to a problem encountered during the scan or the analysis execution, the user will be notified and will be able to repeat the scan a specific number of times. After all the scans are completed and classified the possibility is provided to the user to have a first overview of the electrical quality of the component. By selecting a specific scan from the list, a menu is populated with the most important scan parameters extracted by the analysis, in particular with those which failed a quality cut, and it

is displayed next to the object layout of the main window. The overall DUT classification is then derived from the worst classified scan of the test. For the final classification of the component, the classifications of the same component from previous tests that are stored in the database are taken into account. With this strategy only the degradation in quality of a component is allowed. However, although the DUT can degrade in quality from previous tests, it will not from the current one in case a repetition of it agrees with previously better classifications. The classification criteria and cuts of the scans as well as of the HICs are provided in the Appendix. Immediately after the completion of the test a dedicated window will allow the user to directly write the results of the test in the database or to postpone it for later. The writing of the results to the database includes attaching result files, saving output values of important parameters and enclosing all the information used for the configuration of the setup and the test. During this process the result files are also transferred to the eos filesystem. In case of problems during the writing to the database the user gets notified and can restart the writing process.

Scan types

The different scan types that build up the different tests of the production are responsible for the electrical characterization and the qualification of the modules and staves. Each one of the scan types contains dedicated parameters the values of which define the quality level of the DUT. Detailed descriptions of the main scan types that are included in the software are presented in this session.

- **Initial Register Readback**

The initial register readback is a generic scan that is performed automatically in the beginning of every test and its role is to define which sensors can be powered on properly and are able to respond. The scan is performed by reading specific blocks of the memory of the sensors, the sensor registers, each of them controlling a different property. The sensors that do not respond in this scan are masked for the remainder of the test. The initial register readback scan indicates problems on the setup and on its configuration such as not properly connected cables as well as internal problems of the modules, like possible shorts or broken capacitors on the FPC.

- **Power test**

The power test is performed in order to validate the proper operation of a module or a stave within the functional limits for the voltage and current. During the power test the module(s) are sequentially powered on, the clock is turned on and the configuration is applied. The parameters of this scan are the digital and analogue currents at the different scan levels, on switch on, with clock and after configuration as well as the bias current at the nominal values of 0 V and 3 V. The current-voltage characteristic curve, the I-V curve, is also obtained for the range of back bias voltage 0-4 V with a current limit at 15 mA and saved in a separate result file. In case the bias current exceeds the set limit the module is classified as back bias not working and the maximum reachable voltage is saved as parameter.

- **FIFO scan**

The FIFO scan is dedicated to study the communication with the sensors through the control interface. The way this is done during the FIFO scan is by a set of read back operations on the region memories of the chip, the FIFO buffers. A FIFO buffer stores data on a first-in, first-out basis and on the ALPIDE case stores the addresses of the hit pixels. The FIFO buffers are located in the periphery of the chip and they can store 16-bit numbers. During the scan four hexadecimal numbers, 0x0000, 0xffff, 0x5555, 0xaaaa, are provided as input to the buffers which are then read out. In the ideal case the output should be identical with the input. In the event of an unsuccessful read back the reason could emerge from an exception or from an error. In the error case a mismatch is observed between the input and the output value which could indicate a problem on a single chip. On the other hand, the exception is thrown when the MOSAIC is not able to read or to decode the data from the chip. The exceptions are indicative of problematic DCTRL links of the master chips or of other setup connected problems, in the readout cables or in the board connectors. All the exceptions and errors per chip and per module are stored in the result output files and classify the module as not working in the event of more than one chips with FIFO errors. The FIFO scan is performed at three supply voltages, at the nominal and at ± 10 %.

- **DCTRL scan**

The DCTRL scan is performed on the components to validate an important part of the ALPIDE, the DCTRL interface. The DCTRL scan is performed on all sensors operating in master mode and thus on all nine sensors of an IB module and on the two master sensors of an OB module that have a control interface. During the scan the signal that is returned from the sensors through the DCTRL lines is measured with an oscilloscope for all the 16 DCTRL driver strength settings from 0 to 15. For each one of them a measurement of the amplitude and of the rise and fall time are done. The rise and fall time is defined as the time it takes to go from 20 % to 80 % of the peak height. The measurements are performed separately for the negative and positive DCTRL lines. During the analysis of the results a fit of the plot of the amplitudes as function of the DCTRL settings (the first point of the measurement is excluded from the analysis) is performed from which the slope, the intercept, the χ^2 and the correlation coefficient are extracted. All the above parameters are documented in the result file together the scan parameters that are individually uploaded to the database. The latter ones are the worst parameter values for each HIC together with the worst χ^2 ratio and the worst slope ratio which are derived from the comparison with previous tests.

- **Digital Scan**

The Digital scan is dedicated to study the digital performance of the modules and staves by checking the pixel response of the digital part across the whole sensor matrix and validate the readout through the high speed data links. During the scan digital signals are injected in the digital logic of every pixel and the number of hits is recorded. The default number of injections is 50, a number that can be adjusted through a configuration setting. The pulsing of the pixels is done in steps, pulsing a pixel row at a time by having in total 512 mask stages.

The problems that can be encountered during the readout are common ones for the remaining scans of this session. Starting with the event data there are two problems that could emerge. The first one is that the event data are not received properly and they are flagged as 8b10b errors, whereas the second one is that the event data are received correctly but they cannot be decoded within the ALPIDE data format. In the latter case the event data are marked as corrupt events. An additional issue that can be phased during the readout are the event

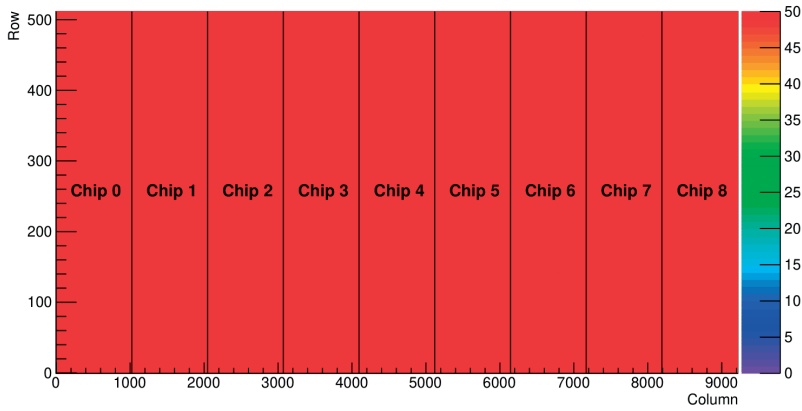


Figure 3.27: *Two dimensional hit map of an inner barrel module after 50 digital injections.*

time outs. Under normal operation when a number of triggers are sent to a sensor, the same number of events is expected to be read out back. In case the same number is not received within a specific amount of time the event creates a time out. After a configurable number of time outs the scan gets aborted. The time outs could be caused by problems in the high speed links, because the triggers are not received by the chips or because some chips might be blocking the readout of the module. The last problem that can occur is the one of the priority encoder errors. In some cases when a pixel is hit its address is sent twice or the pixel addresses of the hit pixels are not sent in the correct order. Both problems caused by the priority encoder can lead to issues on the entire double column that the priority encoder is serving. In most cases this problem is solved by masking the pixels whose addresses are not sent correctly. These pixels are marked as stuck pixels. The stuck pixels together with the bad pixels and all the readout linked problems are saved in the result file. For the classification the number of time outs, the number of corrupt events and the number of bad pixels is used. The latter ones are the sum of the dead, of the noisy and of the inefficient pixels. As dead are marked all the pixels that record zero hits after a given number of injections, whereas as noisy and inefficient are marked the ones that the hits they recorded is different than the

number of injections but not zero. A hit map of a digital scan of an IB module is demonstrated in Figure 3.27. The digital scan is executed at three digital supply voltages, at the nominal and at $\pm 10\%$ while it is also performed for 0 V and 3 V back bias voltage.

- **Digital White Frame**

During the detector operation it is important to be able to mask pixels that are noisy or pixels that are stuck and cannot be read out properly. However, there are cases where some pixels cannot be masked resulting in a problematic behaviour sometimes of the whole sensor. In the event of a stuck pixel, which at the same time is unmaskable, the whole double column that the pixel belongs to is lost. In case these unmaskable stuck pixels are evenly distributed to different double columns of the sensor then the sensor becomes unusable in most of the matrix. The objective of the Digital White Frame scan is to identify the unmaskable pixels of a sensor as well as the ones that are at the same time unmaskable and stuck. The scan is performed by injected charges similarly with the Digital scan with the difference that all pixels are masked. For the DUT classification the number of the unmaskable stuck pixels that belong to different double columns of the sensor is used.

- **Threshold Scan**

The analogue performance of the detector modules and staves is studied with the Threshold scan. Every pixel in ALPIDE has an in-pixel discriminator that has a threshold. When the collected charge from the active area goes through the discriminator its level is compared with the threshold level of the pixel and if it is higher a digital hit is recorded. In the ideal case all pixels of the ALPIDE would have identical threshold values but in reality it is not the case. In order to study the threshold level and the noise of the pixels, during the threshold scan analogue signals of varying charge are injected a configurable number of times (default 50) in the active region of every pixel. The number of hits that are recorded on every pixel are plotted on a real time analysis as function of the injected charge. The resulting plot follows the distribution of an S-Curve, the fit of which is used for the extraction of the threshold scan parameters. In the software there are two ways of fitting the curve. The first one is by using the differential of the S-Curve which is a Gaussian centred on the threshold value and

with a width equal to the pixel noise. The second way of estimating the threshold is by fitting with the error function. The value at which the S-Curve reaches 50% of the maximum is the threshold. For the DUT classification the average noise together with the number of dead pixels and the pixels without threshold per chip are used. The pixels without threshold are the ones for which the fit for the threshold and noise extraction failed. A threshold map of the pixels of an IB module is presented in Figure 3.28 indicating threshold values between 100-170 electrons across the different chips. The threshold scan is performed for two back bias voltages at 0 V and at 3 V. For each one of the voltages the threshold scan is performed twice, once before and once after the threshold tuning (described below). The classification of the DUT is done based on the output of the threshold scan after the tuning.

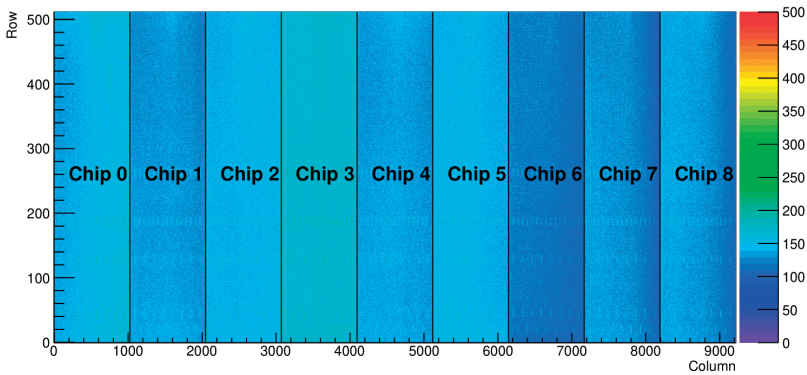


Figure 3.28: *Two dimensional hit map of the threshold level of an inner barrel module.*

- **Threshold Tuning**

The chip to chip threshold variations need to be adjusted in order to achieve a uniform response across the modules and the staves. This is possible with the threshold tuning. There are two types of threshold tuning in the software, the VCASN tuning and the ITHR during. By adjusting the VCASN and ITHR parameters, a uniform threshold level can be achieved between the chips of the same component. As it was previously discussed, by increasing the value of the VCASN the threshold level is reduced whereas by increasing the ITHR the threshold

increases as well. During the threshold tuning analogue pulses of fixed charge, equal to the desired threshold, are sent to the pixels while the values of the VCASN or ITHR are varied. The effect of the threshold tuning is demonstrated in Figure 3.29 where the uniform response of a full OB stave is achieved.

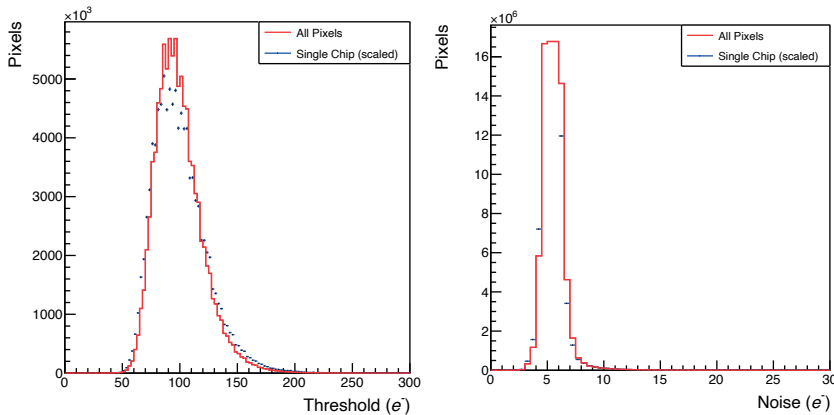


Figure 3.29: *Threshold and noise distribution of the 100 M pixels of an OB stave, after chip by chip threshold tuning. The scaled single chip threshold distribution (blue) agrees with the threshold distribution of all pixels on the stave (red).*

- **Noise Occupancy**

The Noise Occupancy scan is always performed after the threshold tuning when the DUT is at a state where the threshold level is adjusted. The aim of this scan is to identify the noisy pixels and check their occupancy on the detector. The noise occupancy scan is performed by sending 1×10^5 triggers to the pixels without any signal injections. The number of hits recorded on a single pixel divided by the number of triggers gives the pixel noise occupancy. In the chip level the noise occupancy is given by the ratio of hits over the number of triggers times the number of pixels and on a module level as the ratio of the sum of occupancies of all the chips over the number of chips. For the DUT classification, the number of noisy pixels per chip is used. A pixel is marked as noisy in case the noise occupancy value exceeds a configurable value. The noise occupancy scan is performed at two back

bias voltages at 0 V and 3 V and for each one of them twice, without and with masking the noisy pixels.

- **Readout test**

The Readout test is dedicated to study the data transmission at different link speeds (600 Mb/s and 1.2 Gb/s for IB) for standard and low driver and pre-emphasis settings. The common readout problems that were described in the digital scan, namely the number of time outs, the corrupt events and the 8b10b errors are identified and used for the classification.

All the above scan types that are included in the different tests, provide a complete overview of the DUT quality which is reflected on its classification. The electrical response of the DUT is verified and validated at every stage of the signal processing, allowing the users to make interventions on the DUT aiming for an improved detector performance, or to reject or select DUTs for the final detector installation. The new-alpide-software is thus a powerful tool with a leading role in the production phase of the ITS upgrade.

3.4.2 Ageing projection

An important part of the ITS upgrade pre-production phase was the validation of the individual components used to build up the detector modules and staves as well as the verification of the assembly procedure. In view of this direction a number of ageing tests were performed on IB and OB modules and on IB staves. The objective of these tests was to study the endurance of the detector components and how their behaviour will influence the electrical quality of the detectors after a long period of operation inside the ALICE cavern. In order to be able to check the ageing projection of the detector modules and staves in the present time, a number of thermal cycling tests followed by humidity tests at extreme conditions were performed. Starting with the thermal cycles, they induce a thermomechanical stress on the assembly which could have different effects on the different materials. These effects include potential failure of the wirebonds or potential cracks in the glue joints or on the silicon in case the glue is hard enough. The thermal cycles were performed inside a climatic chamber for a specific temperature range. The extreme values of temperature during the thermal cycles were set from 10° to 50° C corresponding to the detector temperature in case of an active

cooling combined with a module failure and in the latter case of a cooling failure while the module is in active mode. With the climatic chamber operating in this temperature range per cycle, an equivalent of 30 thermal cycles correspond to one year of the component inside the ALICE detector. The temperature was monitored through a temperature sensor inside the climatic chamber and the profile of ten thermal cycles is demonstrated in Figure 3.30.

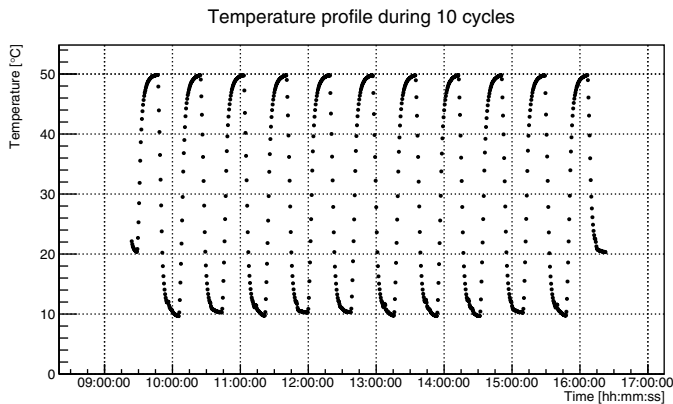


Figure 3.30: *Temperature profile during 10 cycles inside climatic chamber.*

Immediately after one year equivalent of thermal cycles the humidity test which results to accelerated ageing is performed. The humidity test will identify possible corrosion issues on the modules. Indicatively surface corrosion which is unlikely to happen due to the plating, wire-bonding corrosion, or internal corrosion in the FPC. For the simulation of the conditions the nominal values of temperature at 35 ° C and of Relative Humidity (RH) at 35 % were considered. During the test the modules and staves are exposed inside the climatic chamber to an environment with steady temperature at 60° C and steady RH at 60 %. The humidity test has a duration of 13 days corresponding to one year equivalent. After every one year equivalent of ageing the modules and staves are evaluated. The evaluation includes the electrical characterization of the components with a FIFO, a digital and a threshold scan which will immediately indicate possible operational problems. In addition to the electrical characterization, visual inspection is performed under a high magnification microscope to identify possible corrosion or to specify the electrical problem that was discovered during the scans. The

analogue performance of an IB stave before and after three years of ageing is demonstrated in Figure 3.31 indicating a well defined correlation.

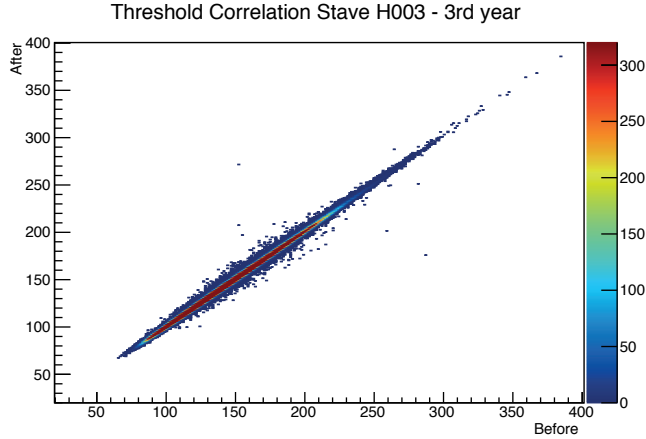


Figure 3.31: *Threshold scan correlation of an IB stave before and after three years of ageing.*

Finally throughout the ageing tests in an effort to validate the wirebond strength and the glue adhesion, pull tests were performed on the wirebonds and peel tests between the sensors and the FPC respectively. The output of the results indicated no degradation of the assembly structure and in combination with the results from the visual inspection and the electrical characterization an excellent component quality and performance throughout the lifetime of the detector inside ALICE is foreseen.

Beauty measurements with the ITS upgrades

4.1 ITS upgrade performance

As it was discussed in a previous chapter the upgrade of the ALICE ITS during the LS2 is going to improve the impact parameter resolution and the tracking efficiency of low momentum particles. The physics program of the ALICE experiment during the next decade requires further improvements that will enhance the measurements of charm and beauty as well as of low mass dielectrons. In the scope of this direction a next upgrade of the Inner Tracking System of ALICE is planned during the LS3 in 2024-2026.

During the ITS3 upgrade the three innermost layers of the ITS2 will be replaced by three cylindrical layers of silicon-only large scale sensors. The new innovations that are becoming available on the silicon imaging technology allow the construction of large scale silicon sensors through the process of stitching. The stitching technology, allows the maximization of the sensor size to dimensions close to the wafer size. The research and development proposal of the ITS3 upgrade aims to benefit from this feature and produce wafers with a diameter of 300 mm from which sensors with size $280 \text{ mm} \times 15 \text{ mm}$ will be produced as it is demonstrated in Figure 4.1. These wafers can be thinned down to $20\text{-}40 \text{ }\mu\text{m}$, a thickness at which the flexible nature of silicon allows the bending of the sensor. For the sensor production, the 65 nm CMOS Towejazz process is proposed which due to the smaller transistor size will result in a reduced pixel pitch, minimizing the

charge collection time and improving the position resolution.

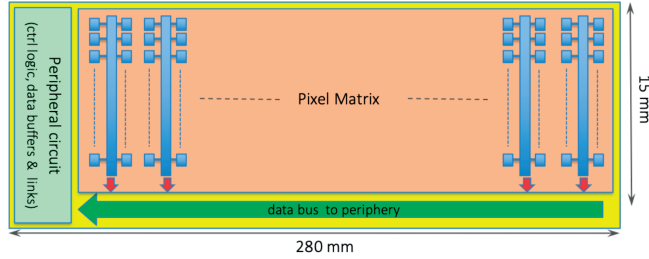


Figure 4.1: Diagram of a stitched sensor in one direction with the periphery positioned in the edge of the sensor. [57]

Each layer will consist of 2 silicon sensors, whose periphery and interface pads will lie on the edge of the chip, outside the fiducial volume. This will allow the removal of the flexible printed circuits and the support structures that were present in ITS2. The latter ones will be replaced by patches of low density carbon foam. In terms of cooling it has been studied that in case the sensor power density is below $20 \text{ mW} \cdot \text{cm}^{-2}$ it is sufficiently possible to replace the water cooling in the active silicon area by low-speed air flow.

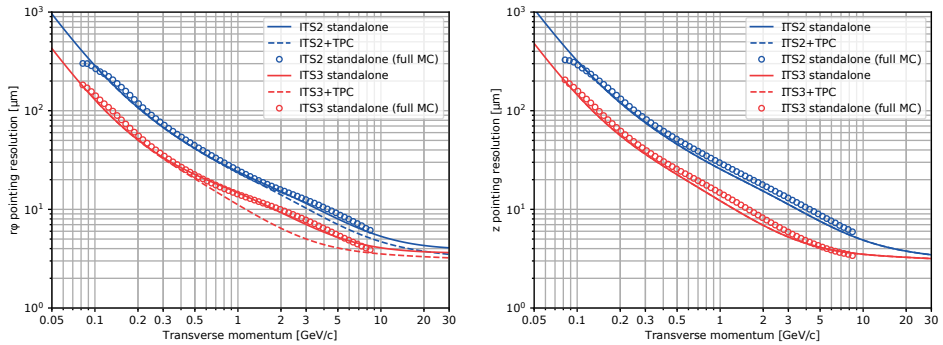


Figure 4.2: Pointing resolution in the $r\phi$ and z plane of primary charged pions with the ITS2 (blue) and the ITS3 (red). The dashed lines correspond to ITS+TPC results whereas the solid lines to ITS standalone performance both obtained with the fast MC simulation tool. The circles demonstrate the performance obtained with the full MC simulation for standalone ITS. [24]

The above modifications will reduce the material budget of the ITS inner barrel from 0.35% X_0 down to 0.05 % X_0 . The thickness of the beam pipe is going to be reduced from 800 μm to 500 μm as well as its inner radius will go down to 16 mm. This will allow the reduction of the radial distance of the innermost layer to the interaction point from 23 mm to 18 mm. The outcome of the above modifications is presented in Figure 4.2, where the improvement of the $r\phi$ and z resolution is demonstrated and compared to the corresponding resolutions obtained with the ITS2 upgrade. The impact of these improvements on the beauty sector of heavy flavour is reflected in the measurement of Λ_b particle, the investigation of which with the ITS2/3 upgrades is the research topic of this chapter.

4.2 Λ_b measurements with ITS2 and ITS3 upgrades

The Λ_b particle is a neutral charged baryon which contains the u d b quarks and according to the latest update has a rest mass of $5619.60 \pm 0.17 \text{ MeV}/c^2$. The measurement of the Λ_b decaying in the hadronic channel of a Λ_c^+ and a π^- with Λ_c^+ further decaying to a p K^- π^+ is one of the measurements that will be enhanced with the ITS3 upgrade. The improved pointing resolution of the ITS3, in the low momentum region, is a key issue that contributes to the investigation of a challenging decay mode with small branching ratio, Table 4.1, and with a four prong final state inside a high background environment. The improvement on the Λ_b measurement benefits also from the expected improvement on the measurement of the non-prompt Λ_c^+ . The mean proper decay lengths of the Λ_b and the Λ_c^+ are 441 μm and 60.7 μm respectively. The significance of measuring the Λ_b particle as well as the measurement of the signal over background ratio were calculated with a MC simulation for both the ITS2 and the ITS3 upgrades and are presented in the following sessions.

Decay channels	Branching Ratio (BR)	p (MeV/c)
$\Lambda_b \rightarrow \Lambda_c^+ + \pi^-$	$(4.9 \pm 0.4) \times 10^{-3}$	2342
$\Lambda_c^+ \rightarrow p + K^- + \pi^+$	$(6.28 \pm 0.32)\%$	823

Table 4.1: Characteristics of the decay channels of Λ_b and Λ_c^+ [30].

4.2.1 Λ_b reconstruction

The algorithm that is used for the reconstruction of Λ_b starts with the reconstruction of the Λ_c^+ decaying to a proton, a kaon and a pion. Three tracks are combined as a Λ_c^+ candidate which passes a selection of filtering cuts on the kinematic variables that will distinguish it from other three prong decays. However, further selection is required in order to reject the large amount of combinatorial background. For this reason, during the filtering the information from the TPC and the TOF detectors are used for the particle identification. In addition, only the candidates with mass inside $\pm 3\sigma$ of the invariant Λ_c^+ mass are selected.

For the secondary vertex reconstruction an opposite sign track, a π^- candidate, is selected and it is later combined with the reconstructed Λ_c^+ . The pion track passes the particle identification selection from the TPC and TOF information. The kinematic information of the Λ_c^+ and the π^- are extracted and used to reconstruct the Λ_b candidate in a two prong decay. A further selection on the kinematic variables of the resulting Λ_b and its daughters is performed for further background rejection. In addition to the latter selection, a loose selection ($1 \text{ GeV}/c^2 \gg 3\sigma \sim 0.07 \text{ GeV}/c^2$ of the reconstructed mass peak) is done on the invariant mass of the Λ_b candidate with respect to the true Λ_b mass.

The aforementioned strategy is followed for the signal selection, in contrast to the background for which further selection is required in order to keep only the background introduced by the HIJING [58] generator and reject injected signal from other particle decays that were forced in the MC sample. The last step of the selection is the background multiplication that is done with the multiple rotational method and will be discussed in the next session. The signal and background distributions of the Λ_b , the Λ_c^+ and the π^- topological variables are stored for the analysis.

4.2.2 Monte Carlo sample

The Monte Carlo sample that is used in the analysis is a GEANT [59] full simulation of the ITS2 geometry and materials with particle transportation, tracking and vertex reconstruction. Approximately 10^6 Pb–Pb events were simulated at $\sqrt{s_{NN}} = 5.5 \text{ TeV}$ using the HIJING generator. In every event heavy flavour and hyper nuclei signals were injected with a cocktail of parametric generators, as well as heavy quark pairs using PYTHIA [60]. The specific MC production was evaluated and used for the physics studies of

many heavy flavour species for the Technical Design Report (TDR) of the ALICE ITS Upgrade [46].

For the study of the significance and the signal over background ratio, an additional selection on the Λ_b particle is done by using topological cuts on the variable distributions for signal and background that were stored for the analysis. However, it has been observed that after the additional cuts are applied, the background under the 3σ region of the signal is totally removed and thus cannot be used for the significance and signal over background calculation. In order to be able to apply the aforementioned selection in an optimized way, a larger amount of background statistics is required. In order to increase the combinatorial background statistics a multiple rotational method was introduced. The multiple rotation technique is a method used to simulate the realistic background by rotating the track of one of the two daughter tracks of the mother particle in the X-Y plane, around the Z-axis which is parallel to the beam axis. The track rotation breaks the correlation between the tracks and it is resulting into pure combinatorial background.

For the current analysis the pion track was rotated. The choice of the number of rotations is momentum depended since the background varies in the different momentum regions. In higher momentum regions the reconstruction algorithm is more powerful, resulting into a lower amount of background statistics with respect to the low momentum regions. For low momentum, so below 9 GeV/c the number of rotations is 13, whereas for the higher momentum regions the number of rotations is increased to 20, increasing the combinatorial background by a factor of 13 and 20 respectively. The generated background introduced by the multiple rotational method reproduces the shape of the original background and thus the rotational method is used for the background multiplication [46].

The analysis of the Λ_b regarding the ITS2 upgrade is performed on the Analysis Data Objects (AOD) of the MC sample. In ALICE there are two types of file typologies, the Event Summary Data (ESD) and the Analysis Data Objects (AOD). The ESDs are the files where all the information extracted from the track finding and reconstruction algorithm of ALICE are stored [61]. The ESD files are further compressed to the AOD files which are the actual files on which the analysis is performed. The AOD files contain the variable information of the tracks, the kinematic characteristics and the detector information.

For the analysis with ITS3 upgrade the same MC sample was used. In order to simulate the ITS3 performance a hybrid method was applied. The

hybrid method is a technique that updates the track parameters that are stored in the AODs. The ITS2 and ITS3 momentum, $r\phi$ and z pointing resolutions are used for recalculation of the track parameters. For the recomputation of every track parameter the scaling factor of the ITS3/ITS2 ratio of resolutions is used [46]. The Λ_b reconstruction algorithm is applied on the updated values resulting to an output file from the ITS3 expected performance.

4.2.3 Selection of Λ_b with topological cuts

In order to distinguish a four prong final state particle from the large combinatorial background, a tight cut topological selection approach is followed on the output files of ITS2 and ITS3. The topological variable distributions of the Λ_b and the Λ_c^+ and the π^- were studied in order to extract the optimal selection cuts that will reject large percent of the background and at the same time keep significant amount of the signal.

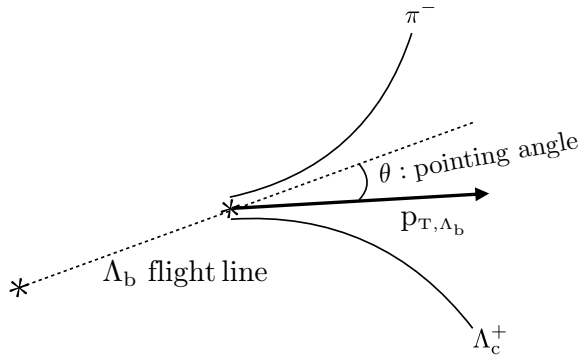


Figure 4.3: Schematic representation of the topology of Λ_b decay.

The variables of which the signal and background distributions were used for the cut optimization are described below:

- **Transverse momentum p_T**

- **Cosp**

Cosine of pointing angle. The pointing angle is the angle formed by the momentum vector and the flight line of the particle.

- **Ct**

The Ct is defined as the decay time times c.

- **Impact Parameter**

The impact parameter is defined as the minimum distance of the particles' track to the primary vertex.

- **Normalized decay length**

The distance between the primary vertex and the secondary vertex is defined as the decay length of the particle. The normalized decay length is defined as the decay length over the decay length uncertainty.

- **Dca**

Distance of closest approach of the daughter tracks.

- **σ vertex**

The track dispersion around the vertex starting from tracks.

The analysis is performed in four different p_T regions, namely 3-6 GeV/c, 6-9 GeV/c, 9-12 GeV/c and 12-15 GeV/c for both the ITS2 and ITS3 upgrades. For each one of the p_T intervals an optimal cut is chosen for every variable based on the signal and background distributions. The cut selection for the 3-6 p_T region is demonstrated in the below distributions for both ITS2 and ITS3.

Starting with the signal and background distributions of the σ vertex of Λ_c^+ , the improved ITS3 resolution is reflected in the signal distribution which becomes narrower allowing the rejection of more background with a tighter cut. At the same time, the Λ_b reconstruction algorithm rejects more background resulting to a lower level in the region of interest. The distributions of the dca of Λ_b indicate the similar behaviour. In the ITS3 case, the improved resolution allows for the tightening of the cut with respect to the ITS2 case. The cuts are also tighter for the case of the cosp of Λ_b and the dca of Λ_c^+ .

The signal and background distributions of the impact parameters of the Λ_c^+ and the π^- allow the rejection of a region where the signal level is low

and the background reaches high values as it is shown in Figure 4.8 and Figure 4.9. The significant improvement on the impact parameter of the Λ_b in the ITS3 case allows for tighter cuts in this variable as well. The cuts applied on the normalised decay length of Λ_b , on the p_T of the π^- , and on the Ct are very similar for the ITS2 and ITS3 cases, they set a lower limit while they are rejecting the high peak backgrounds.

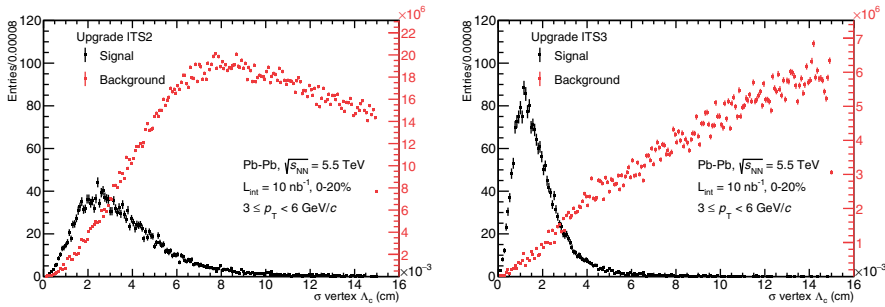


Figure 4.4: Signal and background distributions of the σ vertex Λ_c^+ with the ITS2 (left) and with the ITS3 (right).

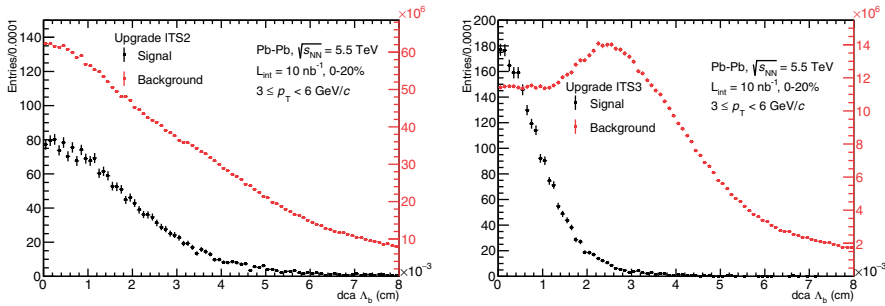


Figure 4.5: Signal and background distributions of the dca Λ_b with the ITS2 (left) and with the ITS3 (right).

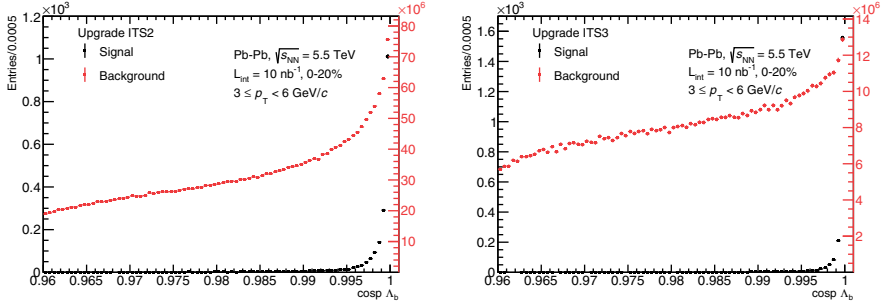


Figure 4.6: Signal and background distributions of the $\cos\theta_{\Lambda_b}$ with the ITS2 (left) and with the ITS3 (right).

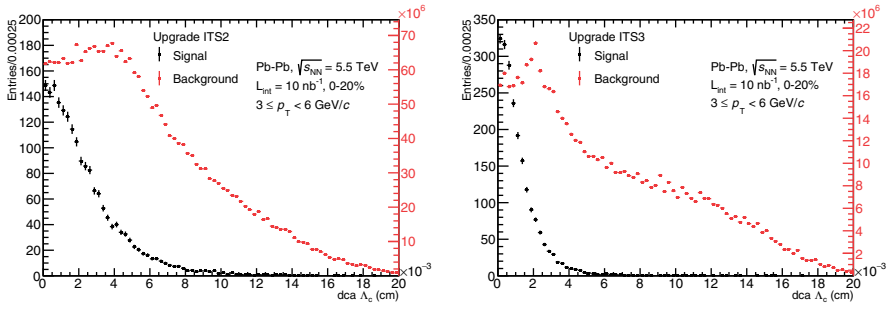


Figure 4.7: Signal and background distributions of the $dca_{\Lambda_c^+}$ with the ITS2 (left) and with the ITS3 (right).

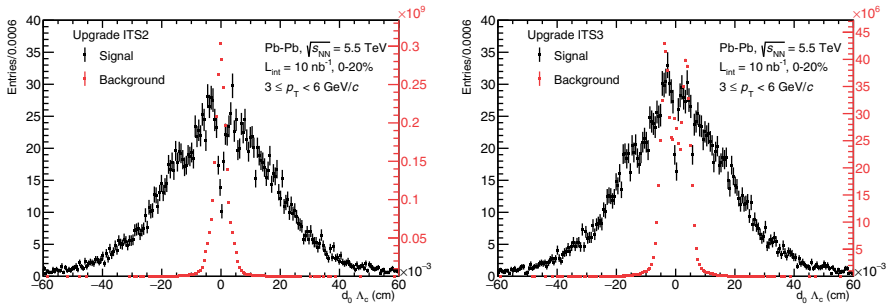


Figure 4.8: Signal and background distributions of the impact parameter of Λ_c^+ with the ITS2 (left) and with the ITS3 (right).

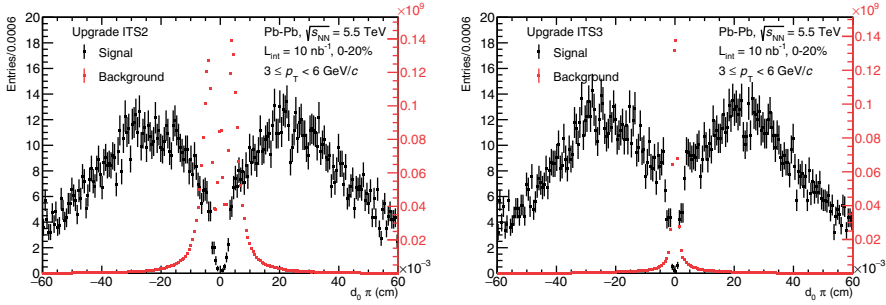


Figure 4.9: Signal and background distributions of the impact parameter of π^- with the ITS2 (left) and with the ITS3 (right).

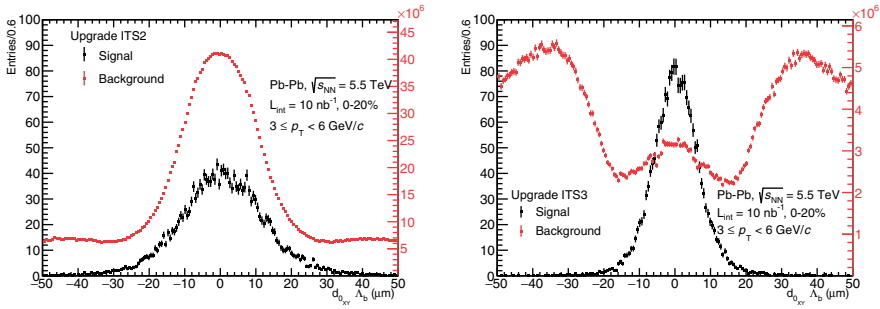


Figure 4.10: Signal and background distributions of the impact parameter of Λ_b with the ITS2 (left) and with the ITS3 (right).

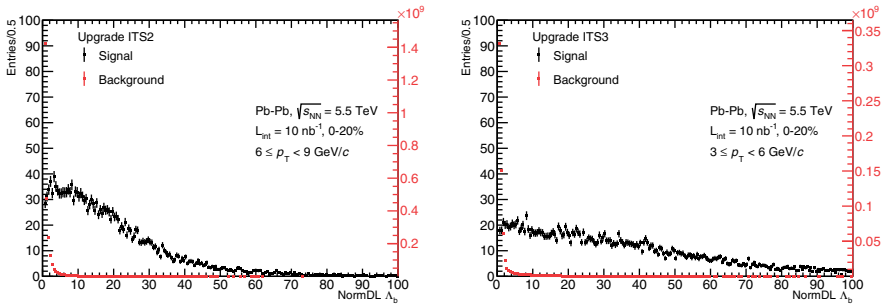


Figure 4.11: Signal and background distributions of the normalised decay length of Λ_b with the ITS2 (left) and with the ITS3 (right).

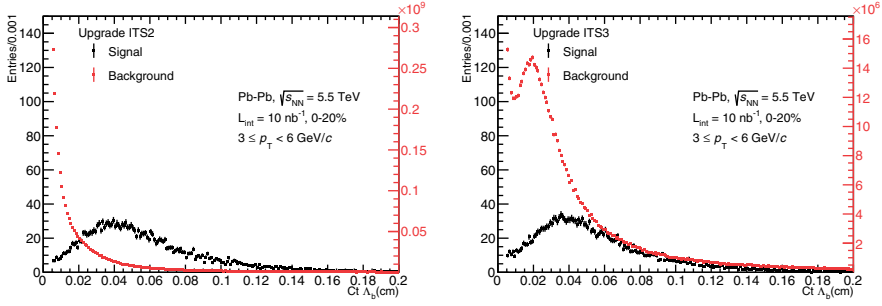


Figure 4.12: Signal and background distributions of the $ct \Lambda_b$ with the ITS2 (left) and with the ITS3 (right).

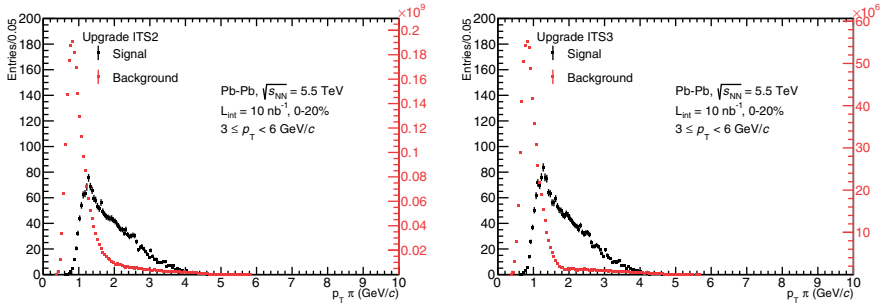


Figure 4.13: Signal and background distributions of the p_T of π^- with the ITS2 (left) and with the ITS3 (right).

The topological variables of the higher momentum regions were similarly studied and lead to the cut selection that is presented in Table 4.2. As it has already been discussed, in the higher momentum regions the background level is significantly lower with respect to the lower momentum. For this reason, in high p_T cuts were not applied in all the kinematic variables, but only on a fraction of them on which for the same reason the selection was chosen to be looser.

Cut variable (ITS2/ITS3)	Λ_b p_T range (GeV/c)			
	3-6	6-9	9-12	12-15
$p_T \pi^-$ (GeV/c)	1/0.8	0.6/0.5	-	-
Cosp Λ_b	0.994/0.997	0.996/0.998	0.998/0.998	0.998/0.998
$ \text{d}_0 \Lambda_c^+$ (μm)	30/10	28/20	25/20	25/10
$ \text{d}_0 \pi^-$ (μm)	50/30	50/50	50/50	40/22
Ct Λ_b (μm)	220/200	190/120	-	-
Impact Parameter XY	18/15	21/15	18/15	16/13
Λ_b (μm)				
Normalized decay length	3.5/3.5	4/4	-	-
XY Λ_b				
dca Λ_b (μm)	30/17	40/20	30/20	25/20
dca Λ_c^+ (μm)	65/45	70/45	50/45	40/30
σ vertex Λ_c^+ (μm)	70/50	60/60	60/50	40/35

Table 4.2: Selection criteria on the variable distributions of Λ_b , Λ_c^+ and π^- .

4.2.4 Analysis results

The estimation of the signal and the background after the cut optimization, is used for the calculation of the significance of the Λ_b with the ITS2 and the ITS3. The S/B ratio is also calculated and compared for both upgrades.

The signal estimation is done by calculating the integral under the 3σ region of the signal peak which is fitted with a Gaussian function. The signal distribution of the Λ_b in the p_T region 3-6 GeV/c in the ITS2 case is demonstrated in Figure 4.14.

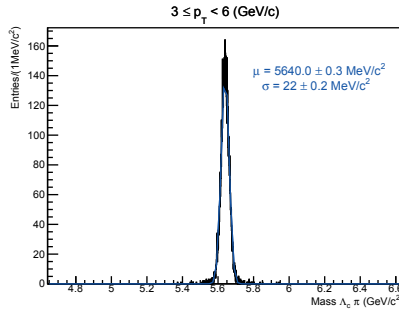


Figure 4.14: Signal distribution of Λ_b in the p_T region 3-6 GeV/c with the ITS2 upgrade.

Since the MC sample that is used contains injected signal, a scaling of the measured signal is required to the true one. The scaling is done by multiplying the signal extracted from the fit with a scaling factor which takes into account the Λ_b expected production yield, similarly as it was done for the Λ_b TDR study [46]. Finally, the signal is divided by the number of events, in order to calculate the true signal per event.

Regarding the background, based on the shape of the distribution an exponential fit is performed, from which the background value is extracted by calculating the integral under the 3σ region of the signal. The background distribution in the p_T region 3-6 GeV/c after the cuts are applied is demonstrated in Figure 4.15. The exponential function is used also for the other p_T regions to fit the background after the topological cuts are applied. The measured background is scaled by a factor $1/N$, where N is the number of rotations, and divided by the number of events to get the true background per event.

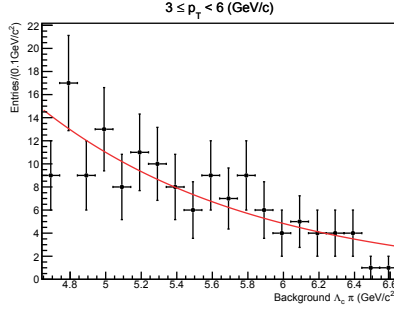


Figure 4.15: Background distribution of Λ_b in the p_T region 3-6 GeV/c with the ITS2 after the topological selection.

The significance of measuring the Λ_b is calculated for the four p_T regions mentioned above for both the ITS2 and ITS3 upgrades and demonstrated in Figure 4.16. For the error calculation a conservative approach is followed, considering a systematic uncertainty of 40% on the background associated with the rotational method, similarly to strategy followed in the previous heavy flavour studies presented in [46] which also used the method. The errors on the significance and on the S/B include the statistical error and the systematic error on the background. The formula used for the significance calculation is the following:

$$Significance = \frac{S}{\sqrt{S + B}} \times \sqrt{M} \quad (4.1)$$

where:

S: the scaled signal per event

B: the scaled background per event

$M = 1.6 \times 10^{10}$: the scaling factor corresponding to the expected yield for 0-20% central Pb-Pb collisions at luminosity $L = 10 \text{ nb}^{-1}$.

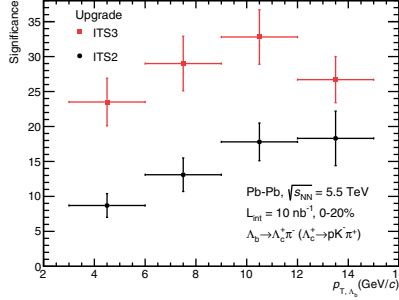


Figure 4.16: Significance of the Λ_b measurement with the ITS3 (red) and the ITS2 (black) upgrades.

The improved performance of the detector with the ITS3 is reflected on the significance of the Λ_b measurement in comparison with the measurement with the ITS2. The improvement is higher in the low momentum regions, almost a factor of 3 at p_T 3-6 GeV/c. The same behaviour is demonstrated in Figure 4.17 where the S/B ratio is improved by a factor of ~ 7 in the lowest p_T region. Both plots of significance and of S/B indicate a sizeable improvement in a wide momentum range which would be interesting to be extended in the p_T region below 3 GeV/c, a momentum region that it was not accessible in the MC sample due to filtering cuts applied on the AOD files. Additionally, a future MC production with increased statistics would allow better measurements in the high p_T regions and lead to the reduction of the uncertainties.

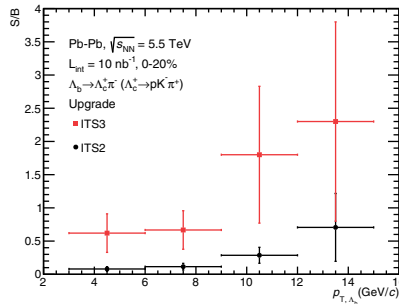


Figure 4.17: Signal over background of the Λ_b with the ITS3 (red) and the ITS2 (black) upgrades.

Discussion

DURING the 2020s, the ALICE experiment is in a new decade of discoveries that will contribute to the understanding of the universe and of the mechanisms that lead to its evolution. Through relativistic heavy ion collisions ALICE will continue reproducing the beginning of the cosmos and studying it while it is cooling down and expanding, Figure 5.1.

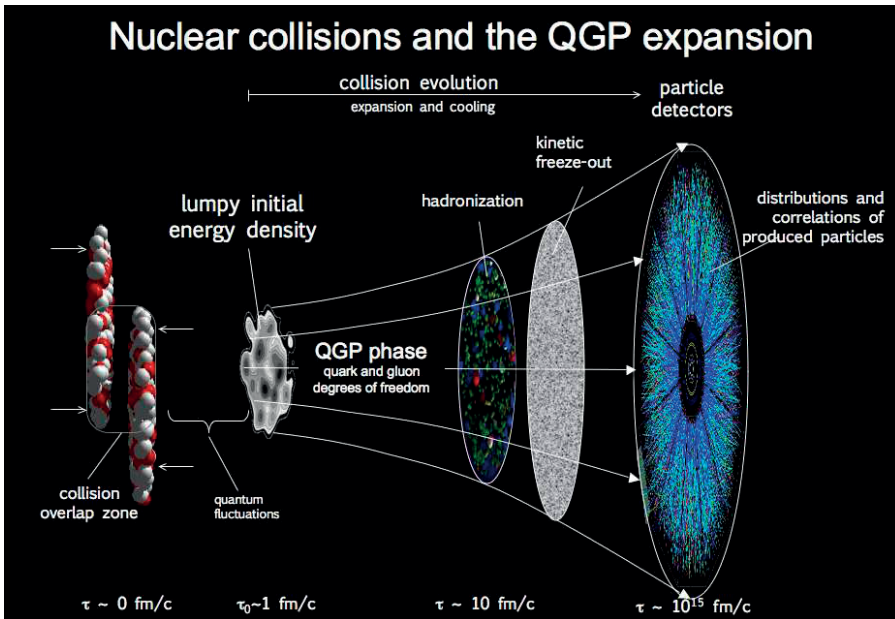


Figure 5.1: *Evolution of heavy ion collisions [62].*

The ALICE apparatus equipped with the latest detector technologies will be able to exploit with high precision the increased luminosity that the LHC will offer during Run 3 and access a wide range of measurements in the heavy flavour sector. The first part of the thesis, that is dedicated to the research and development studies for the ITS2 upgrade, demonstrates the qualification and selection strategy based on which the highest quality detector material was selected and installed in the ITS2. The electrical characterization of the detector modules and staves is covered by a wide range of tests that allow the validation of the analogue and digital performance of the ALPIDE sensors as well as the transmission of the slow control signals and the data. It has been demonstrated that a uniform detector response can be achieved throughout the chips of the modules and staves, at levels where the detection efficiency and the fake hit rate meet the ITS requirements [49]. The classification of the modules and (half) staves that is derived from the tests together with all the information and the settings used during the tests are documented in the ITS database and used for the selection. The module and staff characterisation package, developed in the context of this thesis, was the official tool used for qualification and characterisation of the more than 3000 produced modules and all assembled staves. The author's contribution to the module and staff characterization package includes the development of the graphical interface and its integration in the software framework, while having an active role to the packages' overall development. Specifically, the author as one of the two main developers of test software, contributed to the extensibility of the software in order to allow the use of different readout boards, the testing of different detector components with different types of scans, but also the interaction with the ITS database. In addition, the author contributed to the testing and the validation of the software package with different setup configurations and provided assistance and guidance on its utilization.

Complementary to the software development, the author performed a series of ageing tests, during the ITS2 pre-production phase for the validation of the detector components and the assembly procedure. The effect of the thermal cycling and the humidity test, that were performed on a number of modules and IB staves, was studied with electrical tests, with visual inspection as well as with pull and peel tests. The results indicated the appropriateness of the detector materials and ensured the proper operation of the detector modules and staves in the ALICE cavern within a long term operation.

The ITS production phase was successfully completed and followed by the IB and OB layer assembly and testing. A display of cosmic rays traversing

the innermost IB layer is shown in Figure 5.2. The on-surface commissioning of the ITS2 has also been completed and the installation in the ALICE cavern is taking place during 2021.

The second part of the thesis is dedicated to physics studies based on the ITS performance during Run 4, after a further ITS upgrade, the ITS3. The demand of accessing the low momentum region of heavy flavour hadrons for the investigation of the heavy quark thermalization and hadronization processes, lead to the proposal of a novel ultra light detector which is planned to replace the inner barrel of the ITS2. The effect of the improved pointing resolution, that the ITS3 will offer, was studied in the beauty sector of heavy flavour and more precisely on the measurement of the Λ_b baryon. Based on a MC simulation the significance and the S/B ratio of measuring the Λ_b particle were calculated and compared to the values expected with the ITS2 upgrade. In the low momentum region around 4 GeV/c a noticeable improvement by a factor of almost three and seven on the significance and on the S/B respectively, is reported. The results from the significance and the S/B reflect the substantially improved performance of the ALICE tracker with the ITS3 upgrade. The Λ_b studies with the ITS2/3 upgrades were among the physics material that was presented to the 139th meeting of the LHCC and lead to endorsement of the detector research and development studies for the ITS3 upgrade [63].

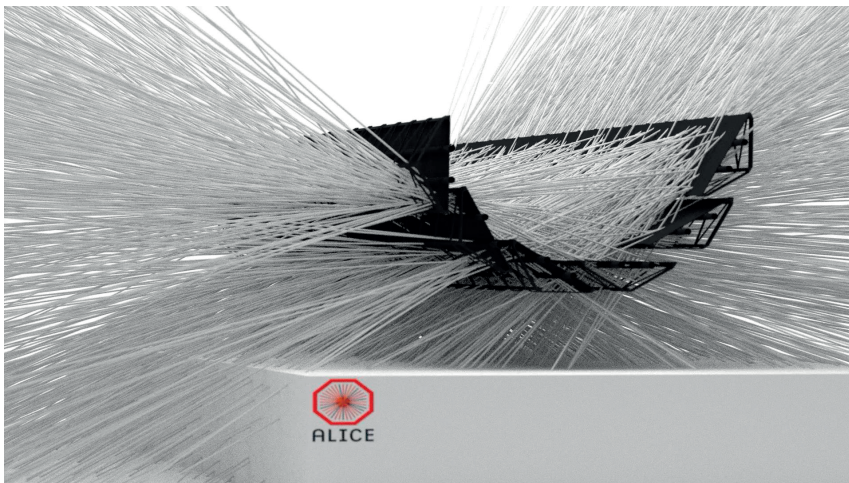


Figure 5.2: *Cosmic rays traversing the innermost layer of the ITS inner barrel.*

Looking at the near future, an interesting period with Run 3 data and new detector technologies to be developed and qualified is starting for ALICE. While for the distant future the ALICE experiment will continue pushing the technological edge towards becoming a next generation heavy ion experiment [64].

New-alpide-software

A.1 Classification cuts of individual scans

Table A.1: HIC classification scheme

Worst Scan Result	Number of Working Chips	Back Bias Working	HIC Class
gold	14/9	Yes	gold
silver	14/9	Yes	silver
bronze	14/9	Yes	bronze
Not working	14/9	Yes	Not working
gold, silver or bronze	13/8	Yes	Partially working
gold, silver or bronze	12/7	Yes	Partially working, cat. B
gold, silver or bronze	≤ 11/6	Yes	Not working
gold, silver or bronze	14/9	No	No back bias
gold, silver or bronze	12,13/8,7	No	No back bias, cat. B

¹IB HIC.

²OB HIC.

Table A.2: *FIFO scan classification cuts.*

Parameter	Category	
	gold	Not working
FIFO exceptions	0	otherwise
FIFO errors	0	otherwise

Table A.3: *Power test classification cuts.*

Parameter	Category			
	gold	silver	No backbias	Not working
$IDDD_{after\ switch\ on}$ (mA)	≥ 50	-	-	otherwise
$IDDA_{after\ switch\ on}$ (mA)	≥ 20	-	-	otherwise
$IDDD_{clocked}$ (mA)	300 to 550 ¹	otherwise	-	
	500 to 850 ²	otherwise	-	-
$IDDA_{clocked}$ (mA)	70 to 180 ¹	otherwise	-	-
	120 to 250 ²	otherwise	-	-
$I_{BB}(V_{BB} = -3\ V)$ (mA)	≤ 10	otherwise	-	-
I_{BB} (mA)	≤ 15	-	otherwise	-

Table A.4: *DCTRL scan classification cuts.*

Parameter	Category		
	gold	silver	Not working
Maximum amplitude (mV)	≥ 150 ¹	-	otherwise
	≥ 300 ²	-	otherwise
Slope (mV/DAC)	≥ 10 ¹	-	otherwise
	≥ 20 ²	-	otherwise
χ^2	≤ 0.05	-	otherwise
Rise/Fall time (ns)	≤ 10	otherwise	

Table A.5: *Digital scan classification cuts.*

Parameter	Category			
	gold	silver	bronze	Not working
Timeouts	0	-	-	otherwise
Corrupt events	0	-	-	otherwise
Bad pixels per chip	≤ 50	≤ 2100	≤ 5243	otherwise

Table A.6: *Digital white frame classification cuts.*

Parameter	Category			
	gold	silver	bronze	Not working
Unmaskable stuck pixels per chip	0	≤ 2	≤ 5	otherwise

Table A.7: *Threshold scan classification cuts.*

Parameter	Category			
	gold	silver	bronze	Not working
Pixels without threshold per chip	≤ 5243	≤ 26214	≤ 52429	otherwise
Dead pixels per chip	≤ 50	≤ 2100	≤ 5243	otherwise
Average noise (e^-)	≤ 10	otherwise	-	-

Table A.8: *Noise occupancy classification cuts.*

Parameter	Category			
	gold	silver	bronze	Not working
Noisy pixels per chip	≤ 50	≤ 2100	≤ 5243	otherwise

Table A.9: *Readout test classification cuts.*

Parameter	Category		
	gold	silver	Not working
Timeouts	0	-	otherwise
Corrupt events	0	-	otherwise
8b10b errors	0	otherwise	-

Table A.10: *Endurance test classification cuts of OB modules.*

Parameter	Category		
	gold	silver	Not working
Trips	0	≤ 3	otherwise
Working Chips	14	otherwise	-
Chip failures	0	≤ 3	otherwise

Bibliography

- [1] G. Lemaître, Un Univers homogène de masse constante et de rayon croissant rendant compte de la vitesse radiale des nébuleuses extra-galactiques, *Annales de la Société Scientifique de Bruxelles* 47 (1927) 49–59.
URL <https://ui.adsabs.harvard.edu/abs/1927ASSB...47...49L>
- [2] E. Hubble, A relation between distance and radial velocity among extra-galactic nebulae, *Proceedings of the National Academy of Sciences* 15 (3) (1929) 168–173. doi:10.1073/pnas.15.3.168.
URL <https://www.pnas.org/content/15/3/168>
- [3] J.-P. Luminet, Lemaitre’s big bang, 2016, p. 214. doi:10.22323/1.224.0214.
- [4] Particle Data Group at Lawrence Berkeley National Lab.
URL <https://particleadventure.org/history-universe.html>
- [5] The ALICE collaboration, The ALICE experiment at the CERN LHC, *Journal of Instrumentation* 3 (08) (2008) S08002–S08002. doi:10.1088/1748-0221/3/08/s08002.
URL <https://doi.org/10.1088/1748-0221/3/08/s08002>
- [6] R. Schicker, Overview of ALICE results in pp, pA and AA collisions., *EPJ Web Conf.* 138 (arXiv:1701.04810) (2016) 01021. 13 p. doi:10.1051/epjconf/201713801021.
URL <https://cds.cern.ch/record/2242545>
- [7] M. Thomson, *Modern particle physics*, Cambridge University Press, New York, 2013.
- [8] D. Griffiths, *Introduction to elementary particles*, 2008.

- [9] D. Dominguez, Standard Model. Le modèle standard. General Photo (Mar 2015).
URL <https://cds.cern.ch/record/2002395>
- [10] M. A. Stephanov, QCD phase diagram and the critical point, Prog. Theor. Phys. Suppl. 153 (2004) 139–156. arXiv:hep-ph/0402115, doi:10.1142/S0217751X05027965.
- [11] R. S. Bhalerao, Relativistic heavy-ion collisions (2014) 219–239. 21 parXiv:1404.3294, doi:10.5170/CERN-2014-001.219.
URL <https://cds.cern.ch/record/1695331>
- [12] CERN accelerator complex.
URL <http://cds.cern.ch/record/2684277>
- [13] A. Tauro, ALICE Schematics, general Photo (May 2017).
URL <https://cds.cern.ch/record/2263642>
- [14] R. J. Fries, B. Müller, C. Nonaka, S. A. Bass, Hadronization in heavy-ion collisions: Recombination and fragmentation of partons, Phys. Rev. Lett. 90 (2003) 202303. doi:10.1103/PhysRevLett.90.202303.
URL <https://link.aps.org/doi/10.1103/PhysRevLett.90.202303>
- [15] Y. Oh, C. M. Ko, S. H. Lee, S. Yasui, Ratios of heavy baryons to heavy mesons in relativistic nucleus-nucleus collisions, Phys. Rev. C 79 (2009) 044905. doi:10.1103/PhysRevC.79.044905.
URL <https://link.aps.org/doi/10.1103/PhysRevC.79.044905>
- [16] S. Plumari, V. Minissale, S. K. Das, G. Coci, V. Greco, Charmed Hadrons from Coalescence plus Fragmentation in relativistic nucleus-nucleus collisions at RHIC and LHC, Eur. Phys. J. C 78 (4) (2018) 348. arXiv:1712.00730, doi:10.1140/epjc/s10052-018-5828-7.
- [17] L. Vermunt, Measurement of λ_c^+ baryons and d_s^+ mesons in pb-pb collisions with alice (2019). arXiv:1910.11738.
- [18] L. van Doremalen, Overview of heavy-flavour measurements in ALICE, Acta Phys. Pol. B Proc. Suppl. 14 (arXiv:2005.06648) (2020) 15. doi:10.5506/APhysPolBSupp.14.15.
URL <https://cds.cern.ch/record/2718185>

- [19] L. Musa, Conceptual Design Report for the Upgrade of the ALICE ITS, Tech. Rep. CERN-LHCC-2012-005. LHCC-G-159, CERN, Geneva (Mar 2012).
URL <https://cds.cern.ch/record/1431539>
- [20] Technical Design Report for the Muon Forward Tracker, Tech. Rep. CERN-LHCC-2015-001. ALICE-TDR-018 (Jan 2015).
URL <https://cds.cern.ch/record/1981898>
- [21] Upgrade of the ALICE Time Projection Chamber, Tech. Rep. CERN-LHCC-2013-020. ALICE-TDR-016 (Oct 2013).
URL <https://cds.cern.ch/record/1622286>
- [22] P. Antonioli, A. Kluge, W. Riegler, Upgrade of the ALICE Readout & Trigger System, Tech. Rep. CERN-LHCC-2013-019. ALICE-TDR-015 (Sep 2013).
URL <https://cds.cern.ch/record/1603472>
- [23] P. Buncic, M. Krzewicki, P. Vande Vyvre, Technical Design Report for the Upgrade of the Online-Offline Computing System, Tech. Rep. CERN-LHCC-2015-006. ALICE-TDR-019 (Apr 2015).
URL <https://cds.cern.ch/record/2011297>
- [24] ALICE Collaboration, Letter of Intent for an ALICE ITS Upgrade in LS3, Tech. Rep. CERN-LHCC-2019-018. LHCC-I-034, CERN, Geneva (Dec 2019).
URL <https://cds.cern.ch/record/2703140>
- [25] Z. C. et al., Future physics opportunities for high-density qcd at the lhc with heavy-ion and proton beams (2019). [arXiv:1812.06772](https://arxiv.org/abs/1812.06772).
- [26] ALICE upgrade physics performance studies for 2018 Report on HL/HE-LHC physics (Feb 2019).
URL <https://cds.cern.ch/record/2661798>
- [27] H. Kolanoski, N. Wermes, Particle detectors: fundamentals and applications, Oxford University Press, Oxford, 2020. doi:10.1093/oso/9780198858362.001.0001.
URL <https://cds.cern.ch/record/2721300>

- [28] R. Gluckstern, Uncertainties in track momentum and direction, due to multiple scattering and measurement errors, *Nuclear Instruments and Methods* 24 (1963) 381 – 389. doi:[https://doi.org/10.1016/0029-554X\(63\)90347-1](https://doi.org/10.1016/0029-554X(63)90347-1).
- [29] Z. Drasal, W. Riegler, An extension of the Gluckstern formulae for multiple scattering: Analytic expressions for track parameter resolution using optimum weights, *Nuclear Instruments and Methods in Physics Research Section A: Accelerators, Spectrometers, Detectors and Associated Equipment* 910 (2018) 127 – 132. doi:<https://doi.org/10.1016/j.nima.2018.08.078>.
- [30] P.A. Zyla et al. (Particle Data Group), *Prog. Theor. Exp. Phys.* 2020, 083C01 (2020).
URL <https://pdg.lbl.gov/index.html>
- [31] H. A. Bethe, Molière's Theory of Multiple Scattering, *Phys. Rev.* 89 (1953) 1256–1266. doi:[10.1103/PhysRev.89.1256](https://doi.org/10.1103/PhysRev.89.1256).
- [32] H. Spieler, *Semiconductor Detector Systems*, Oxford University Press, 2005.
- [33] E. B. Podgoršak, *Radiation Physics for Medical Physicists*, Springer International Publishing, 2016. doi:<https://doi.org/10.1007/978-3-319-25382-4>.
- [34] W. R. Leo, *Techniques for Nuclear and Particle Physics Experiments*, Springer-Verlag Berlin Heidelberg, 1994. doi:[10.1007/978-3-642-57920-2](https://doi.org/10.1007/978-3-642-57920-2).
- [35] H. Bichsel, Straggling in thin silicon detectors, *Rev. Mod. Phys.* 60 (1988) 663–699. doi:[10.1103/RevModPhys.60.663](https://doi.org/10.1103/RevModPhys.60.663).
- [36] E. et al., Experimental methods and colliders, *Physics Letters B* 592 (1) (2004) 235 – 274, review of Particle Physics. doi:<https://doi.org/10.1016/j.physletb.2004.06.012>.
- [37] S. N. Ahmed (Ed.), *Physics and Engineering of Radiation Detection* (Second Edition), Elsevier, 2015. doi:<https://doi.org/10.1016/C2013-0-15270-1>.

- [38] G. Lutz, *Semiconductor Radiation Detectors*, Springer-Verlag Berlin Heidelberg, 2007. doi:10.1007/978-3-540-71679-2.
- [39] N. Wermes, L. Rossi, P. Fischer, T. Rohe, *Pixel Detectors, From Fundamentals to Applications*, Springer-Verlag, 2006. doi:10.1007/3-540-28333-1.
- [40] W. Shockley, Currents to conductors induced by a moving point charge, *Journal of Applied Physics* 9 (10) (1938) 635–636. doi:10.1063/1.1710367.
URL <https://doi.org/10.1063/1.1710367>
- [41] S. Ramo, Currents induced by electron motion, *Proceedings of the IRE* 27 (9) (1939) 584–585. doi:10.1109/JRPROC.1939.228757.
- [42] W. Riegler, An application of extensions of the ramo–shockley theorem to signals in silicon sensors, *Nuclear Instruments and Methods in Physics Research Section A: Accelerators, Spectrometers, Detectors and Associated Equipment* 940 (2019) 453–461. doi:<https://doi.org/10.1016/j.nima.2019.06.056>.
URL <https://www.sciencedirect.com/science/article/pii/S0168900219309015>
- [43] B. et al., Monolithic Active Pixel Sensors (MAPS) in a Quadruple Well Technology for Nearly 100Factor and Full CMOS Pixels, *Sensors* 8 (09 2008). doi:10.3390/s8095336.
- [44] J. W. van Hoorn, Study and Development of a novel Silicon Pixel Detector for the Upgrade of the ALICE Inner Tracking System, Ph.D. thesis, TU Vienna (10 2015).
URL <http://cds.cern.ch/record/2119197>
- [45] R. Turchetta, et al., A monolithic active pixel sensor for charged particle tracking and imaging using standard VLSI CMOS technology, *Nucl. Instrum. Meth. A* 458 (2001) 677–689. doi:10.1016/S0168-9002(00)00893-7.
- [46] A. et al., Technical Design Report for the Upgrade of the ALICE Inner Tracking System, Tech. Rep. CERN-LHCC-2013-024. ALICE-TDR-017 (Nov 2013). doi:10.1088/0954-3899/41/8/087002.

- [47] F. Reidt, Studies for the ALICE Inner Tracking System Upgrade, presented 28 Apr 2016 (Feb 2016).
URL <https://cds.cern.ch/record/2151986>
- [48] M. Suljic, Study of Monolithic Active Pixel Sensors for the Upgrade of the ALICE Inner Tracking System, Ph.D. thesis, presented 02 Feb 2018 (Nov 2017).
URL <https://cds.cern.ch/record/2303618>
- [49] P. Martinengo, The new Inner Tracking System of the ALICE experiment, Nucl. Phys. A 967 (2017) 900–903. 4 p. doi:10.1016/j.nuclphysa.2017.05.069.
URL <https://cds.cern.ch/record/2295080>
- [50] W. Snoeys, CMOS monolithic active pixel sensors for high energy physics, Nucl. Instrum. Methods Phys. Res., A 765 (2014) 167–171. 5 p. doi:10.1016/j.nima.2014.07.017.
- [51] K. et al., Front end optimization for the monolithic active pixel sensor of the ALICE Inner Tracking System upgrade, Journal of Instrumentation 11 (2016) C02042–C02042. doi:10.1088/1748-0221/11/02/C02042.
- [52] P. Y. et al., Low-power priority Address-Encoder and Reset-Decoder data-driven readout for Monolithic Active Pixel Sensors for tracker system, Nuclear Instruments and Methods in Physics Research Section A: Accelerators, Spectrometers, Detectors and Associated Equipment 785 (2015) 61 – 69. doi:<https://doi.org/10.1016/j.nima.2015.02.063>.
- [53] ALICE ITS ALPIDE development team, ALPIDE Operations Manual (July 2016).
URL http://www-subatech.in2p3.fr/~electro/projets/alice/dimuon/mft/pdf/ALPIDE-4-operations-manual_draft20160601.pdf
- [54] J. Schambach, J. Alme, M. Bonora, P. Giubilato, R. Hannigan, H. Hillemanns, M. Lupi, S. V. Nesbø, A. Rehman, G. A. Rinella, M. J. Rossewijn, K. M. Siewicz, A. Velure, A Radiation-Tolerant Readout System for the ALICE Inner Tracking System Upgrade, in: 2018 IEEE Nuclear Science Symposium and Medical Imaging Conference Proceedings (NSS/MIC), 2018, pp. 1–6. doi:10.1109/NSSMIC.2018.8824419.

- [55] A. Junique, The Engineering, Production and Quality Assurance of the Inner Barrel Staves for the Upgrade of the ALICE Inner Tracking System, PoS TWEPP2019 (2020) 081. 5 p. doi:10.22323/1.370.0081.
URL <https://cds.cern.ch/record/2725204>
- [56] G. De Robertis, G. Fanizzi, F. Loddo, V. Manzari, M. Rizzi, A Modular System for Acquisition, Interface and Control (MOSAIC) of detectors and their related electronics for high energy physics experiment, EPJ Web Conf. 174 (2018) 07002. 4 p. doi:10.1051/epjconf/201817407002.
- [57] M. Mager, Upgrade of the ALICE ITS in LS3, PoS Vertex2019 (2020) 040. doi:10.22323/1.373.0040.
- [58] X.-N. Wang, M. Gyulassy, HIJING : A Monte Carlo model for multiple jet production in pp, pA, and AA collisions, Phys. Rev. D44 D44 (1991) 3501–351. doi:10.1103/PhysRevD.44.3501.
URL <https://link.aps.org/doi/10.1103/PhysRevD.44.3501>
- [59] R. B. et al., GEANT detector description and simulation tool, CERN-W5013, CERN-W-5013 (1994). doi:10.17181/CERN.MUHF.DMJ1.
- [60] T. Sjostrand, S. Mrenna, P. Z. Skands, PYTHIA 6.4 Physics and Manual, JHEP 05 (2006) 026. arXiv:hep-ph/0603175, doi:10.1088/1126-6708/2006/05/026.
- [61] I. Belikov, Event reconstruction and particle identification in the ALICE experiment at the LHC, EPJ Web of Conferences 70 (2014) 00029. doi:10.1051/epjconf/20147000029.
- [62] P. SORENSEN, ELLIPTIC FLOW: A STUDY OF SPACE-MOMENTUM CORRELATIONS IN RELATIVISTIC NUCLEAR COLLISIONS, Quark-Gluon Plasma 4 (2010) 323–374doi:10.1142/9789814293297_0006.
URL http://dx.doi.org/10.1142/9789814293297_0006
- [63] Minutes of the 139th Meeting of the LHCC, Tech. Rep. CERN-LHCC-2019-010. LHCC-139, CERN, Geneva (Sep 2019).
URL <https://cds.cern.ch/record/2689443>
- [64] D. Adamová et al., A next-generation LHC heavy-ion experiment (2019). arXiv:1902.01211.



Summary

The ALICE experiment at CERN is dedicated to study the properties of the strongly interacting matter and the Quark Gluon Plasma through heavy ion collisions at the LHC. During the 2020s, ALICE is entering a new era of measurements in the heavy flavour sector benefiting from the detector upgrades that will enhance its capabilities. The first part of this thesis provides an overview of the detector characterization and classification that was performed during the (pre) production phase of the upgrade of the ALICE Inner Tracking System (ITS) during the Long Shutdown 2. A detailed description of the tests that were used for the evaluation of the electrical response of the detector components and the data transmission are presented and accompanied by indicative results that reflect the detector quality. In the second part of the thesis, the impact of a further ITS upgrade, during the Long Shutdown 3, is studied on the beauty sector of heavy flavour and more precisely on the measurement of the Λ_b baryon. The significance and the signal over background ratio of measuring the Λ_b particle were estimated and compared for the two upgrades. Benefiting from the improved pointing resolution that the proposed future ultra-low mass detector will offer, an improvement especially in the low momentum region is reported. The research performed in this thesis reflects how well the latest technological advances combine with high energy physics and contribute to the understanding of our universe.

Samenvatting

Het ALICE-experiment op CERN is gewijd aan het onderzoeken van de eigenschappen van sterk-interacterend quarkmaterie en het quark-gluonplasma. Dit wordt bereikt door het bestuderen van zware ionenbotsingen in de LHC. Tijdens de jaren twintig van de 21ste eeuw zal ALICE een nieuw tijdperk betreden waarin metingen van hadronen, opgebouwd uit ten minste één zware quark, veel nauwkeuriger zullen worden vanwege uitgevoerde detector upgrades. Het eerste deel van dit proefschrift geeft een overzicht van de karakterisering en classificatie van de detector die werd uitgevoerd tijdens de (pre) productiefase van de upgrade van de ALICE Inner Tracking System (ITS) tijdens Long Shutdown 2. Er wordt een gedetailleerde beschrijving gegeven van de testen die werden gebruikt voor de evaluatie van de elektrische respons van de detectorcomponenten en de gegevensoverdracht, vergezeld met indicatieve resultaten die de kwaliteit van de detector weerspiegelen. In het tweede deel van het proefschrift wordt de impact die een vervolg upgrade van de ITS detector tijdens Long Shutdown 3 op de beauty sector zal hebben bestudeerd, specifiek op de meting van het Λ_b baryon. De statistische significantie en de signaal-tot-achtergrond ratio van het te meten Λ_b deeltje werden geschat en vergeleken tussen beide detector upgrades. Profiterend van de verbeterde resolutie die de voorgestelde toekomstige detector zal bieden, wordt een nauwkeuriger Λ_b signaal verwacht, vooral in het lage momentum regime. Het onderzoek in dit proefschrift laat zien hoe goed de nieuwste technologische ontwikkelingen combineren met het veld van hoge-energiefysica en daardoor bijdragen aan het begrip van ons universum.

Acknowledgements

The last part of this book is devoted to the people that were next to me during the last years. First, I would like to thank Luciano for all his guidance and support throughout my PhD. It was a pleasure for me to be part of the CERN ITS group, learn, develop and contribute in a perfect working environment. Raimond, thanks for supporting my efforts from the very beginning and for all your advices.

Markus, I feel grateful for all your help throughout the years. You were there every moment, every day, ready to give me feedback and answer even the most strange questions. During our discussions I was trying to absorb the maximum from your knowledge and I always felt a bit more wiser afterwards. Thank you for everything Markus.

Paul, as I have said many times I do not know how it would have been without you. In the moments of crisis you helped me move forward and gain back my strength. From the deepest part of my soul thank you for supporting me and believing in me during the last six years.

I would also like to thank Felix and Magnus from the ITS group for the help and the nice discussions we had over the last years. Also a big thanks to Vit, the best officemate ever. My paranymphs, Luuk and Zhanna, and my very good friend Elena thank you for being next to me in this journey.

Finally, I would like to thank my family. My husband, Stergios that survived my dissertation and could fix everything with a hug. My mum and dad, that are constantly helping me make my dreams come true and supporting even my craziest ideas. But mostly my granddad and grandmum, that from my baby steps in Kallithea, are filling my life with endless love and kindness.

Thank you all for helping me accomplish my dream!



Curriculum Vitae

<i>Current</i>	Post-doctoral researcher Syracuse University, New York, USA Coordination of the assembly and commissioning activities of the Upstream Tracker of the LHCb experiment at CERN.
<i>December 2021</i>	PhD in Particle Physics CERN Doctoral Student, Geneva, Switzerland, Utrecht University, The Netherlands Thesis title: "Detector characterization and Λ_b measurements with the upgrades of the ALICE Inner Tracking System"
<i>February 2017</i>	MSc Physics: Gravitation, Astro-, and Particle Physics University of Amsterdam, Nikhef, The Netherlands Thesis title: "Development of a testing system for the silicon pixel detectors of the Inner Tracking System of ALICE"
<i>January 2015</i>	Diploma of Applied Mathematical and Physical Sciences 5-year, MSc equivalent National Technical University of Athens (NTUA), Greece Thesis title: "Development of Temperature and Humidity Measure- ment System based on Arduino and WinCC OA"

